

UC Riverside

UC Riverside Electronic Theses and Dissertations

Title

Utilization of Inelastic Scattering Techniques in Phonon Measurements

Permalink

<https://escholarship.org/uc/item/48s4g198>

Author

Cai, Qingan

Publication Date

2022

Peer reviewed|Thesis/dissertation

UNIVERSITY OF CALIFORNIA
RIVERSIDE

Utilization of Inelastic Scattering Techniques in Phonon Measurements

A Dissertation submitted in partial satisfaction
of the requirements for the degree of

Doctor of Philosophy

in

Mechanical Engineering

by

Qingan Cai

December 2022

Dissertation Committee:

Dr. Chen Li, Chairperson
Dr. Sinisa Coh
Dr. Boniface Fowka Tsinde

Copyright by
Qingan Cai
2022

The Dissertation of Qingan Cai is approved:

Committee Chairperson

University of California, Riverside

Acknowledgments

It would not have been possible for me to complete my Ph.D. studies without many kind and supportive people: friends, mentors, and family members in my life. Some, however, deserve a particular mention in this acknowledgment.

Above all, I would like to express my deepest gratitude to Dr. Chen Li, my supervisor and personal mentor, for his dedicated guidance and support throughout my Ph.D. career. His supportive patience, continued motivation, and knowledgeable feedback and suggestions encouraged me every step of the way in pursuing my degree.

This thesis would not have been possible without my dissertation committee: Dr. Sinisa Coh and Dr. Boniface Fowka Tsinde. Both are distinguished researchers who have provided professional and insightful comments and feedback for my dissertation and final defense. I would like to express my sincere thanks to both of them.

I would like to acknowledge and appreciate the scientists at Argonne National Laboratory and Oak Ridge National Laboratory. Particularly to Dr. Ayman H. Said for his assistance during the difficult experiments. Without his support, the experiments would not have been completed. My deepest appreciation also goes to Dr. Eric Chronister, Dr. Olle Hellman, and Dr. Barry Winn for offering advice on my research articles, aiding in the performance of theoretical simulation, and collaborating to conduct innovative experiments. Without them, my research horizon would not have been as broad as today.

I would also like to thank my colleagues at our lab for their enthusiastic discussions, for our sleepless nights working together at APS, and for the five years of fun and hard work

we shared together as an unbreakable team. Thank you for going through this tough time with me.

Last but not least, I would like to extend my sincere love to Elaine. Thanks for being with me and encouraging me during my darkest and most challenging time. Your persistent companionship illuminates my life and inspires my confidence in overcoming the difficulties in my research. I would also like to express my grateful appreciation to our families for supporting us in realizing dreams.

To you for all the support.

ABSTRACT OF THE DISSERTATION

Utilization of Inelastic Scattering Techniques in Phonon Measurements

by

Qingan Cai

Doctor of Philosophy, Graduate Program in Mechanical Engineering

University of California, Riverside, December 2022

Dr. Chen Li, Chairperson

The microscopic study of lattice vibrations is essential for regulating the thermal properties and understanding the phase transition of materials. As for the newly proposed and observed chiral phonons, they are significant in controlling the entanglement of quantum dots and generating the thermal Hall effect in materials. In layered transition metal chalcogenides and some other quantum materials, their lattice dynamics are mostly studied by first-principles calculations, the phonon measurement is relatively rare, especially with temperature and pressure dependence.

Phonon theory and experimental techniques, such as inelastic X-ray scattering, inelastic neutron scattering, and Raman scattering, for phonon measurement are briefly discussed. The phonon computational method is also reviewed. Phonon measurements and theoretical calculations were performed on some layered materials and other quantum materials.

Using millielectronvolt-resolution non-resonant inelastic X-ray scattering, we discovered that it could be utilized to directly probe phonon chirality throughout the whole

Brillouin zone in tungsten carbide. The results show that phonon chirality and X-ray polarization play essential roles in the scattering process. The results also suggest that a revision to the textbook X-ray scattering function of phonons is needed.

To study the temperature and pressure dependence of lattice dynamics in materials, especially for layered transition metal chalcogenides, we performed the first temperature- and pressure-dependent inelastic X-ray scattering measurements on bulk tungsten diselenide and obtained the mode Grüneisen parameters. The results show monolayer-like lattice dynamics in the bulk tungsten diselenide. We also performed the pressure-dependent phonon measurement on palladium diselenide. A panoramic diamond anvil cell was used to generate the high hydrostatic pressure. We observed the pressure-dependent flexural phonons for the first time and quantified the elastic properties and interlayer van der Waals interactions in layered materials.

Using inelastic neutron scattering, temperature- and pressure-dependent phonon lattice dynamics measurements on p-terphenyl were studied. The results indicate strong anharmonic phonon dynamics and suggest a lack of phase transition in the region of 0~1.51 kbar and 10~30 K.

Using Raman scattering, the pressure- and temperature-dependent results on Fe_3GeTe_2 were performed, and a significant pressure-induced phonon energy shift was observed. The phonon energy shift may be related to the strong spin-phonon interactions, which may play important roles in its application for magnetic storage devices.

Contents

List of Figures	xi
List of Tables	xix
1 Introduction	1
2 Theory and Methods	4
2.1 Phonon Theory	4
2.2 Computation methods	10
2.3 Inelastic scattering techniques	14
2.3.1 Raman scattering	14
2.3.2 Inelastic neutron scattering (INS)	15
2.3.3 Inelastic X-ray scattering (IXS)	16
2.3.4 Control of X-ray polarization	18
3 Chiral Phonon Measurement	21
3.1 Direct observation of chiral phonons in WC by IXS	21
3.1.1 Introduction	22
3.1.2 Experiment and Calculation	24
3.1.3 Results and Discussion	29
3.1.4 Conclusion	42
4 Temperature- and Pressure- Dependent Phonon Measurements	43
4.1 Temperature- and pressure-dependent phonon measurements on layered WSe ₂	43
4.1.1 Introduction	44
4.1.2 Materials and Methods	47
4.1.3 Results	50
4.1.4 Discussion	59
4.1.5 Conclusion	62
4.2 Phonon anharmonicity in para-terphenyl	63
4.2.1 Introduction	63
4.2.2 Experiment	66

4.2.3	Results and discussion	67
4.2.4	Conclusion	77
4.3	Quantify the Van der Waals interactions in layered PdSe ₂	79
4.3.1	Introduction	79
4.3.2	Experiment and calculation	82
4.3.3	Results and discussion	86
4.3.4	Conclusion	99
4.4	Anomalous phonon softening in Fe ₃ GeTe ₂	101
4.4.1	Introduction	101
4.4.2	Methods	103
4.4.3	Results	106
4.4.4	Discussion	110
4.4.5	Conclusion	116
5	Conclusion	118
	Bibliography	121

List of Figures

2.1	Schematic for the 30-ID beamline layout. [121]	16
2.2	Schematic of X-ray Phase Retarder (XPR) setup. (a) Measurement of X-ray polarization. The purple arrows represent the X-ray beam, IH and IV are measured by detector 1 and 2 respectively. (b) Image of the diamond crystal phase retarder.	18
2.3	Accurately controlled X-ray polarization by a diamond XPR. (a) The degree of linear polarization with respect to the deflected angle. (b) The degree of circular polarization with respect to the deflected angle.	19
3.1	Lattice structure of WC and scattering schematic. (a) WC has a hexagonal lattice structure. Red and blue spheres represent tungsten atoms and carbon atoms, respectively. (b) K and K' are distinguished in the Brillouin zone, indicating the broken inversion symmetry. (c)-(d) In-plane scattering geometry and out-of-plane scattering geometry are designed and plotted in the reciprocal space. Red balls in (c) and (d) represent the reciprocal lattice points; k_{in} , k_{out} , and k_{ph} represent the wavevector of incident electric field, scattered electric field and phonon in the inelastic scattering process. Direction of phonon angular momentum along c-axis, l_c , is represented by purple arrows in (c) and (d). The black arrows indicate the polarization of incident X-ray.	23
3.2	In-plane reciprocal space map and the measured K/K' points. The blue rhombuses represent K/K' points measured in the in-plane scattering geometry, while the blue stars represent the K' points measured in the out-of-plane scattering geometry. The red arrows indicate the same $ \mathbf{Q} $ of these three K/K' points. (b) Measured \mathbf{Q} points away from K/K' points. (c) The rocking curve of WC single crystal measured by HERIX shows the high crystalline quality.	25
3.3	Schematic of a multiple scattering process. Triangle formed by BD, $ k_{in} $, and $ k_{hkl} $ is plotted in green color.	28

3.4	Phonon dispersion, DOS, and phonon angular momentum of WC. (a) Phonon dispersion of WC from DFT calculation agrees well with experimental measurement. There are three acoustic and three optical phonon branches. Calculated phonon dispersion relations are plotted in lines and IXS measurement is represented by black symbols. The error bars indicate the fitting error of phonon energy in IXS spectra. The red dashed dispersion lines are from Ref. [54]. (b) Measured acoustic phonon DOS of WC agrees well with DFT calculation. The solid red line represents the calculated total DOS of WC; the black line represents the (neutron-weighted) DOS below 30.9 meV measured by INS. (c) Phonons near K/K' points are circularly polarized. Phonon angular momentum is plotted by purple and red lines along in-plane high symmetry directions. The purple and red colors represent positive and negative value of angular momentum respectively.	31
3.5	Animations of TA and LA modes at K and K'. (a) and (b) Animations of TA and LA at K points. (c) and (d) Animations of TA and LA at K' points. Red and blue spheres represent tungsten atoms and carbon atoms, respectively. The animations are generated by ascii-phonons. [63]	33
3.6	The simulation based on equation (3.8) agrees well with the measurement at \mathbf{Q} points away from K and K' points. (a)-(f) IXS spectra with linearly polarized X-ray at (2 0.2 0), (2.2 0.2 0), (2.1 0.1 0), (2 0.5 0), (1.8 0.6 0) and (1.8 0.4 0) in the reciprocal space, respectively. Solid red lines are the Voigt fittings of IXS spectra and dotted black lines represent the spectra simulated from the scattering function. Error bars are from the counting statistics. . .	37
3.7	The simulation based on equation (3.8) agrees well with the measurement at K and K' points in the in-plane scattering geometry. (a)-(d) IXS spectra with linearly polarized X-ray at (0.33 1.33 0), (0.33 2.33 0), (0.66 1.66 0), and (2.33 0.33 0) in the reciprocal space, respectively. Solid red lines are the Voigt fittings of IXS spectra and dotted black lines represent the spectra simulated from the scattering function. Error bars are from the counting statistics	38
3.8	The simulation based on equation (3.8) disagrees with the measurement at K and K' points in the out-of-plane scattering geometry. (a)-(b) IXS spectra at K' points (2.66 -2.33 0) and (1.66 -2.33 0); ZA is an out-of-plane acoustic phonon mode; its appearance is explained by multiple scattering. Solid red lines are the Voigt fittings of IXS spectra and dotted black lines represent the spectra simulated from the scattering function. Error bars are from the counting statistics.	39

3.9	X-ray polarization could affect the scattering intensities of circularly polarized phonons. (a) Polarization dependent IXS spectra at K' (2.66 -2.33 0) point. The spectrum at each polarization is integrated from 3-4 scans. The measured intensity is normalized by the flux of incident X-ray after XPR. All the peaks are fitted by Voigt functions. The purple numbers represent the value of P_C . (b) Polarization dependent intensity change of TA and LA modes; (c) Intensity relation of TA and LA modes; Blues line represents the simulated result from existing theory. P_C is the degree of X-ray circular polarization. Shading areas in (b)-(c) are the error sections.	41
4.1	(a) Top view and side view of atomic structure of 2H-WSe ₂ ; (b) First Brillouin zone in the reciprocal space.	45
4.2	The rocking curve of WSe ₂ single crystal measured by HERIX shows the high crystalline quality. The X-ray wavelength is 0.5226 Å. The narrow full width at half maximum (FWHM) indicates high crystalline quality of the sample.	47
4.3	Phonon dispersion of bulk and monolayer WSe ₂ along high symmetry directions at 300 K. (a) Comparison between calculated and experimental dispersion of bulk WSe ₂ ; (b) Comparison between calculated monolayer dispersion and experimental bulk dispersion. Orange lines and dots represent the calculated and measured longitudinal modes, red color represents the in-plane transverse modes, blue color represents the out-of-plane transverse modes, and the dark red triangles are Raman active modes. All IXS spectra are fitted by Gaussian function, error bar represents the fitting error of phonon peak.	50
4.4	Intensity simulation of bulk and monolayer WSe ₂ . (a) and (b) represent the dynamical structure factor of phonon branches along Γ -M in Brillouin zone (1 1 0) and (0 0 12) in bulk WSe ₂ ; (c) and (d) represent the dynamical structure factor of phonon branches along Γ -M in Brillouin zone (1 1 0) and (0 0 12) in monolayer WSe ₂ . The white dashed lines represent the phonon dispersion, the color bar is in log scale. A resolution of 1.5 meV is used in the simulation.	51
4.5	Temperature dependent phonon measurement on acoustic phonons (a) Phonon measurement along in-plane high symmetry directions; The insets are the IXS spectra at (0 0.1 12) and (-0.05 0.1 12) at 300 K and 150 K respectively. (b) Phonon measurement along out-of-plane direction. The error bar represents the fitting uncertainty. The orange, red and blue colors represent the LA, TA, and ZA modes respectively. The filled, hollow, and crossing markers represent 300, 150, and 25 K.	53

4.6	IXS spectra with Gaussian fitting. (a) IXS spectra measured along Γ -M direction in BZ (1 1 0) under 300 K; The black points represent raw data, and the red lines represent the Gaussian fitting. (b) IXS spectra measured at (0 0 12.5) along Γ -A direction under 300 K (black), 150 K (green) and 25 K (blue). (c) IXS spectra measured at (1.2 1 0) along Γ -M direction under 300 K (black), and 25 K (blue). (d) IXS spectra measured at (0 0.1 12) along Γ -M direction under 300 K (black), and 150 K (green). (e) IXS spectra measured at (0.9 1.2 0) along Γ -K direction under 300 K (black), and 25 K (blue). (f) IXS spectra measured at (-0.05 0.1 12) along Γ -K direction under 300 K (black), and 150 K (green). The intensity is rescaled to arbitrary unit (a. u.).	55
4.7	Temperature dependent phonon measurement on acoustic phonons (a) Phonon measurement along in-plane high symmetry directions; (b) Phonon measurement along out-of-plane direction. The phonon linewidths are shown as error bars. The points without error bar means the phonon linewidths are resolution limited. The orange, red and blue colors represent the LA, TA, and ZA modes respectively. The filled, hollow, and crossing markers represent 300, 150, and 25 K.	56
4.8	(a) Acoustic phonon isobaric modes Grüneisen parameters compared with bulk calculation; (b) Acoustic phonon isobaric modes Grüneisen parameters compared with monolayer calculation. Blue lines and points represent the Grüneisen parameters of ZA mode obtained from calculation and experiment, respectively. Orange and red represent LA and TA, respectively. Solid lines represent the calculation based on QHA, the dashed lines represent the γ dispersion relation from literature. [61]	58
4.9	(a) Pressure dependence of TA modes along Γ -M; (b) Pressure dependence of LA modes along Γ -M. (c) Acoustic phonon isothermal modes Grüneisen parameters compared with bulk calculation; (d) Acoustic phonon isothermal modes Grüneisen parameters compared with monolayer calculation. Orange, red and blue lines represent the Grüneisen parameters of LA, TA and ZA modes obtained from calculation based on QHA, respectively. Orange and red points represent the experimental isothermal Grüneisen parameters. . .	60
4.10	Phase diagram of p-terphenyl. The open markers represent data collected on deuterated p-terphenyl [139][Toudic] through inelastic neutron scattering (open circles) and Raman scattering (open triangles). The filled markers represent Raman scattering data [87] [Leme] (blue filled circles) on p-terphenyl and molecular dynamic simulations [18] (green filled circles). The filled orange squares represent optical spectroscopy results on pentacene-doped p-terphenyl [49] [Baer]. The green filled triangles show the temperature dependence at ambient pressure. The red symbols indicate the temperature and pressure regime of the current study on crystalline p-terphenyl. No solid-solid phase transition is observed in the measured regime. The black dotted lines represent a guide to denote the different solid-solid phase boundaries. A boundary gap exists between the deuterated and nondeuterated p-terphenyl.	66

4.11	Pressure-dependent phonon spectra of para-terphenyl acquired on VISION. (a)(b)(c) Pressure-dependent spectra show only minor changes from 0 to 1.51 kbar at 10 K; (d)The pressure-dependent phonon energy shifts from 0 to 1.51 kbar at 10 K. Peaks in spectra are fitted with Gaussian functions. Error bars indicate the fitting tolerance of phonon energy in spectra. Phonon energies at ambient pressure are labelled and the energy shifts with respect to the energy at 0 kbar are fitted by linear functions. Three representative types of phonon modes are plotted based on the pressure dependence. Phonon mode at 14.9 meV does not show much change with pressure; phonon mode at 75.9 meV softens with increasing pressure; and phonon mode at 24.2 meV stiffens with increasing pressure.	70
4.12	The log-log plot of the energy ratio vs. the volume ratio for four vibrational modes at $\nu_1=4.9$ meV, $\nu_2=6.6$ meV, $\nu_3=14.9$ meV, and $\nu_4=49.5$ meV. (a) Pressure dependent data yield the Grüneisen parameters of $\gamma_{1T}=0.09\pm 0.07$, $\gamma_{2T}=0.12\pm 0.07$, $\gamma_{3T}=0.10\pm 0.01$, and $\gamma_{4T}=-0.02\pm 0.01$. (b) Temperature dependent data yield the Grüneisen parameters of $\gamma_{1P}=-5.5\pm 0.9$, $\gamma_{2P}=4.4\pm 1.2$, $\gamma_{3P}=0.3\pm 0.2$, and $\gamma_{4P}=0.5\pm 0.1$. The data points are calculated from the peaks fitting of spectra in Figure 4.11 and Figure 4.14. The lines are linear fits, and their slopes are the mode Grüneisen parameters, γ , with error bars shown in Figure 4.15 (b). The magnitude of γ is larger in the temperature dependent data, especially for the low-frequency librational modes. Linear fitting quality depends on the phonon energy from Gaussian fitting, related to the peak statistics in spectra.	72
4.13	Temperature-dependent phonons below 74.4 meV (600 cm^{-1}) acquired on FDS. Temperature-dependent neutron spectra of the low-frequency librational region for p-terphenyl from 10 to 200 K. The spectra were corrected for thermal neutron occupation. There are strong temperature-induced changes in intensity, energy, and linewidth for various phonon modes but no signs of phase transition.	73
4.14	Temperature-dependent phonon spectra of p-terphenyl acquired on VISION. (a) Temperature-dependent phonon spectra of the low energy modes at 0.5 kbar; (b) The pressure-dependent phonon energy shifts from 10 K to 30 K at 0.5 kbar. Error bars indicate the fitting tolerance of phonon energy in spectra. Phonon energy at 10 K is labelled at the first points and the lines are linear fits.	74
4.15	The comparison between the Grüneisen parameters calculated from temperature- and pressure-dependent data. Large differences are found with no simple correlations between them. The temperature dependent Grüneisen parameters show large variations. Light blue symbols in (a) and (b) represent the modes with little pressure dependence.	76

4.16	Crystal structures of layered PdSe ₂ . a and b are the front and side views of the orthorhombic structure with space group <i>Pbca</i> before phase transition, respectively, while c and d are the front and side views of the cubic structure with space group <i>Pa$\bar{3}$</i> after phase transition, respectively. The arrow with color from yellow to purple represents the increasing of pressure.	82
4.17	Sample preparation for pressure-dependent IXS measurement of 2D-layered PdSe ₂ single crystal. a, Rocking curve for (002) Bragg peak of PdSe ₂ crystal. The narrow peak width indicates by the arrow shows high crystalline quality. Inset is the sample attached on a copper post for the ambient pressure measurement. b, Sample loading for high-pressure measurement with panoramic DAC. Left and right panels are the object and schematics of DAC, respectively. c, Schematic of the beam scattering geometry for the high-pressure experiment. Solid red frame in the right panel shows the DAC mounted on HERIX. Middle panel shows the sample and beam scattering geometries. Left panel shows the scattering vectors in zone (211). d, Sample geometry for ZA mode measurement under high pressure. The first and second methods are commonly used for high-pressure IXS measurement, while the third one is the method used in this work.	83
4.18	Calculated dynamic structure factors of PdSe ₂ along Γ -Y direction by IXS at zone (2 1+ q 1) under 0 GPa (a) and 6 GPa (b). Arrows indicate the longitudinal, transverse, and flexural acoustic modes (LA, TA, and ZA). Color bar indicates the phonon intensity plotted on a logarithmic scale.	85
4.19	Diffraction patterns of (211) plane of PdSe ₂ . Patterns at 0.36 GPa (a) and 6 GPa (b) show the phase transition and indicate the high quality of the single crystal sample. The yellow circles are the reference line for sample alignment. (c) Simulation of the reciprocal space of PdSe ₂ along the experimental view axis. The red arrows indicate the (211) plane group.	89
4.20	Calculated systematic free energy of PdSe ₂ with pressure. Yellow and purple shadows represent before and after phase transition, and the position of interface is estimated from ref. [131]	90
4.21	Pressure-dependent crystal change of PdSe ₂ . a, Bragg peak of (211) plane by HERIX. The vertical green solid lines are the predictions by Single Crystal software. b, Schematic formation of octahedral [PdSe ₆] from the orthorhombic to cubic structure, including the orbital correlation, reproduced from ref. [97]. c, Pressure-dependent lattice constants and the volume. Dashed lines are the fitting curves from $y = A + Bx + Cx^2$. Green curve is guide for eyes. d and e are the bond length and ICOHP of Pd-Se ₁ , Pd-Se ₂ , and Pd-Se ₃ , respectively. f, Force constant of Pd-Pd. Yellow and purple shadows represent before and after phase transition, and the position of interface is estimated from ref. [97].	91

4.22	Pressure-dependent acoustic phonon dispersions along Γ –Y of PdSe ₂ . a-c, Measured phonon modes of LA, TA, and ZA branches (symbols), overlaid with the corresponding first-principles calculations (lines). d, Exponential fittings of the ZA branches with $\omega = \alpha \mathbf{q}^\beta$ function (arrow). e, Pressure-dependent fitting parameters α and β . Error bars are the fitting uncertainty. Shadows represent the different structures as described in previous figures. .	92
4.23	Calculated low-energy phonon dispersions of PdSe ₂ under each pressure. . .	94
4.24	Fitted ZA mode of layered PdSe ₂ by equation (4.7) at each pressure.	95
4.25	Pressure-dependent elastic constants of PdSe ₂ . a-d are the results of C ₂₂ , C ₆₆ , C ₃₃ , and C ₄₄ and by, respectively. e and f are the interlayer compression (fdirect) and shear (fshear) force constants, respectively. Dashed lines in (c) and (e) indicate the trend with pressure. Error bars are the fitting uncertainty. Shadows represent the different structures as described in previous figures.	97
4.26	a) Side and (b) top view of hexagonal lattice crystal structure of Fe ₃ GeTe ₂ . The red, green, and tan spheres represent the Fe, Ge, and Te atoms, respectively.	102
4.27	Pressure-dependent (PD) Raman spectra at 300 K. (a) Raman spectra from ambient pressure to 9.52 GPa, (b) Pressure dependence of phonon frequency, and (c) pressure dependence of phonon linewidth. The phonon peaks are fitted by Lorentzian function. FWHM stands for the Full Width at Half Maximum. The lines in (b) and (c) are linear fits.	107
4.28	Schematic animation of E _{2g} ² and A _{1g} ¹ modes from (a) spin-polarized and (b) non-spin polarized calculations. The red, green, and tan spheres represent the Fe, Ge, and Te atoms, respectively. The arrows represent phonon eigenvectors.	108
4.29	Pressure and temperature-dependent (PTD) Raman spectra. (a) Raman spectra of FGT at temperatures from 8 to 300 K and under pressures from 9.43 GPa to ambient pressure. (b) Comparison between PD data and PTD data. The solid red squares and blue circles represent the PTD E _{2g} ² and A _{1g} ¹ , respectively. The hollow red squares and blue circles represent the PD E _{2g} ² and A _{1g} ¹ , calculated from the fitted pressure dependence. (c) Extracted temperature-dependent (TD) phonon frequency. The solid red squares and blue circles represent the PTD E _{2g} ² and A _{1g} ¹ , respectively. The hollow red squares and blue circles represent the extracted TD E _{2g} ² and A _{1g} ¹ , respectively. The green triangles represent the TD E _{2g} ² obtained from the literature. [38]	111
4.30	Magnetic phase transition and spin-phonon interactions. (a) Pressure-dependent phase diagram. PM and FM represent paramagnetic and ferromagnetic, respectively. The blue square dashed line represents the phase boundary from Heshen et al. [144]. The red circle dashed line represents the phase boundary from Jie-Min et al.[154]. The black triangle solid line represents our measured data points. (b) Phonon linewidth of the two measured modes.	112

4.31 (a) Calculated pressure-dependent lattice parameters of Fe_3GeTe_2 . (b) Calculated energy difference between the FM and AFM magnetic states at different pressures. (c) Pressure-dependence of magnetocrystalline anisotropy energy for the FM and AFM states. 114

List of Tables

3.1	Phonon linewidth obtained by super-resolution method.	30
4.1	β parameter of ZA dispersion within Γ -M ($q < 0.2$) and Γ -K ($q < 0.1$). . .	53
4.2	Phonon modes measured by inelastic neutron scattering compared with the results from Raman and IR spectroscopy. [LMA-long molecular axis, SMA1-short molecular axis (perpendicular to molecular plane), SMA2-short molecular axis (parallel to molecular plane), OP-out-of-plane, IP-in plane, Translation, Lib-libration]. Zig-Zag motion looks like a six C alkane which turns into its mirror image.	71
4.3	Pressure-dependent lattice information of PdSe ₂	88
4.4	Fitted data from LA mode along Γ -Y of PdSe ₂	88
4.5	Fitted data from TA mode along Γ -Y of PdSe ₂	88
4.6	Fitted data from ZA mode along Γ -Y of PdSe ₂	90
4.7	Pressure-dependent layer spacing of PdSe ₂	98
4.8	Spin exchange parameters for experimental and 7 GPa structures obtained from SPRKKR calculations.	115
4.9	Calculated frequencies (cm ⁻¹) of Raman active modes under various pressure.	116

Chapter 1

Introduction

Lattice dynamics is a fundamental property of materials. Understanding the microscopic lattice dynamics is essential for studying the phase stability, regulating the thermal transport properties, explaining the superconductivity, and manipulating the valley spin in materials. [44, 128, 90] The measurement of lattice dynamics is usually realized by using inelastic X-ray scattering (IXS), inelastic neutron scattering (INS), and Raman scattering techniques. With the rapid development of modern technologies, the fabrication of nano-electronic and spintronic devices will involve applying 2D layered materials. It is of great urgency to have an in-depth study on their phonon dynamics to enhance functionality and thermal stability in these materials. However, the comprehensive phonon measurement in two-dimensional (2D) layered materials is rare, especially with pressure and temperature dependence.

More recently, the chirality concept was extended for phonons in 2D and 3D materials with broken inversion symmetry, leading to the observation of chiral phonons. [24, 25]

Chiral phonons offer a new possibility for information processing and designing phononic quantum devices. The current measurement of chiral phonons is indirect and could not allow characterizing chirality throughout the whole Brillouin zone (BZ). Therefore, a new method is needed to integrate the most advanced inelastic scattering techniques for chiral phonon measurement.

In this work, phonon theory and experimental techniques, such as IXS, INS, and Raman scattering, for phonon measurement are discussed. The phonon computational method is also reviewed. Phonon measurement on layered transition metal dichalcogenides (TMDs), tungsten diselenide (WSe_2) and palladium diselenide (PdSe_2), topological semimetal tungsten carbide (WC), polycyclic aromatic hydrocarbons para-terphenyl (PTP), layered magnetic materials Fe_3GeTe_2 (FGT) were conducted by using the techniques as mentioned above. Theoretical calculations were compared with the experimental results for a well-rounded study on lattice dynamics in these materials.

Using millielectronvolt-resolution non-resonant IXS, we discovered that it could be utilized to directly probe phonon chirality throughout the whole Brillouin zone in bulk WC. The results show that phonon chirality and X-ray polarization play essential roles in the scattering process. The results also suggest that a revision to the textbook X-ray scattering function of phonons is needed. In WSe_2 , we performed the first temperature- and pressure-dependent phonon dispersions measurements and obtained the mode Grüneisen parameters and found a monolayer-like lattice dynamics in its bulk system. The pressure-dependent phonon measurement on PdSe_2 was performed by using the Diamond Anvil cell to generate the high hydrostatic pressure. We observed the pressure-dependent flexural phonons for

the first time and quantified the elastic properties and interlayer van der Waals interactions in layered materials. These temperature- and pressure-dependent phonon measurements are significant in studying the strain effects on the anisotropic thermal conductivity and optimizing the materials' thermal transport to enhance their functionality and thermal stability.

Using inelastic neutron scattering, temperature- and pressure-dependent phonon lattice dynamics measurements on PTP were studied. The results indicate strong anharmonic phonon dynamics and suggest a lack of phase transition in the region of 0~1.51 kbar and 10~30 K.

Using Raman scattering, the pressure and temperature-dependent results on FGT were performed, and the significant pressure-induced phonon energy shift was observed. The phonon energy shift may be related to the strong spin-phonon interactions, which may play important roles in its application for magnetic storage devices.

Chapter 2

Theory and Methods

2.1 Phonon Theory

In condensed matter physics, a phonon is a collective excitation in a periodic arrangement of atoms in solids. The concept of phonon was introduced by Soviet physicist Igor Tamm in 1932 and referred to as “sound”, since sound is the long-wavelength acoustic phonon. Analogous to the photon (quantum energy in the electromagnetic field), phonon was suggested for the quantum lattice vibrational energy. Different from photons, phonons are regarded as quasiparticles representing the collective vibrational modes in solids. [171]

A crystalline solid is formed by a periodic array of atoms. An atom or a group of atoms that repeats infinitely is represented as a basis. If the atom or group of atoms is replaced by a point in space, each point is called a lattice point, and the collection of these points is named crystal lattice. Each lattice point can be moved to its identical one by a

translation vector \mathbf{R} , obtained by using three non-coplanar elementary lattice vectors \mathbf{a}_1 , \mathbf{a}_2 , and \mathbf{a}_3 . \mathbf{R} is given by [99]:

$$\mathbf{R} = u_1\mathbf{a}_1 + u_2\mathbf{a}_2 + u_3\mathbf{a}_3, \quad (2.1)$$

\mathbf{a}_1 , \mathbf{a}_2 , and \mathbf{a}_3 construct a parallelepiped, called a unit cell, containing the space between adjacent lattice points as well as the atoms inside. u_1 , u_2 and u_3 are integers. The unit cell can build up the whole crystal without overlaps or voids. When the unit cell has the smallest volume and contains only one lattice point with minimum number of atoms in a basis, it is called a primitive unit cell. A set of discrete translation operations on the lattice vectors could generate a Bravais lattice. Due to the limited possible arrangement of lattice vectors, there are 5 Bravais lattices in two-dimensional space and 14 Bravais lattices in three-dimensional space. The crystal is invariant under translation, including any local physical properties like electron charge concentration. It is more convenient to generate the reciprocal lattice to study the interesting periodic crystal properties. Reciprocal lattice is the Fourier transform of the spatial crystal lattice, and reciprocal lattice points are periodic in k-space or momentum space. A Wigner-Seitz primitive cell in reciprocal space is called a Brillouin zone. The central cell consists of the smallest volume enclosed by the perpendicular bisectors of the elementary reciprocal lattice vectors; it is called the first Brillouin zone.

In real space, the equilibrium position of the unit cell origin is represented as \mathbf{R}_j ; the equilibrium position of the l th atom in unit cell \mathbf{R}_j is represented by \mathbf{R}_{jl} , which satisfy the following equation:

$$\mathbf{R}_{jl} = \mathbf{R}_j + \mathbf{R}_l, \quad (2.2)$$

where \mathbf{R}_l represents the relative position of the l th atom with respect to the unit cell origin. These equilibrium positions are achieved by balancing the attractive and repulsive forces between atoms. However, the atoms are allowed to move and vibrate around their equilibrium positions, more actively at higher temperatures. The lattice vibrations are treated as elastic waves in crystals, and a simple mathematical model is developed to understand their propagating properties. [99] Periodic lattices with n atoms in the unit cell have $3n$ vibrational normal modes (phonon modes). If n is two or larger, the phonon modes are divided into 3 acoustic phonon modes and $3n - 3$ optical phonons modes. Acoustic phonons involve the in-phase atomic vibrations and can be longitudinal and transverse. Longitudinal acoustic (LA) phonons mean that the atoms vibrate along the propagating direction while transverse acoustic (TA) phonons correspond to the vibration perpendicular to the propagating direction. Optical phonons are out-of-phase vibrations of atoms; similar to acoustic phonons, they are abbreviated as LO and TO phonons. The subject pertaining to lattice vibrations is called lattice dynamics. The electrons are much lighter and move much faster than nuclei. For the atomic vibrations in lattices, only the motions of nuclei are considered. Within the Born-Oppenheimer adiabatic approximation, the stationary states of the nuclei can be expressed by the nuclear Hamiltonian as [48, 56, 141]:

$$\widehat{H}_n = - \sum_{jl} \frac{\Delta_{jl}^2}{2M_{jl}} + U, \quad (2.3)$$

As an approximation, the quantum-mechanical momentum can be replaced by its corresponding classical momentum:

$$-i\Delta_{jl} = -i \frac{\partial}{\partial R_{jl}} \rightarrow \mathbf{P}_{jl}. \quad (2.4)$$

We can get the classical nuclear Hamiltonian in the system:

$$\widehat{H}_n^{clas} = \sum_{jl} \frac{\mathbf{P}_{jl}^2}{2M_{jl}} + U, \quad (2.5)$$

where $\sum_{jl} \frac{\mathbf{P}_{jl}^2}{2M_{jl}}$ is the kinetic energy, M_{jl} is the mass of l th nuclei in the j th unit cell. U is the total potential energy of nuclei. The atoms only vibrate with small displacements from their equilibrium positions and their time-dependent instantaneous positions can be expressed as:

$$\mathbf{R}_{jl}(t) = \mathbf{R}_{jl} + \mathbf{u}_{jl}(t), \quad (2.6)$$

where \mathbf{R}_{jl} is the equilibrium position and \mathbf{u}_{jl} is the time-dependent displacement. Using the classical Hamiltonian, Newton's equations can be derived as:

$$M_{jl}\ddot{\mathbf{u}}_{jl} = \frac{\partial U}{\partial \mathbf{u}_{jl}}. \quad (2.7)$$

We can perform the Taylor expansion of the total potential energy, U , up to the second order in the atomic displacements \mathbf{u}_{jl} :

$$U = U_0 + \sum_{jl\alpha} \Phi_{jl}^{\alpha} \mathbf{u}_{jl}^{\alpha} + \frac{1}{2} \sum_{jl\alpha} \Phi_{jlj'l'}^{\alpha\alpha'} \mathbf{u}_{jl}^{\alpha\alpha'} \mathbf{u}_{j'l'}^{\alpha\alpha'} + \dots, \quad (2.8)$$

where α sum over the Cartesian coordinates (x, y, and z). U_0 is related to the total energy corresponding to the nuclei in their equilibrium positions. Φ_{jl}^{α} is the force on each nucleus and is zero in the equilibrium configuration. $\Phi_{jlj'l'}^{\alpha\alpha'}$ are the second-order derivative of U .

Therefore, we can have:

$$\Phi_{jlj'l'}^{\alpha\alpha'} = [\Phi_{jlj'l'}^{\alpha\alpha'}], \quad (2.9)$$

$$U = U_0 + \frac{1}{2} \sum_{jl} \sum_{j'l'} \Phi_{jlj'l'}^{\alpha\alpha'} \mathbf{u}_{jl} \mathbf{u}_{j'l'}, \quad (2.10)$$

which defines the harmonic approximation. $\Phi_{jlj'l'}$ is the second derivative of U and represent the harmonic force constants. Newton's equations within the harmonic approximation can be written as:

$$M_{jl}\mathbf{u}_{j'l''} = -\sum_{j'l'}\Phi_{jlj'l'}\mathbf{u}_{j'l'}. \quad (2.11)$$

It needs to be noted that when the potential energy U is expanded to the third or higher order, the anharmonicity terms are involved and correspond to the phonon-phonon interactions. Descriptions about phonon-phonon interactions and phonon anharmonicity have been reported comprehensively in other works. [88, 149]

Using the periodic boundary conditions and translational invariance of force constants in crystals, the solution of the equation is in the form of a propagating wave with wavevector \mathbf{q} , angular frequency $\omega_{\mathbf{q}s}$, and polarization $\mathbf{e}_{ls}(\mathbf{q})$:

$$\mathbf{u}_{jl}(\mathbf{q}, t) = \sqrt{\frac{2\hbar}{NM_l\omega_{\mathbf{q}s}}}\mathbf{e}_{ls}(\mathbf{q})e^{i(\mathbf{q}\cdot\mathbf{R}_{jl}-\omega_{\mathbf{q}s}t)}, \quad (2.12)$$

where s is the mode index and there are $3n$ phonon modes if there are n atoms in the unit cell. N is the total number of atoms. The real part of the solution is used as the physical atom displacement.

Three-dimensional polarization vectors $\mathbf{e}_{ls}(\mathbf{q})$ provide the relative displacement of the atom l in unit cell j associated with phonon mode s in Cartesian coordinates. [37] Such vectors and angular phonon frequency $\omega_{\mathbf{q}s}$ are eigenvectors and eigenvalues obtained by diagonalizing the dynamical matrix $\mathbf{D}(\mathbf{q})$:

$$\omega_{\mathbf{q}s}^2\mathbf{e}_{ls}(\mathbf{q}) = \mathbf{D}(\mathbf{q})\mathbf{e}_{ls}(\mathbf{q}), \quad (2.13)$$

where $\mathbf{D}(\mathbf{q})$ is the Fourier transform of the force constants $\Phi_{jlj'l'}$:

$$\mathbf{D}(\mathbf{q}) = \frac{1}{\sqrt{M_l M_{l'}}} \sum_{l'} \Phi_{jlj'l'}(\mathbf{q}) e^{i(\mathbf{q} \cdot (\mathbf{R}_{j'l'} - \mathbf{R}_{jl}))}. \quad (2.14)$$

It can be seen that $\omega_{\mathbf{q}s}$ depends on wavevector \mathbf{q} ; this relation forms the phonon dispersion in reciprocal space. The transmission speed of phonons can be represented by group velocity $v_g = (\partial\omega_{\mathbf{q}s})/\partial\mathbf{q}$. In quantum mechanics, it is convenient to treat a phonon with wavevector \mathbf{q} as a quasiparticle with momentum $\mathbf{p} = \hbar\mathbf{q}$ and quantized energy $E = \hbar\omega_{\mathbf{q}s}$. Phonons are bosons and obey the Bose-Einstein distribution:

$$n(\mathbf{q}) = \frac{1}{e^{\frac{\hbar\omega_{\mathbf{q}}}{K_B T}} - 1}, \quad (2.15)$$

where K_B is the Boltzmann constant and T is the absolute temperature. $n(\mathbf{q})$ represents the average number of phonons for a given temperature T . It is often useful to know how many vibrational modes are around a given phonon frequency, called phonon density of states (DOS). Such information is pivotal to studying the phase diagram, specific heat, and thermal conductivity. Phonon density of states $g(\omega)$ is formally defined as:

$$g(\omega) = \frac{1}{N} \sum_{s, \mathbf{q}} \delta(\omega - \omega_{\mathbf{q}s}), \quad (2.16)$$

where N is the number of unit cells. However, $g(\omega)$ does not include the vibrational eigenvectors, which are considered in the weighted DOS [52]:

$$G(\omega) = \sum_l G_l(\omega), \quad (2.17)$$

where $G_l(\omega)$ can be defined as:

$$G_l(\omega) = \frac{1}{3N} \sum_{s, \mathbf{q}} |\mathbf{e}_{ls}(\mathbf{q})|^2 \delta(\omega - \omega_{\mathbf{q}s}). \quad (2.18)$$

2.2 Computation methods

Modern computational methods from first principles have developed rapidly with the breakthrough in theoretical approximations and computational techniques. In solid state physics, the computational science is based upon Density Functional Theory (DFT), which is effective in solving the Schrödinger equation. Such computation is very useful in predicting physical and chemical properties of materials, even under extreme conditions, and providing theoretical explanations to novel experimental observations. In this section, we will briefly review computational methods for phonons. More details about the computational techniques are discussed in many books. [48, 85]

To understand the behavior of quantum particles, their wavefunction $\Psi(\mathbf{r})$ at point \mathbf{r} can be determined by solving the Schrödinger equation. When we want to study many electrons and nuclei together in solid materials, many-body wavefunctions Ψ needs to be determined by including all electrons and nuclei. In this system, the many-body Schrödinger equation in Hartree atomic units ($E_{Ha} = \frac{e^2}{4\pi\epsilon_0}$) can be written as [48]:

$$\left[-\sum_i \frac{\Delta_i^2}{2} - \sum_I \frac{\Delta_I^2}{2M_I} + \frac{1}{2} \sum_{i \neq j} \frac{1}{|\mathbf{r}_i - \mathbf{r}_j|} + \frac{1}{2} \sum_{I \neq J} \frac{Z_I Z_J}{|\mathbf{R}_I - \mathbf{R}_J|} - \frac{1}{2} \sum_{i,I} \frac{Z_I}{|\mathbf{r}_i - \mathbf{R}_I|} \right] \Psi = E_{tot} \Psi, \quad (2.19)$$

where $-\sum_i \frac{\Delta_i^2}{2} - \sum_I \frac{\Delta_I^2}{2M_I}$ is the kinetic energy, $\frac{1}{2} \sum_{i \neq j} \frac{1}{|\mathbf{r}_i - \mathbf{r}_j|}$ is the potential energy related to Coulomb repulsion between electron pairs, and $\frac{1}{2} \sum_{I \neq J} \frac{Z_I Z_J}{|\mathbf{R}_I - \mathbf{R}_J|}$ is the potential energy related to Coulomb repulsion between nuclei pairs, $-\frac{1}{2} \sum_{i,I} \frac{Z_I}{|\mathbf{r}_i - \mathbf{R}_I|}$ is the potential energy related to the Coulomb attraction between electrons and nuclei. i, j and I, J are the indices of electrons and nuclei. m_e and M_I are the masses of electron and nuclei respectively. ϵ_0 is

the permittivity of vacuum, and Z_I represents the atomic number. E_{tot} is the total energy eigenvalue of the system.

In solid systems, we can assume that the nuclei are immobile in their known positions (known as Clamped nuclei approximation), then the dependence on the nuclear coordinates can be ignored. In order to solve equation (2.19), approximation methods have been developed to simplify the problems, such as independent electrons approximation and mean-field approximation. Within the independent electrons approximation, the Coulomb repulsion between electrons pairs is ignored, and the many-electrons Schrödinger equation can be written as:

$$\sum_i \hat{H}(\mathbf{r}_i) \phi_1(\mathbf{r}_1) \dots \phi_N(\mathbf{r}_N) = E \phi_1(\mathbf{r}_1) \dots \phi_N(\mathbf{r}_N), \quad (2.20)$$

where N is the number of electrons in the system, wavefunction $\phi_i(\mathbf{r}_i)$ is the solution of single-electron Schrödinger equation. The electron charge $n(\mathbf{r})$ density represents the possibilities of finding the electrons in state i at point \mathbf{r} and is given as:

$$n(\mathbf{r}) = \sum_i |\phi_i(\mathbf{r})|^2. \quad (2.21)$$

Within the mean-field approximation, adding the terms regarding the exchange interaction between electrons and correlation between electrons in equation (2.20), we finally obtain the famous single-particle Kohn-Sham equations:

$$\left[-\frac{1}{2} \Delta_i^2 + V_n(\mathbf{r}) + V_H(\mathbf{r}) + V_{xc}(\mathbf{r}) \right] \phi_i(\mathbf{r}) = \varepsilon_i \phi_i(\mathbf{r}), \quad (2.22)$$

where $V_{xc}(\mathbf{r})$ is the exchange and correlation functional. $V_n(\mathbf{r}) = -\sum_I \frac{Z_I}{|\mathbf{r}-\mathbf{R}_I|}$ is the Coulomb potential of nuclei. $\Delta^2 V_H(\mathbf{r}) = -4\pi n(\mathbf{r})$ is used to obtain Hartree potential from electron charge. In density functional theory, it is observed that the total energy,

ground state energy E , of a many-electrons system is a functional of the electron density only, known as the Hohenberg-Kohn theorem:

$$E = F[n], \quad (2.23)$$

$$F[n] = \int d\mathbf{r} n(\mathbf{r}) V_n(\mathbf{r}) - \sum_i \int d\mathbf{r} \phi_i^2(\mathbf{r}) \frac{\Delta_i^2}{2} \phi_i(\mathbf{r}) + \frac{1}{2} \iint d\mathbf{r} d\mathbf{r}' \frac{n(\mathbf{r})n(\mathbf{r}')}{|\mathbf{r}_i - \mathbf{r}_j|} + E_{xc}[n]. \quad (2.24)$$

In equation (2.19), the first three terms comprise the total energy, based on the independent electrons approximation, representing external potential, kinetic energy, and Hartree energy, respectively. The relations between $E_{xc}[n]$ and $V_{xc}(\mathbf{r})$ can be expressed as:

$$V_{xc}(\mathbf{r}) = \frac{\delta E_{xc}[n]}{\delta n} \Big|_{n\mathbf{r}}. \quad (2.25)$$

If we know the $E_{xc}[n]$, the exchange and correlational energy, we could calculate $F[n]$ using the electron density of its ground state. Therefore, the question is then how to determine the electron density to get the ground state energy. The contribution from $E_{xc}[n]$ in the total energy is actively involved in, and crucial to the success and accuracy of DFT. The selection of exchange and correlation functionals is the first step in first-principles calculations, and several functionals are available today. The simplest functional is obtained within the local density approximation (LDA). The LDA's is calculated in the simplest model of interacting electrons, the homogeneous electron gas (HEG). In real materials, the electron density in a small region $d\mathbf{r}$ is treated homogeneous, the exchange and correlation energy in this region can be expressed as:

$$dE_{xc} = \frac{E_{xc}^{HEG} n(\mathbf{r})}{V} d\mathbf{r}. \quad (2.26)$$

Adding up the contribution from each small region through the whole volume V , we obtain:

$$E_{xc} = \int \frac{E_{xc}^{HEG} n(\mathbf{r})}{V} d\mathbf{r}. \quad (2.27)$$

We can see that this functional only depends on the local electron density and works well for systems with small variance in electron density over distance. The calculated lattice parameters using LDA are usually smaller than the measured lattice parameters. Other widely used functionals are within the generalized gradient approximations (GGA), which work better for systems having stronger electron density gradients. The commonly used forms include PW91 (Perdew -Wang 91) and PBE (Perdew-Burke-Ernzerhof). GGA usually overestimate the calculated lattice parameters. The selection principle about LDA and GGA is empirical and depends on the material system.

In many cases, it is more convenient to use DFT by describing the valence electrons only. The electrons in core state are tightly bound to the nucleus and only valence electrons dominate in the chemical bonding. The potential is modified so that the solution of the Kohn-Sham equation gives a smooth pseudo-wavefunction that eliminates the oscillating structure in the all-electron wavefunction. Such potential is named “pseudopotential” and the PAW (projector augmented wave) potential is used in our DFT calculations. More information about can be found in books. [23]

After the introduction of DFT and the Kohn-Sham equation, we can use these theoretical techniques to calculate the total energy, electron density in the ground state by using self-consistent calculations, which is based on equations (2.22), (2.21), and (2.25). The first guess for electron density is plugged into equation (2.22) to get a wave function which, in turn, gives a new electron density of the system. The new electron density will be used again for the calculation if it is not equal to the older one. Such optimized iterative

procedure will yield the ground-state electron density and total energy, which is then used for the atomic force and phonon calculations.

In order to perform the first-principles calculation within DFT, Vienna Ab initio simulation package (VASP) [76] was used. Since VASP codes could not provide the information about lattice dynamics, Phonopy package [137] was used by implementing supercell with finite displacement or DFPT methods to get the harmonic force constants, phonon dispersions and phonon DOS.

2.3 Inelastic scattering techniques

2.3.1 Raman scattering

Raman scattering is the inelastic scattering of photons where the frequency of the scattered photon differs from the incident one. It is one of the most powerful tools for studying the vibrational properties in solids and molecules. A custom-built open-bench Raman spectrometer at 532 nm laser excitation was used as our Raman scattering system. Before being focused on the sample, the laser beam is controlled by various components such as mirrors, waveplate, polarizer, irises, and beam expander on the optical table. When the laser light interacts with matter, the photons that make up the light may be absorbed, scattered, or may not interact with the material and may pass through it. It is an inherently weak process in that only one in every $10^6 - 10^8$ photons is Raman scattered. A long-working-distance microscope objective lens was used for focusing and light collection in the reflective geometry, while a notch filter was employed to remove the Rayleigh scattering. Usually, Raman Scattering is recorded only on the low-energy side to give Stokes scattering:

a process in which the ground vibrational state of the molecule absorbs energy and is promoted to an excited vibrational state with higher energy. Raman spectroscopy uses a single frequency of radiation to irradiate the sample. The radiation scattered from the molecule is detected. The energy unit is wavenumber: the number of waves in a unit of distance. The CCD camera would capture these photon signals and convert them into electronic signals so that the information would be received and processed by the LightFiled software on the computer.

2.3.2 Inelastic neutron scattering (INS)

Neutrons are the essential part of the nuclei of atoms (except the hydrogen atom). The mass of a neutron is $1.674927351 \times 10^{-27}$ kg, and the energies and momenta of neutrons are comparable with those of phonons in condensed solids. INS has been widely used in measuring the lattice dynamics and spin dynamics in materials. In the scattering process, momentum and energy conservation need to be satisfied, and the energy and momentum transfer of a neutron can be calculated as: $\Delta E = E_i - E_f$ and $\Delta \mathbf{Q} = \mathbf{Q}_i - \mathbf{Q}_f$, where E_i and \mathbf{Q}_i are the energy and momentum of the incident neutron, and E_f and \mathbf{Q}_f are the energy and momentum of scattered neutron. We used the Vibrational Spectrometer (VISION) at the Spallation Neutron Source (SNS) to collect data. VISION is an indirect geometry inelastic neutron spectrometer that uses a white beam of incident neutrons with two banks of seven analyzer modules, equipped with curved pyrolytic graphite analyzer arrays that focus neutrons on two large detectors at near-90-degree scattering angles.

2.3.3 Inelastic X-ray scattering (IXS)

IXS spectrometer in Sector 30ID in Advanced Photon source, Argonne National Laboratory, is used to measure the dynamic structure factor at the points in energy and momentum space. The optical layout of the high-energy resolution inelastic X-ray (HERIX) spectrometer and the white beam components. Three stations are in sector 30 of Advanced Photon Source [121]:

1. Section-A (FOE) contains white beam components and high-heat-load monochromator.

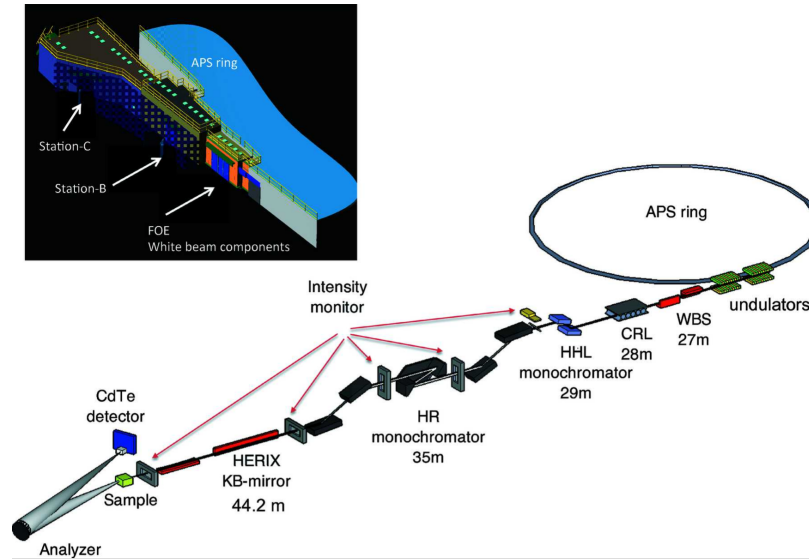


Figure 2.1: Schematic for the 30-ID beamline layout. [121]

2. Section-B houses the high-resolution monochromator.
3. Section-C contains the actual spectrometer, including optics, sample environments, and analyzer systems.

The APS ring accelerates the injected electrons to high energy states. The undulators consisting of a periodic structure of dipole magnets and the electrons are forced to oscillate in the magnetic field and emit synchrotron radiation in the form of ultrabright X-ray. WBS and CRL are the abbreviation of white beam slits and compound refractive lens. High-heat loaded (HHL) monochromator is designed to reduce the heat load on high-resolution (HR) monochromator because the high-power X-ray from undulator would damage spectrometer components. Meanwhile, the wide bandwidth of X-ray was narrowed from kiloelectronvolt (keV) to electronvolt (eV). The HR monochromator further reduce the energy bandwidth to a millielectronvolt (meV) level. A 12-element bimorph Kirkpatrick–Baez mirror system focus the X-ray beam to a few micrometers with a spot of $35 \times 15 \mu\text{m}^2$ ($H \times V$) on the sample. The scatted photons are received by the analyzer and sent to the detector, which gives us the counts information and scattering intensity. Since the detector could not overlap with the sample, we can only work near back scattering geometry by arranging a long scattering arm and small separation between sample and detector. Details about the development of IXS could be found in the referred works. [121, 13]

Compared with INS, the most important characteristic of IXS is the ability to probe small samples due to the high-efficient focusing system, high flux and high brilliance of modern X-ray sources. Such characteristic allows the measurements on small crystals (in micrometer size) and reduce the cost in discovering new materials. It also promotes the growing field of high-pressure research. We have conducted polarization-, pressure-, and temperature- dependent X-ray scattering phonon measurements on different systems.

In the following part of this section, the methods and techniques for controlling X-ray polarization and are briefly discussed.

2.3.4 Control of X-ray polarization

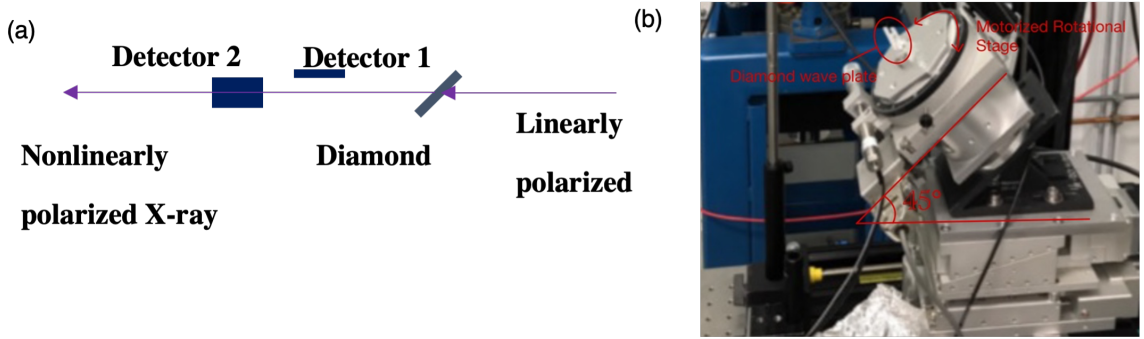


Figure 2.2: Schematic of X-ray Phase Retarder (XPR) setup. (a) Measurement of X-ray polarization. The purple arrows represent the X-ray beam, I_H and I_V are measured by detector 1 and 2 respectively. (b) Image of the diamond crystal phase retarder.

A general setup of a diffractive XPR and analyzing method is used, [133] also shown in Figure 2.2. A high-quality diamond single-crystal substrate with a thickness of 950 μm is mounted on a rotation stage and aligned near Bragg condition with its diffraction plane 45 degrees from the horizontal plane. Phase retardation between the two decomposed components of X-ray beam occurs near the Bragg condition for (4 0 0) in the diamond substrate. Final polarization states can be controlled by rotating the deflected angle, $\Delta\theta$. Here $\Delta\theta = \theta - \theta_B$ is the deflected angle from Bragg condition, θ_B is the Bragg angle. Degree of X-ray linear polarization, P_L , is defined as:

$$P_L = \frac{I_H - I_V}{I_H + I_V} = \cos \delta_{exp}, \quad (2.28)$$

and the degree of circular polarization, P_C , is defined as:

$$P_C = \sin \delta_{exp}, \quad (2.29)$$

where I_H is the horizontal intensity, I_V is the vertical intensity, and δ_{exp} is the experimental phase retardation. I_H and I_V are measured by detectors installed on the top and side of X-ray beam, respectively, using Thomson scattering from air. Detector background is subtracted, and the intensity is normalized by the detector efficiency.

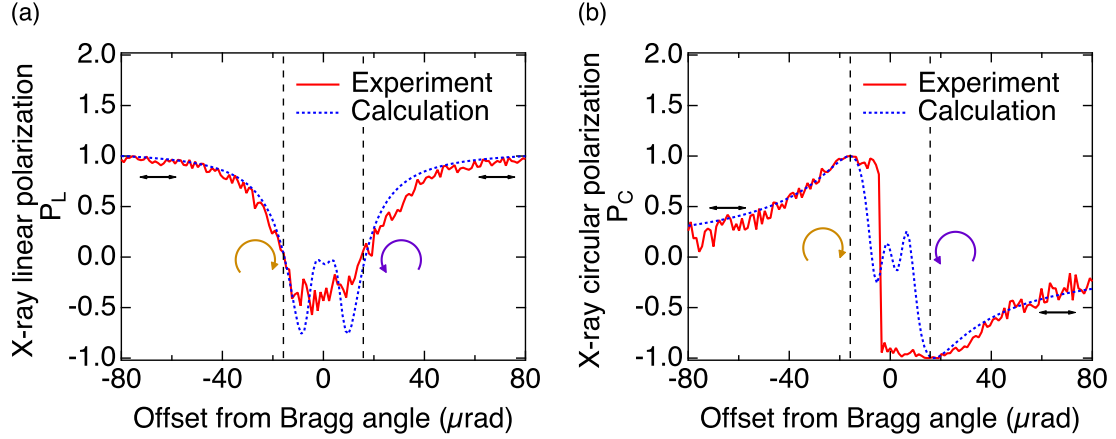


Figure 2.3: Accurately controlled X-ray polarization by a diamond XPR. (a) The degree of linear polarization with respect to the deflected angle. (b) The degree of circular polarization with respect to the deflected angle.

The measured X-ray linear polarization P_L and circular polarization P_C with respect to the deflected angle agree well with the expected result from simulation, as shown in Figure 2.3 (a) and (b). Phase retardation δ , P_L , and P_C are calculated as following [133]:

$$\delta = -\frac{\pi}{2} \left[\frac{r_e^2 \text{Re}(F_h F_h^-) \lambda^3 \sin(2\theta_B)}{\pi^2 V^2 \Delta\theta} \right] \frac{t}{\cos \theta}, \quad (2.30)$$

$$P_C = \sin \delta, \quad (2.31)$$

$$P_L = \cos \delta, \quad (2.32)$$

where r_e is electron radius, F_h and $F_{\bar{h}}$ are the structure factor of hkl and $\bar{h}\bar{k}\bar{l}$ reflections, V is the unit-cell volume, λ is the X-ray wavelength, t is the thickness of the phase plate. X-ray is fully circular polarized at $\pm 15.8 \mu rad$ (dashed black lines). Producing circularly polarized X-ray with meV bandwidth is challenging due to the effects of high energy-resolution monochromator, such as increased beam divergence, and was not previously done to our knowledge. The broadening is observed in the measured polarization in Figure 2.3 due to the beam divergence. Deflected angles of $\pm 28.35 \mu rad$ and $\pm 16.94 \mu rad$ ($P_C = \mp 0.76$ and ∓ 0.99) are used for chiral phonon measurement. The value of the degree polarization is limited by the availability of beamtime and low counts.

Chapter 3

Chiral Phonon Measurement

3.1 Direct observation of chiral phonons in WC by IXS

Chiral phonons break the traditional cognition of linear atomic vibrations and have been extensively studied theoretically. Despite the experimental efforts, characterization of the phonon chirality in full Brillouin zones is still not possible due to the lack of suitable tools. Here, we report an investigation of phonon dispersion and chirality of tungsten carbide by non-resonant millielectronvolt-energy-resolution IXS. For the first time, we observed anomalous IXS by circularly polarized phonons at the corners of hexagonal Brillouin zone and attributed the anomaly to phonon chirality. We also controlled the X-ray polarization successfully and proved that X-ray polarization and phonon chirality play significant roles in the scattering process. Our first-principles simulations, in excellent agreement with phonon dispersion measurement, confirmed the phonon chirality at the zone corners and failed in reproducing the scattering intensities of chiral phonons. The results suggest that a revision to the textbook X-ray scattering function of phonons to consider chirality and X-ray

polarization is needed. Our work paves a new avenue of characterizing chiral phonons and investigating the effects of phonon chirality in phonon-phonon interactions and phonon-spin interactions for applications in novel phononic quantum devices.

3.1.1 Introduction

Circularly polarized phonons, also called chiral phonons, exhibit eigenmodes with circular atomic vibrations and have been theoretically predicted and experimentally observed in some 2D materials. [168, 166] Phonon chirality plays a significant role in controlling the entanglement of quantum dots, generating thermal hall effect, and assisting intervalley or intravalley electron-phonon scatterings.[28, 53, 163] It is also reported that chiral phonons may be exploited for valleypin manipulation [90] or as a messenger to transport information on chirality and angular momentum. [24] Great efforts have been made to identify and quantify chiral phonons and related physical phenomena by infrared circular dichroism and Raman scattering. [26, 38, 157] However, these methods remain indirect and do not allow characterizing chirality throughout the full Brillouin zone (BZ). To date and in this study, non-resonant meV-energy-resolution IXS techniques have usually utilized linearly polarized phonons. The dynamical structure factor of linear phonons is well predicted by the scattering function based on the Born approximation.[12, 138, 2] Recently, the effect of symmetry breaking on the phononic dispersion in chiral magnets has been studied by IXS and is attributed to the phonon chirality. [108] However, the role of phonon chirality and X-ray polarization in the scattering process have not been discussed or studied using IXS.

To produce phonon eigenstates with angular momentum, inversion symmetry needs to be broken. [166, 33] Tungsten carbide (WC), with a space group of $P\bar{6}m2$ (*No.*187), has three-fold rotational and broken inversion symmetry, as shown in Figure 3.1 (a). The K point in BZ (Figure 3.1 (b)) is not equivalent to its reversed K' (-K) point without inversion symmetry, as shown in Figure 3.2. Consequently, WC is an ideal candidate for investigating

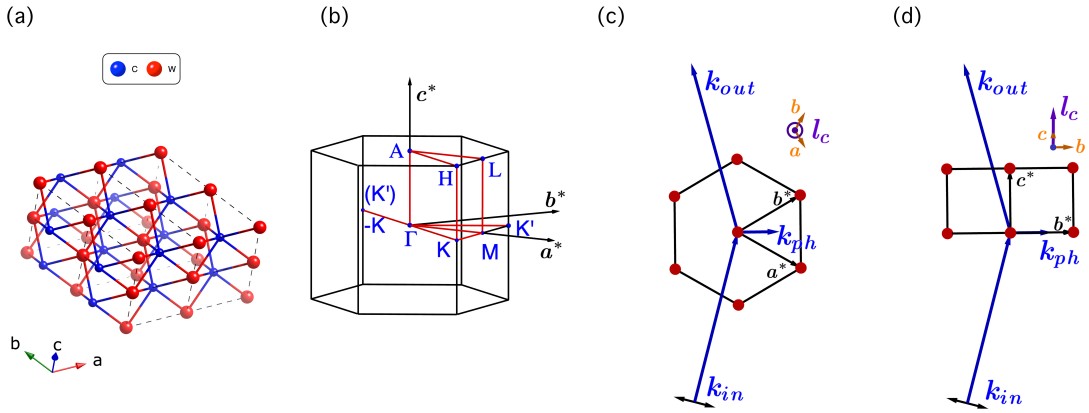


Figure 3.1: Lattice structure of WC and scattering schematic. (a) WC has a hexagonal lattice structure. Red and blue spheres represent tungsten atoms and carbon atoms, respectively. (b) K and K' are distinguished in the Brillouin zone, indicating the broken inversion symmetry. (c)-(d) In-plane scattering geometry and out-of-plane scattering geometry are designed and plotted in the reciprocal space. Red balls in (c) and (d) represent the reciprocal lattice points; k_{in} , k_{out} , and k_{ph} represent the wavevector of incident electric field, scattered electric field and phonon in the inelastic scattering process. Direction of phonon angular momentum along c-axis, l_c , is represented by purple arrows in (c) and (d). The black arrows indicate the polarization of incident X-ray.

phonon chirality in the bulk lattice. [33] Additionally, even though the phonon transport properties of WC have been studied by first-principles calculations using the phonon Boltzmann transport equation, [98, 54, 81] no phonon dispersion measurement on the material has been performed to the best of our knowledge. Lattice dynamics measurements of WC would provide valuable information on its thermodynamic properties and phonon chirality.

In this work, phonon measurement was performed on WC by using IXS along several high symmetry directions in the BZ. The density of state (DOS) of acoustic phonons was also measured by inelastic neutron scattering (INS). Anomalous IXS by in-plane longitudinal (LA) and transverse acoustic (TA) phonons was observed at K and K' points. The anomaly was attributed to the chirality of these phonon modes. In addition, we observed that X-ray polarization could affect the scattering intensities by chiral phonons apparently. The discovery educes that phonon and X-ray polarizations play significant roles in the X-ray scattering process. The results also provide insights on the utilization of IXS in probing phonon chirality and suggest that a revision of the scattering function to consider chirality is needed. This work paves a new avenue of characterizing chiral phonons and investigating the effects of phonon chirality in phonon-phonon interactions and phonon-spin interactions for applications in novel phononic quantum devices.

3.1.2 Experiment and Calculation

Inelastic X-ray scattering measurements. Phonon measurement was conducted at the HERIX spectrometer at APS. Single crystals (typical size of $200 \times 300 \mu m^2$) were purchased commercially (KENNAMETAL [1]). The high quality is revealed by the rocking curve in Figure 3.2 (c). The sample was attached to a copper post by GE varnish and the copper post was mounted on a 4-axis rotation and 3-dimension translation stage. A photon energy of 23.7 keV (wavelength at 0.5226 \AA) was used. The instrument has an energy resolution of 1.5 meV (full width at half maximum). [120] The momentum resolution (\mathbf{Q} -resolution) of the instrument is 0.65 nm^{-1} and ensures the alignment accuracy for measuring the selected wavevector points. When choosing the \mathbf{Q} point at $(2 \ 0 \ 0)$, the

relative accuracy can be represented as $(2 \pm 0.03 \ 0 \ 0)$ in r.l.u. The beam is focused on a spot of $35 \times 15 \ \mu\text{m}^2$ ($H \times V$) on the sample. The thickness of the sample was optimized

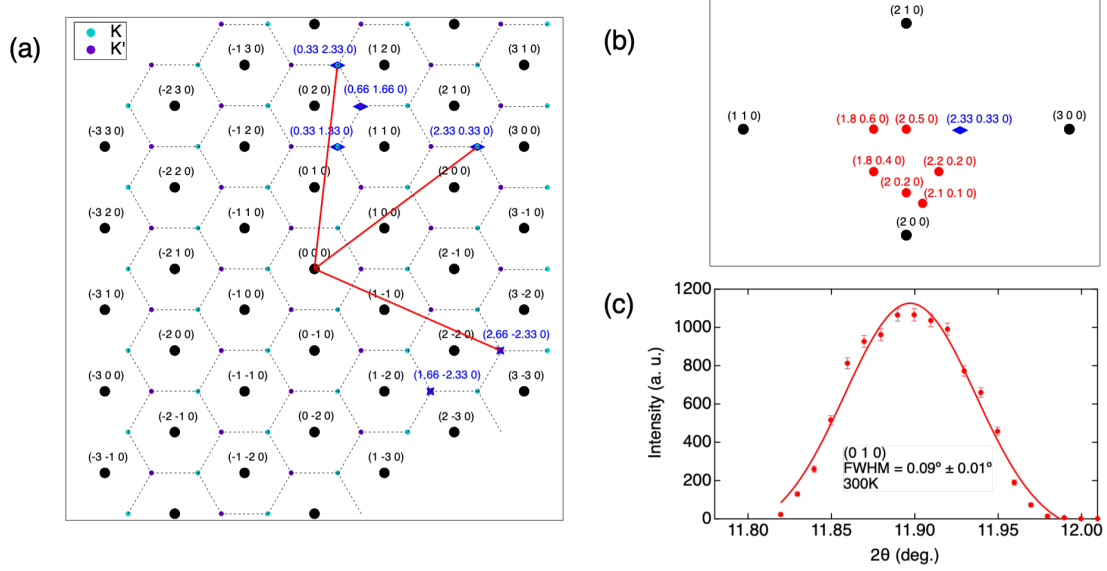


Figure 3.2: In-plane reciprocal space map and the measured K/K' points. The blue rhombuses represent K/K' points measured in the in-plane scattering geometry, while the blue stars represent the K' points measured in the out-of-plane scattering geometry. The red arrows indicate the same $|\mathbf{Q}|$ of these three K/K' points. (b) Measured \mathbf{Q} points away from K/K' points. (c) The rocking curve of WC single crystal measured by HERIX shows the high crystalline quality.

for transmission measurements. The X-ray energy loss spectrum was collected by scanning the energy of the high-resolution monochromator. [135] CdTe Pilatus3 area detectors were used for data collection. [121] All measurements were conducted at room temperature. The X-ray polarization was controlled by a diffractive diamond XPR (Discussed in Chapter 2) .[133] The XPR further decreased the beam flux, so counting time at each polarization was increased significantly due to the low statistics. Because of the scarcity of the beam-

time, the experiment was designed to maximize the information obtained within the limit of beamtime. The data presented was collected through three beamtime experiments.

Super-resolution method is applied to extract the intrinsic phonon linewidth by removing the instrumental resolution in energy and momentum from IXS results. Phonon peaks in IXS spectra are fitted by Voigt function. The measured phonon peak is regarded as a convolution of phonon spectra and resolution functions, as shown in equation (3.1):

$$f_{Phonon} \otimes f_{Resolution} = f_{Experiment}. \quad (3.1)$$

We can deconvolve the phonon peak in raw IXS spectra by resolution function to get the phonon spectrum. The deconvolution process is based on a single mode approximation. [91] Usually, the resolution function is obtained from the energy resolution and momentum resolution functions as shown in equation (3.2):

$$f_{Energy} \otimes f_{Momentum} = f_{Resolution}, \quad (3.2)$$

where f_{Energy} is measured experimentally and $f_{Momentum}$ is the momentum resolution and calculated and regarded as a Gaussian function. FWHM of $f_{Momentum}$ is obtained as:

$$FWHM_{Momentum} = \frac{|dE|}{|d\mathbf{Q}|}, \quad (3.3)$$

where $\mathbf{Q}_{res}=0.65nm^{-1}$, $\frac{|dE|}{|d\mathbf{Q}|}$ is the dispersion slope. Equation (3.3) is used to have the $FWHM_{Momentum}$ in meV unit, which is consistent with the unit of the energy resolution function. The $f_{Momentum}$ can be defined using the obtained $FWHM_{Momentum}$. $\Gamma_{Experiment}$, $\Gamma_{Resolution}$, and Γ_{Phonon} represent the FWHM of $f_{Experiment}$, $f_{Resolution}$, and f_{Phonon} . The linewidth of each function is obtained and listed in Table 3.1.

Inelastic neutron scattering measurements. Powder INS measurement was performed on the time-of-flight direct geometry neutron spectrometer, Hybrid Spectrometers (HYSPEC) [162], at the SNS at Oak Ridge National Laboratory. The measurement was performed at 300 K with an incident energy E_i of 35 meV. The data were reduced using Mantid. [8]

First-principles calculations. First-principles calculations were performed with the density-functional theory (DFT) as implemented in the Vienna Ab initio simulation package (VASP). [76] The exchange correlation function with the generalized gradient approximation in the Perdew-Burke-Ernzerhof flavor (GGA-PBE) [112] and the projector-augmented-wave (PAW) potentials were used. The kinetic cutoff energy with 800 eV was used for plane wave expansion in reciprocal space with a k-point mesh of $12 \times 12 \times 12$. The threshold for the total energy convergence was 10^{-8} eV. The lattice constants obtained from relaxation ($a = b = 2.911 \text{ \AA}$, $c = 2.859 \text{ \AA}$) are slightly larger in c-axis compared to our experimental value ($c = 2.844 \text{ \AA}$, obtained from the Bragg peaks in IXS measurement). The phonon dispersion within the harmonic approximation was calculated using Phonopy. [137] Second-order force constants were calculated by the finite displacement method in supercells ($3 \times 3 \times 3$) containing 54 atoms.

Multiple scattering analysis. The ZA mode in the IXS spectra is a fully linear phonon mode with a polarization not allowed in one-phonon coherent scattering at K' (2.66 -2.33 0). This is because its eigenvector is polarized along the c-axis and its intensity is expected to be zero according to equation (3.8). The measured ZA intensity at (2.66 - 2.33 0) may come from a multiple scattering process, in which a Bragg reflection (h k l) is

also allowed at a particular momentum transfer (m n o). In this case, elastically scattered photons are inelastically scattered for a second time by phonons at (m-h n-k o-l), giving scattering intensity from a forbidden phonon mode. [4]

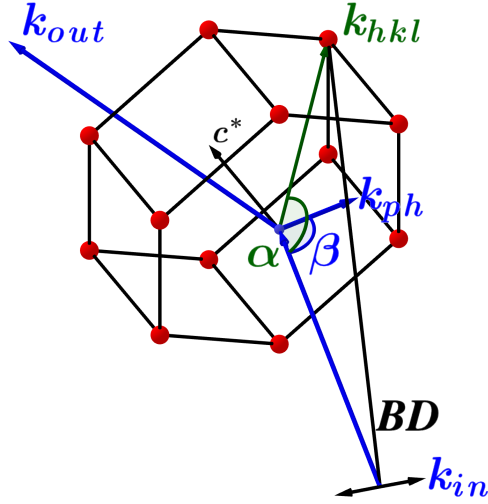


Figure 3.3: Schematic of a multiple scattering process. Triangle formed by BD , $|k_{in}|$, and $|k_{hkl}|$ is plotted in green color.

Figure 3.3 shows a simplified inelastic scattering schematic for multiple scattering in reciprocal space. Incident photons with a wave vector k_{in} were scattered to k_{out} with a wave vector transfer of k_{ph} . Some incident photons were also scattered elastically with a wave vector transfer of k_{hkl} . Furthermore, k_{in} , k_{out} , k_{ph} , and k_{hkl} are known in reciprocal space and are represented in the same Cartesian coordinates. They satisfy:

$$\cos \alpha = \frac{|k_{hkl}|^2 + |k_{in}|^2 - |BD|^2}{2|k_{hkl}||k_{in}|}, \quad (3.4)$$

$$2\theta_{hkl} = 2 \times \left(\alpha - \frac{\pi}{2} \right), \quad (3.5)$$

here α is the angle opposite to the side BD in Figure 3.3. The Bragg condition is satisfied when the calculated α from equation (3.4) could meet the requirement in equation (3.5).

At (2.66 -2.33 0) in the out-of-plane scattering geometry, another Bragg reflection at (-3 -2 5) happens to be at Bragg condition. The elastically scattered photons are then inelastically scattered again by ZA phonons at (5.66 -0.33 -5). As a result, the secondary inelastic scattering from (5.66 -0.33 -5) contributes to the measured ZA mode in Figure 3.8 (a). We also performed intensity simulation at (5.66 -0.33 -5) and found that intensity of ZA is much larger than that of TA and LA. In this simulation, TA and LA also have the same intensity and their intensity relation is consistent with the simulation at other K or K' points. These calculations suggest that the second order scattering does not influence the observations using linearly and nonlinearly polarized X-ray.

3.1.3 Results and Discussion

Phonon dispersion, DOS, and linewidth

Phonon dispersion measured by IXS (details in “Methods”) was along Γ -M-K- Γ -A directions in reciprocal space, as shown in Figure 3.4 (a). The first-principles calculations (details in “Methods”) agree well with our IXS measurement of acoustic phonons, with some minor underestimation of the phonon energy along M-K- Γ directions. This underestimation may result from the slightly larger relaxed lattice parameters. Additionally, the current calculation agrees better with the experimental measurement along Γ -M direction than the prior calculation from Ref. [54]. The phonon linewidths at most measured **Q** points are limited by instrument resolution for extraction using super-resolution method.

IXS measurement at most \mathbf{Q} points are resolution limited except for the listed \mathbf{Q} points in Table 3.1. These extracted phonon linewidths are not reliable because of the narrow phonon linewidths.

Table 3.1: Phonon linewidth obtained by super-resolution method.

\mathbf{Q} points	Phonon mode	$\Gamma_{Experiment}$ (meV)	$\Gamma_{Resolution}$ (meV)	Γ_{Phonon} (meV)
(2 0.2 0)	TA	3.3 ± 0.8	2.3	2.2 ± 0.5
	LA	4.0 ± 0.4	3.9	2.5 ± 0.3
(1.8 0.6 0)	TA	2.0 ± 0.9	1.6	1.1 ± 0.5
	LA	2.7 ± 1.1	1.5	2.1 ± 0.8
(1.8 0.4 0)	TA	3.1 ± 1.1	2.3	1.8 ± 0.6
(1.66 -2.33 0)	TA	1.8 ± 0.5	1.5	1.0 ± 0.3
	LA	1.8 ± 0.3	1.5	1.0 ± 0.2
(2.66 -2.33 0)				
	LA	1.8 ± 0.8	1.5	1.0 ± 0.4

Acoustic part of the phonon DOS measured by INS also shows decent agreement with the calculation (Figure 3.4). The peak near 25 meV is dominated by the TA branch and the peak about 30 meV corresponds to the LA branch. The small observed difference with the calculation comes from the instrument resolution and neutron weighting. In general,

the IXS and INS measurements confirm the accuracy of the first-principles calculation for acoustic phonons.

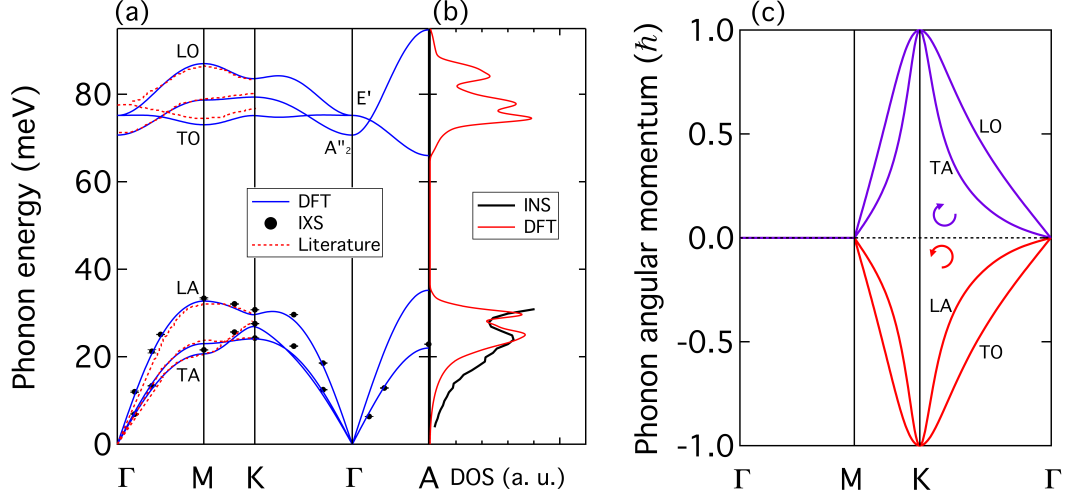


Figure 3.4: Phonon dispersion, DOS, and phonon angular momentum of WC. (a) Phonon dispersion of WC from DFT calculation agrees well with experimental measurement. There are three acoustic and three optical phonon branches. Calculated phonon dispersion relations are plotted in lines and IXS measurement is represented by black symbols. The error bars indicate the fitting error of phonon energy in IXS spectra. The red dashed dispersion lines are from Ref. [54]. (b) Measured acoustic phonon DOS of WC agrees well with DFT calculation. The solid red line represents the calculated total DOS of WC; the black line represents the (neutron-weighted) DOS below 30.9 meV measured by INS. (c) Phonons near K/K' points are circularly polarized. Phonon angular momentum is plotted by purple and red lines along in-plane high symmetry directions. The purple and red colors represent positive and negative value of angular momentum respectively.

Phonon polarization

According to first-principles calculations, phonons at K and K' points have the largest angular momenta and are fully circularly polarized, as shown in Figure 3.4 (c).

Circular atomic vibrations of chiral phonons can be visualized (Figure 3.4) by calculating the

time-dependent atomic displacement from equation (2.12). As a result, three-dimensional eigenvectors of chiral phonons are complex. In-plane LA and TA modes are associated with the atomic motions in the basal plane (a-b plane in real space shown in Figure 3.1 (a)), indicating that direction of angular momentum is along c-axis. Phonon angular momentum along c-axis of sth mode with reduced momentum at \mathbf{q} , $l_c(\mathbf{q}, s)$, can be calculated from equation (3.6) [165, 55]:

$$l_c(\mathbf{q}, s) = \hbar(e_{\mathbf{q}s}^\dagger \mathbf{M}_c e_{\mathbf{q}s}), \quad (3.6)$$

here $\mathbf{M}_c = \begin{pmatrix} 0 & -i & 0 \\ i & 0 & 0 \\ 0 & 0 & 0 \end{pmatrix} \otimes I_{n \times n}$ and n is the number of atoms in one unit cell. $e_{\mathbf{q}s}$ is the eigenvector of sth phonon mode with reduced momentum at \mathbf{q} , $\omega_{\mathbf{q}s}$ is the corresponding eigenvalue.

Near the K points (nonlinear region), TA and LO modes are dominantly clockwise circularly polarized, showing positive angular momentum along the c-axis; LA and TO modes are anticlockwise circularly polarized, showing negative angular momentum along c-axis. On the other hand, near the K' points, the equivalent phonon modes show opposite polarizations. The total angular momentum of these phonon modes throughout the full Brillouin zone is zero. TA and LA modes have opposite polarization at any given q point, so do LO and TO modes. Figure 3.5 shows the animations of TA and LA modes at K and K' points. TA mode shows clockwise circular vibrations at K point; LA mode shows anticlockwise circular vibrations. TA and LA modes have opposite circular polarization at K'.

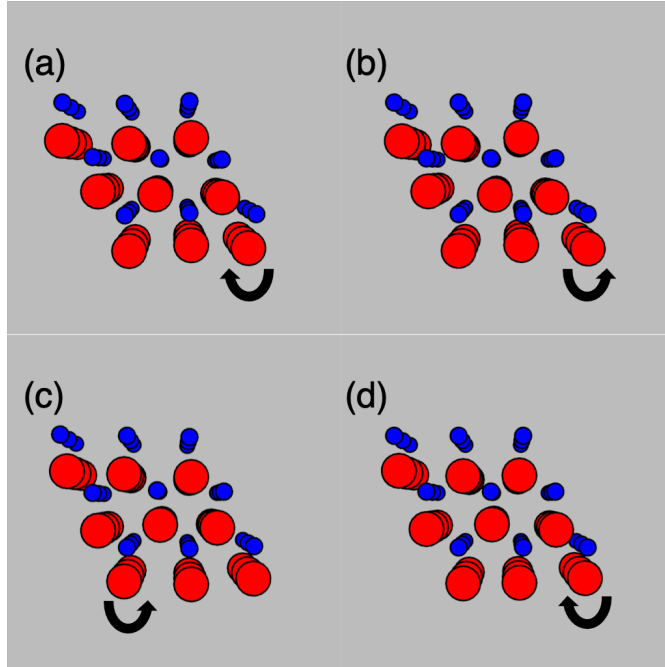


Figure 3.5: Animations of TA and LA modes at K and K'. (a) and (b) Animations of TA and LA at K points. (c) and (d) Animations of TA and LA at K' points. Red and blue spheres represent tungsten atoms and carbon atoms, respectively. The animations are generated by ascii-phonons. [63]

Anomalous inelastic scattering of X-ray

In IXS experiments, X-ray from high-resolution monochromator was horizontally linearly polarized. [121] In-plane and out-of-plane scattering geometries were used to measure the scattering geometry-dependent dynamical structure factor. IXS spectra at some K points $((0.33 \ 2.33 \ 0)$, $(0.33 \ 1.33 \ 0)$ and $(2.33 \ 0.33 \ 0)$) and K' point $((0.66 \ 1.66 \ 0))$ (plotted in reciprocal space in Figure 3.2 (a)), were obtained in the in-plane scattering geometry (Figure 3.1 (c)). Additionally, an out-of-plane scattering geometry in Figure 3.1 (d) was used to measure the spectra at another two K' points $((2.66 \ -2.33 \ 0)$ and $(1.66 \ -2.33 \ 0)$, shown in Figure 3.2 (a)). Measurements of the same K' or K points in both in-plane and

out-of-plane scattering geometries are not possible due to the instrument constrain so the points with equivalent $|\mathbf{Q}|$ are used. For the in-plane scattering geometry, the basal plane of the crystal was oriented parallel to the plane of electric field vectors of the incident X-ray beam. For the out-of-plane scattering geometry, the basal plane of the crystal was oriented perpendicular to the plane of electric field vectors of the incident X-ray beam.

Anomalous IXS by chiral phonons is observed at Brillouin zone boundary (K and K' points). Such anomaly depends on the scattering geometry. The results show that the scattering function based on the Born approximation [12] reliably reproduces the scattering intensity of linearly polarized phonons and the circularly polarized phonons measured in the in-plane scattering geometry (Figure 3.6 and Figure 3.7) but fails in predicting the intensity of circularly polarized phonons measured in the out-of-plane scattering geometry (Figure 3.8). To qualify such anomaly, phonon peaks in IXS spectra are fitted by Voigt functions and the area ratios between the LA and TA modes, $\frac{S_{LA}}{S_{TA}}$, are calculated. The ratios are then compared with the ones from the simulated dynamical structure factor, $S(\mathbf{Q}, \omega)$, which is obtained from the partial differential cross section, as shown in equation (3.7) [12, 129]:

$$\left(\frac{\partial^2 \sigma}{\partial \Omega \partial E} \right)_{k\varepsilon_\alpha \rightarrow k'\varepsilon_\beta} = \frac{k'}{k} r_e^2 \times |\varepsilon_\alpha^* \cdot \varepsilon_\beta|^2 S(\mathbf{Q}, \omega), \quad (3.7)$$

where \mathbf{Q} is the total wave vector transfer, ω is the phonon angular frequency. Photons are scattered from the initial state with wavevector k and polarization ε_α^* to a final state k' and ε_β , and r_e is the electron radius. No change of photon polarization is involved, and the partial differential cross section is directly proportional to the dynamical structure factor, $S(\mathbf{Q}, \omega)$. If considering one-phonon coherent scattering with photon energy

loss (phonon creation) process, IXS intensities of LA and TA phonons were calculated by [12, 129]:

$$S(\mathbf{Q}, \omega)_{1p} = N \sum_{\mathbf{q}} \sum_s \sum_d \times \left\{ \left| \frac{f_d(\mathbf{Q})}{\sqrt{2M_d}} e^{-W_d(\mathbf{Q})} e^{i\mathbf{Q} \cdot x_d} (\mathbf{Q} \cdot e_{\mathbf{q}sd}) \right|^2 \right\} \frac{\langle n_{\omega_{\mathbf{q}s}} + 1 \rangle}{\omega_{\mathbf{q}s}}, \quad (3.8)$$

where N is the number of unit cells, \mathbf{q} is the reduced momentum transfer determined by $\mathbf{q} = \mathbf{Q} - \tau$ (τ is the momentum transfer for Bragg reflections), d is the index of atoms in the primitive cell locate at X_d , s is the index of phonon modes, M_d is the atomic mass, $f_d(\mathbf{Q})$ is the X-ray atomic form factor, [19] $\omega_{\mathbf{q}s}$ is the phonon angular frequency, $e_{\mathbf{q}sd}$ is the phonon polarization vector, $n_{\omega_{\mathbf{q}s}}$ is the Bose occupation, and $e^{-W_d(\mathbf{Q})}$ is the Debye Waller Factor. The spectra calculated by the equations above are checked again with the results from Phonopy and found to be consistent. It should be noted that this formalism does not take the angular momentum of circularly polarized phonons into account. For comparison, the simulated spectra are rescaled so that its TA mode shows the same intensity as the experimental ones.

At \mathbf{Q} points away from K and K', simulation matches well with the measurement (Figure 3.6). At K and K' points in the in-plane scattering geometry, as shown in Figure 3.7, the simulation is consistent with the measurement as well. The similar intensities of TA and LA modes are generally expected, within measurement statistics. However, for K' points in the out-of-plane scattering geometry, as shown in Figure 3.8, the measurement is significantly different from the simulation: the intensity of LA mode at (2.66 -2.33 0) and (1.66 -2.33 0) is much stronger than that of TA mode.

For the same phonon mode, its scattering intensity is expected to be the same at $(2.33 \ 0.33 \ 0)$, $(0.33 \ 2.33 \ 0)$, and $(2.66 \ -2.33 \ 0)$ based on equation (3.8) because they have equivalent $|\mathbf{Q}|$ transfer and the phonon eigenvectors are in the same norm. Consequently, the intensity relation between LA and TA should be the same for the three points. It should be noticed that the two phonon modes are fully circularly polarized at these K and K' (Figure 3.4 (c)). The obvious discrepancy between simulation and experiment is likely due to the phonon chirality. The discrepancy also reveals that equation (3.8) fails in reproducing the IXS scattering intensities of chiral phonons in the out-of-plane scattering geometry.

The failure of the scattering simulation possibly originates from two sources. Firstly, the calculated cross section, equation (3.7), assumes that photon polarizations ε_α and ε_β are conserved before and after the scattering by phonons, which works well for linear phonons. However, when phonons carry angular momentum, the creation or annihilation process may involve the transfer of angular momentum between photons and phonons. In this case, the photon polarizations ε_α and ε_β might not be the same. Secondly, in equation (3.8), $S(\mathbf{Q}, \omega)$ is proportional to $|\mathbf{Q} \cdot e_{\mathbf{q}sd}|^2$, in which the eigenvector of the phonon mode with angular momentum is complex, containing phase information. Such information is lost in the calculation. Therefore, the eigenvectors of the similar norm lead to similar LA and TA intensities at K and K' points indifferent of the scattering geometry.

Because this IXS anomaly depends on the scattering geometry, it is likely that the phonon angular momentum is involved in scattering the photons. In the in-plane scattering geometry, the eigenvectors of LA and TA phonons are parallel to the electric field vectors

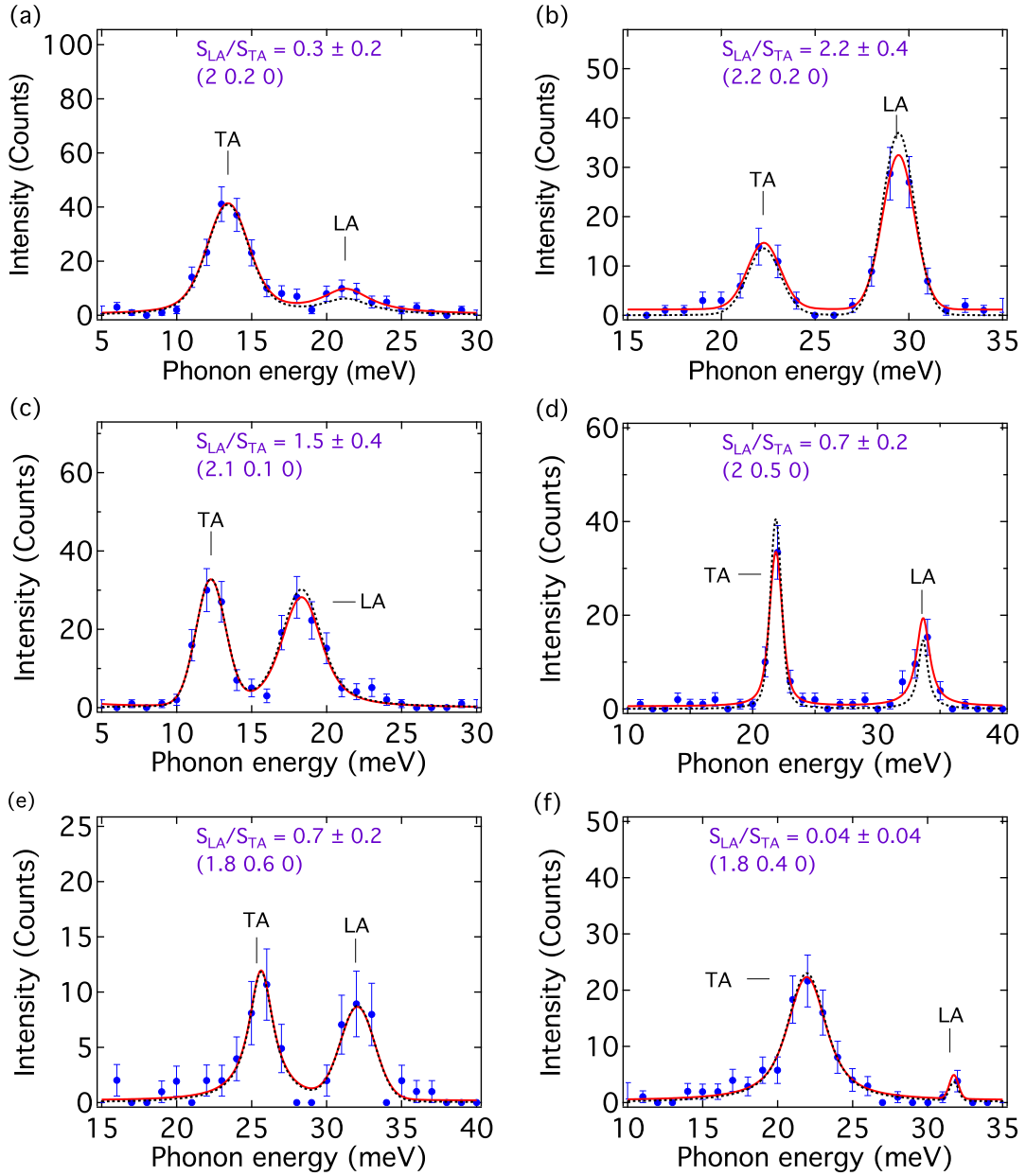


Figure 3.6: The simulation based on equation (3.8) agrees well with the measurement at \mathbf{Q} points away from K and K' points. (a)-(f) IXS spectra with linearly polarized X-ray at $(2\ 0.2\ 0)$, $(2.2\ 0.2\ 0)$, $(2.1\ 0.1\ 0)$, $(2\ 0.5\ 0)$, $(1.8\ 0.6\ 0)$ and $(1.8\ 0.4\ 0)$ in the reciprocal space, respectively. Solid red lines are the Voigt fittings of IXS spectra and dotted black lines represent the spectra simulated from the scattering function. Error bars are from the counting statistics.

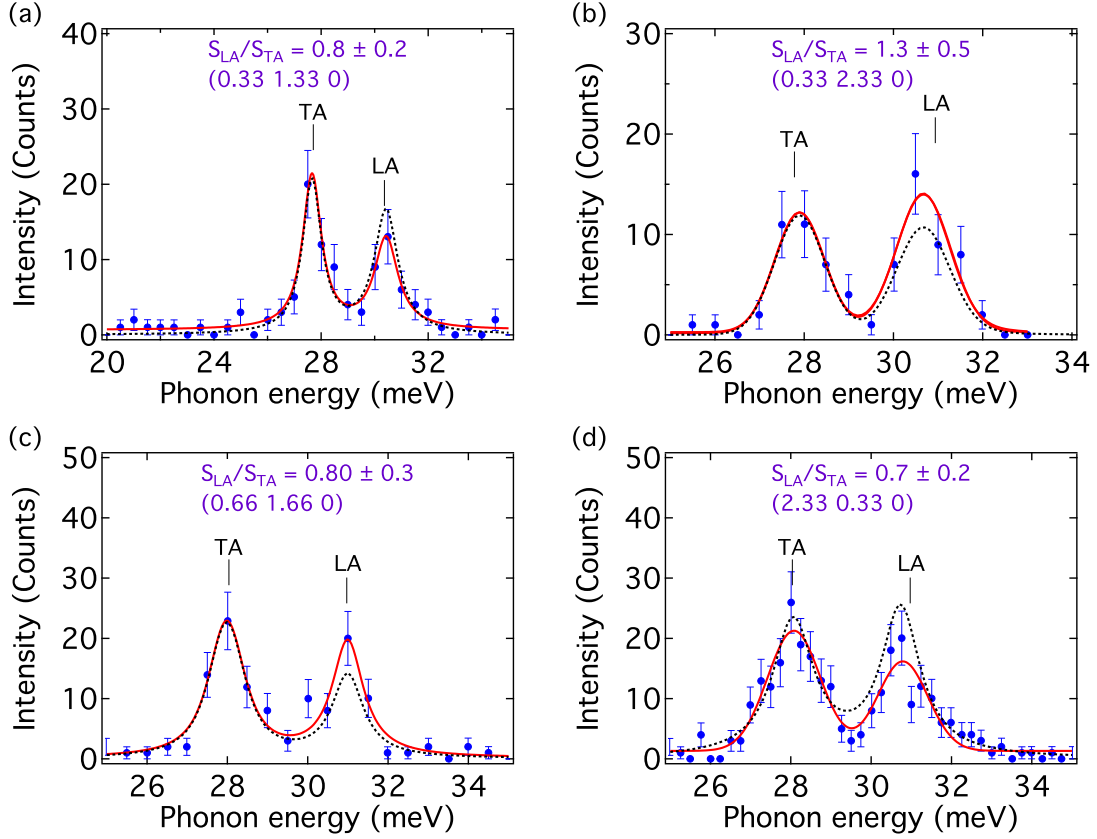


Figure 3.7: The simulation based on equation (3.8) agrees well with the measurement at K and K' points in the in-plane scattering geometry. (a)-(d) IXS spectra with linearly polarized X-ray at (0.33 1.33 0), (0.33 2.33 0), (0.66 1.66 0), and (2.33 0.33 0) in the reciprocal space, respectively. Solid red lines are the Voigt fittings of IXS spectra and dotted black lines represent the spectra simulated from the scattering function. Error bars are from the counting statistics

of incident photons. In this geometry, the phonon angular momentum l_c is perpendicular to the electric field vector of the photon, as shown in Figure 3.1 (c). This geometry may forbid the direct angular momentum transfer between phonons and photons. In the out-of-plane scattering geometry, the two directions are not perpendicular, as shown in Figure 3.1 (d), and angular momentum transfer between phonons and photons may be allowed. The

result hints that the IXS anomaly could arise from the chiral phonon and polarization of phonon/X-ray may play an essential role in the scattering process.

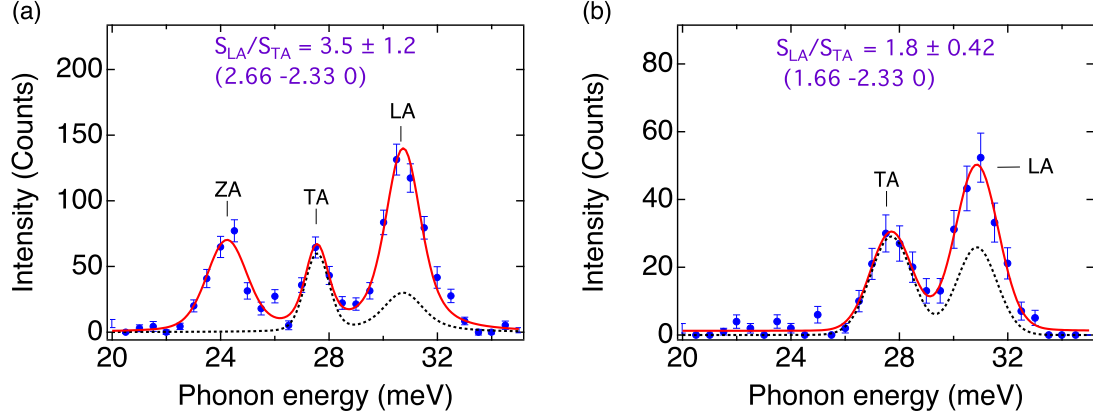


Figure 3.8: The simulation based on equation (3.8) disagrees with the measurement at K and K' points in the out-of-plane scattering geometry. (a)-(b) IXS spectra at K' points (2.66 -2.33 0) and (1.66 -2.33 0); ZA is an out-of-plane acoustic phonon mode; its appearance is explained by multiple scattering. Solid red lines are the Voigt fittings of IXS spectra and dotted black lines represent the spectra simulated from the scattering function. Error bars are from the counting statistics.

It is also reported that the phonon angular momentum along c-axis is distributed on the entire paths K – H and K' – H', [24] only K and K' are used to satisfy the requirements on in-plane and out-of-plane scattering geometries. During phonon creation or annihilation process, phonons at other points along K – H and K' – H' are not involved when conducting measurements at K and K', their angular momentum would not affect the scattering results at K and K' either.

Based on the suggestions from the observation by using linearly polarized X-ray (Figures 3.6 - 3.8), we generated nonlinearly polarized X-ray to measure the two chiral modes at K' (2.66 -2.33 0) in the out-of-plane scattering geometry, with $P_C = -0.99, -0.76, 0, 0.76$ and 0.99 (P_C is the degree of X-ray circular polarization), as shown in Figure 3.9 (a).

There are two main observations: $|P_C|$ could change the scattering intensities of TA and LA modes oppositely, as shown in Figure 3.9 (b) and (c); scattering intensities of LA and TA modes (S_{LA} and S_{TA}) show a symmetric behavior between negative and positive X-ray polarizations. ZA is a linearly polarized mode from multiple scattering process, showing different dependence on X-ray polarization when compared with that of circularly polarized modes. The effect of X-ray polarization suggests that polarizations of phonon and photon play essential roles in the scattering process. The angular momentum exchange between phonons and photons is different for LA and TA modes. The anomalous scattering intensity by using linearly polarized X-ray (Figure 3.8) could be attributed to phonon chirality.

The symmetric behavior of S_{LA} and S_{TA} between opposite X-ray polarizations may be attributed to the twinning structure of WC crystal. [130] Twinning by merohedry in WC makes the crystal consisting of layers stacking in opposite orientations. At any given \mathbf{Q} point, chiral phonons are polarized oppositely in adjacent oppositely oriented layers. Together, the contribution from phonons of both chirality lead to the symmetric dependence on X-ray polarizations.

Linearly and nonlinearly polarized X-ray beam may carry angular momentum as spin angular momentum (SAM) and orbital angular momentum (OAM), it may be speculated that there are exchanges of SAM and/or OAM between phonons and photons. In IXS process, left- and right-hand polarized components of X-ray may be scattered differently by oppositely polarized TA and LA phonons, leading to their intensity difference. In addition, such interaction may be attributed to the current-current correlation function from

the atomic motion of related phonons. We tested and excluded several models based on the current-current correlation function.

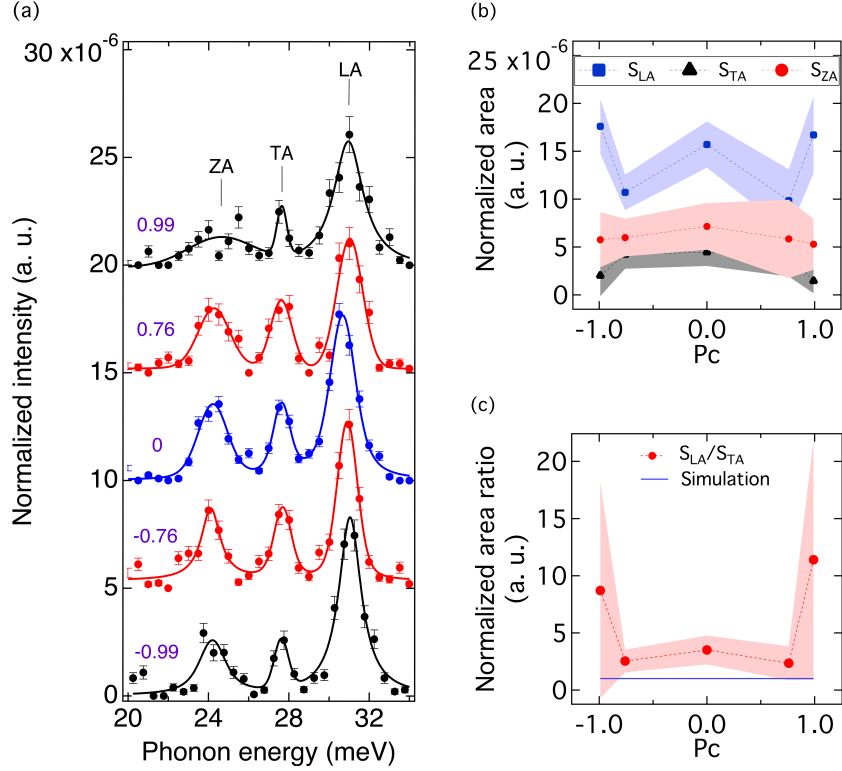


Figure 3.9: X-ray polarization could affect the scattering intensities of circularly polarized phonons. (a) Polarization dependent IXS spectra at K' (2.66 -2.33 0) point. The spectrum at each polarization is integrated from 3-4 scans. The measured intensity is normalized by the flux of incident X-ray after XPR. All the peaks are fitted by Voigt functions. The purple numbers represent the value of P_C . (b) Polarization dependent intensity change of TA and LA modes; (c) Intensity relation of TA and LA modes; Blues line represents the simulated result from existing theory. P_C is the degree of X-ray circular polarization. Shading areas in (b)-(c) are the error sections.

It is the first time that X-ray phase retarder (XPR) is used for IXS on phonon measurements, especially for the experiment on chiral phonons. Based on the results from linearly and nonlinearly polarized X-ray, some major questions remain unanswered. The scattering function, equation (3.8), needs to be revised to include the phonon chirality and

X-ray polarization to address the anomalous IXS. The transfer of angular momentum between lattice and photons, if possible, should be considered. The answers to these questions will enable the IXS as a tool for quantifying chiral phonons and their interactions with other phonons and other degrees of freedom in the materials, such as spin wave, for applications in valleytronics and quantum devices.

3.1.4 Conclusion

In summary, the acoustic phonons of WC along high symmetry directions have been measured by IXS and acoustic phonon DOS has been measured by INS. DFT calculations are compared these measurements with good agreement. The phonon angular momentum calculation shows that phonons are fully circularly polarized at zone boundary (K and K'). While the atomistic simulation works well for most LA and TA phonons elsewhere, it fails dramatically for chiral phonons in the out-of-plane geometry. The X-ray polarization was controlled accurately and affected the scattering process of chiral phonons obviously. The observed IXS anomaly from chiral phonons suggests that the revision of scattering function for phonons is needed. This work lays a foundation of future use of IXS as a tool for investigations of chiral phonons and the effects of phonon chirality in phonon-phonon interactions and phonon-spin interactions for applications in novel phononic quantum devices.

Chapter 4

Temperature- and Pressure- Dependent Phonon Measurements

4.1 Temperature- and pressure-dependent phonon measurements on layered WSe_2

Understanding the microscopic lattice dynamics is essential for regulating the thermal properties in two-dimensional layered materials. In transition metal dichalcogenides, the layered structures result in different but closely related phonon dispersions between monolayer and bulk. Here, by combining inelastic X-ray scattering and first-principles calculations, the lattice dynamics of tungsten diselenide (WSe_2) was investigated comprehensively, and a monolayer-like lattice dynamics in the bulk WSe_2 was revealed. We performed the first measurements of the temperature-dependent phonon dispersions and obtained the mode Grüneisen parameters of bulk WSe_2 , which are found to be in better agreement with

the calculations on the monolayer system than those of the bulk. This observation indicates that lattice dynamics in bulk WSe₂ hold the characterization of monolayers. We also performed the high-pressure IXS measurements on acoustic phonon in bulk WSe₂ and observed the significant pressure-induced phonon stiffening. The pressure-dependent lattice dynamics are very useful to study the strain effects on the van der Waals interactions and anisotropic thermal conductivity in layered materials.

4.1.1 Introduction

Transition metal dichalcogenides (TMDs) have attracted intensive attentions and emerged as promising candidates for advanced applications including electronics, [115, 46] optoelectronics, [145, 60] spintronics, [169] and thermoelectrics. [84, 79] Recently, tungsten diselenide (WSe₂), one valuable member of TMDs, has been extensively studied for the component of field-effect transistors [31] and light-emitting diodes. [119] All the versatile WSe₂-based devices require optimized thermal properties of WSe₂ to enhance their functionality and stability and a comprehensive understanding of the thermal transport in WSe₂ is needed. In many TMDs, phonons are the main heat carriers and play essential roles in their thermal transport performance. So far, the temperature-dependent thermal conductivity of WSe₂ has been reported by experiments and computation. [79, 65, 30, 92] However, a discrepancy between experiment and calculation still exists due to the lack of in-depth understanding of lattice dynamics in the material, especially for the out-of-plane thermal conductivity. Thus, there is a great motivation to investigate the lattice dynamics in WSe₂.

Bulk WSe₂ has a 2H-polytype structure with space group $P63/mmc$ (*No.*194), as shown in Figure 4.1 (a). The unit cell consists of two Se-W-Se layers, which are weakly

bonded by the interlayer van der Waals (vdW) interactions with a lateral offset. Each monolayer comprises three atomic planes, with a plane of W atoms covalently bonded to and sandwiched between two planes of Se atoms. The layered structure results in different but closely related electronic and phonon band structures between monolayer and bulk systems. [79, 29] For phonon band structures, the first-principles phonon calculations and the Raman spectroscopy have reported the phonons of a monolayer, multilayers, and bulk WSe₂. [79, 62, 82] However, owing to the lack of the experimental measurement of full phonon dispersions throughout the entire Brillouin zone (BZ), the microscopic mechanism of thermal transport of WSe₂ remains unclear, and further work is needed.

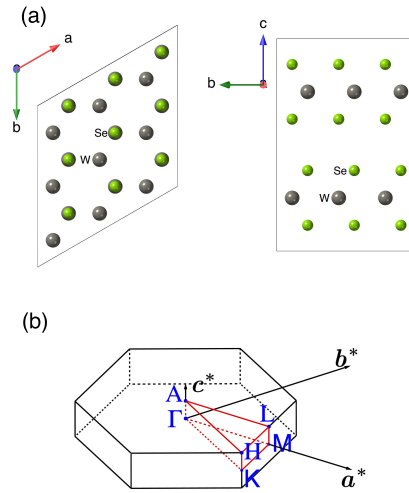


Figure 4.1: (a) Top view and side view of atomic structure of 2H-WSe₂; (b) First Brillouin zone in the reciprocal space.

Inelastic X-ray scattering (IXS) technique is a powerful tool to measure phonon dispersions in a wide range of materials especially including small single crystals of two-

dimensional (2D) layered materials. [148] Generally, the scattering is extremely weak from monolayer samples. Instead, the bulk samples were successfully used to obtain the phonon dispersions by IXS to study various thermal properties, such as phonon anharmonicity, anisotropic thermal transport, and thermal conductivity, in layered-2D materials. [148, 138, 149, 104] This inspired us to conduct comprehensive temperature- and pressure- dependent IXS measurements on bulk WSe₂ and quantify the phonon dispersions in this material.

In this work, we found that the phonon dispersion and mode Grüneisen parameters from first-principles calculation on monolayer WSe₂ agree with the temperature-dependent IXS measurements of the bulk samples reported in this work. The fitted power law of the measured out-of-plane vibrational acoustic (ZA) branch along Γ -M and Γ -K (directions in reciprocal space shown in Figure 4.1 (b)) significantly deviate from the corresponding calculated values in bulk material but close to the calculated values in monolayer, showing the monolayer-like vibrational behavior of ZA in the bulk crystals. In addition, significant softening of ZA phonons around the BZ center was observed with decreasing temperature. The acoustic phonons along Γ -A also show a similar temperature dependence. The reported results in this work highlight the importance of first-principles calculation on monolayer for investigating the phonon dynamics in bulk transition metal dichalcogenides. We also observed the pressure induced stiffening of in-plane acoustic phonons in bulk WSe₂. Our work also provides the theoretical and experimental reference for studying the thermodynamics and thermal transport properties in related two-dimensional layered materials.

4.1.2 Materials and Methods

High quality WSe₂ single crystals (Figure 4.2, typical size of 300×400 m²) were purchased commercially. The sample was attached to a copper post by epoxy and the copper post was mounted on a 4-axis rotation and 3-dimension translation stage for alignment. Temperature dependent phonon dispersion measurements were performed by the HERIX

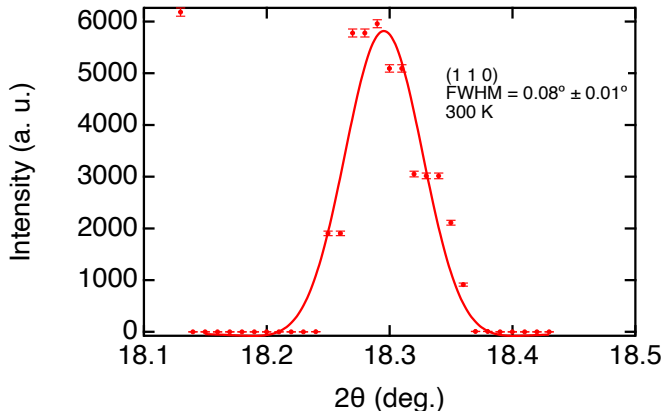


Figure 4.2: The rocking curve of WSe₂ single crystal measured by HERIX shows the high crystalline quality. The X-ray wavelength is 0.5226 Å. The narrow full width at half maximum (FWHM) indicates high crystalline quality of the sample.

spectrometer at 30-ID of the Advanced Photon Source, Argonne National Laboratory. A photon energy of 23.7 keV (wavelength at 0.5226 Å) is used. The instrument has an energy resolution of 1.5 meV (full width at half maximum, FWHM) and a momentum resolution of 0.65 nm⁻¹ in the configuration. [120] The X-ray energy loss spectrum was collected by scanning the incident X-ray (from a high efficiency six-reflection cryogenically stabilized meV-monochromator) energy at 0.5 meV steps. [135] CdTe Pilatus3 area detectors were used for data collection. [121] A closed-cycle cryostat sample environment was used. Phonon dispersion measurements were conducted at 300, 150, and 25 K along some high symmetry

directions in the reciprocal space. The raw IXS spectra were fitted by Gaussian function to identify the phonon peak location and FWHM (full width at half maximum). For each phonon peak, it can be fitted by the Gaussian function written as:

$$f(x) = y_0 + Ae^{(-\frac{x-x_0}{width})^2}, \quad (4.1)$$

where y_0 is the baseline of the peak, A is the height of the peak, x_0 is the position of the center of the peak, $FWHM = 2\sqrt{\ln 2} \times width$. The fitting result is used to obtain the phonon linewidth.

First-principles calculations on bulk and monolayer WSe₂ were performed with the density-functional theory (DFT) implemented in Vienna Ab initio simulation package (VASP). [76] We used the exchange correlation function with the Local Density Approximation (LDA) and the projector-augmented-wave (PAW) potentials. The relaxed lattice constants ($a = b = 3.250 \text{ \AA}$, $c = 12.83 \text{ \AA}$) were used for the calculation on bulk WSe₂. In the monolayer system, the relaxed lattice constants ($a = b = 3.247 \text{ \AA}$, $c = 23.84 \text{ \AA}$) were used, including 20 \AA vacant space between each layer to avoid interlayer interactions. The kinetic energy cutoff was 900 eV, the threshold for the total energy convergence was 10^{-8} eV. The vdW interaction was taken into consideration by using vdW-DF-cx functionals. [15] Second order force constants were calculated by the finite displacement method in supercells ($4 \times 4 \times 1$). Gamma centered q-point meshes of $3 \times 3 \times 3$ was used. The phonon dispersion in harmonic approximation was calculated using Phonopy. [137] Grüneisen parameter provides quantitative connections between phonon frequency and volume change. Phonon dispersion relations at three volumes (original, 1.2% larger, and 1.2% smaller) were calculated and

mode Grüneisen parameters $\gamma(\mathbf{q}, s)$ based on quasi-harmonic approximation (QHA) were obtained by [137]:

$$\gamma(\mathbf{q}s) \cong -\frac{V}{(2[\omega(\mathbf{q}s)]^2)} \left\langle e(\mathbf{q}s) \left| \frac{\Delta \mathbf{D}(\mathbf{q})}{\Delta V} \right| e(\mathbf{q}s) \right\rangle, \quad (4.2)$$

where \mathbf{q} is the phonon wave vector, s is the band index, $\omega(\mathbf{q}s)$ is the phonon frequency, $e(\mathbf{q}s)$ is the phonon eigenvector, $\mathbf{D}(\mathbf{q})$ is the dynamical matrix, V is the original unit cell volume, and δV is the volume variance. In bulk system, the volume change was made by modifying the lattice constants based on the anisotropic thermal expansion coefficients of lattice constants a and c . [106] To evaluate the Grüneisen parameter for monolayer, the volume change was made by modifying in-plane lattice constants while keeping the large vacuum space between layers. At each volume, the atom coordinates and cell shape were relaxed. When in-plane lattice constants increase (decrease), the relaxed layer thickness (defined as the vertical distance between the two Se planes in the unit cell) decreases (increases). The unit cell volume change of monolayer was calculated using the in-plane lattice constants and layer thickness. Implementing the phonon frequency change and volume change with QHA, we obtained the mode Grüneisen parameters in monolayer, which were consistent with the reported results. [61]

To evaluate the Grüneisen parameter from temperature-dependent IXS measurements, experimental thermal expansion [106] was used to obtain the temperature-induced volume change. The isobaric mode Grüneisen parameter $\gamma(\mathbf{q}s)$ were calculated based on measured temperature-dependent phonon frequency:

$$\gamma_P(\mathbf{q}s) = - \left(\frac{d \ln \omega_{\mathbf{q}s}}{d \ln V} \right)_P = - \frac{1}{\alpha \omega_{\mathbf{q}s}} \left(\frac{d \omega_{\mathbf{q}s}}{dT} \right)_P, \quad (4.3)$$

where α is the volumetric thermal expansion coefficient. [106]

4.1.3 Results

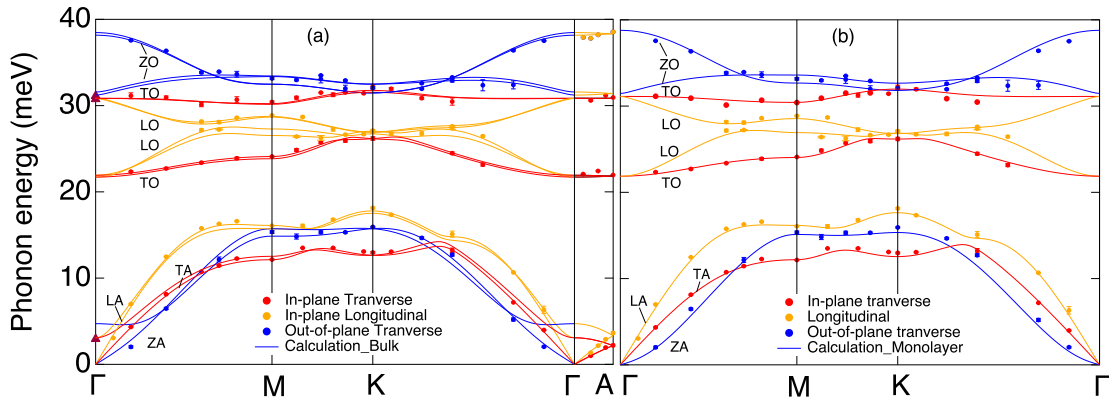


Figure 4.3: Phonon dispersion of bulk and monolayer WSe_2 along high symmetry directions at 300 K. (a) Comparison between calculated and experimental dispersion of bulk WSe_2 ; (b) Comparison between calculated monolayer dispersion and experimental bulk dispersion. Orange lines and dots represent the calculated and measured longitudinal modes, red color represents the in-plane transverse modes, blue color represents the out-of-plane transverse modes, and the dark red triangles are Raman active modes. All IXS spectra are fitted by Gaussian function, error bar represents the fitting error of phonon peak.

Figure 4.3 shows the IXS measured phonon dispersion of bulk WSe_2 along some high symmetry directions in the BZ at 300 K. Bulk 2H- WSe_2 has 6 atoms per unit cell and 18 phonon branches: three acoustic and fifteen optical. Due to the relatively weak interlayer vdW bondings, some phonon branches called Davydov pairs [138] are almost degenerate, as shown in Figure 4.3 (a). Each pair consists of two phonon modes with slightly different frequencies and similar eigenvectors. The eigenvectors of the atoms in one of the layers

have a phase shift of π between the two modes [138]. We observed three acoustic branches and six optical branches in IXS measurement. Figure 4.4 shows the scattering intensity simulation in the measured BZ by using first-principles phonon calculation and the two modes in each pair have a noticeable intensity difference. Thus, only one in each pair will

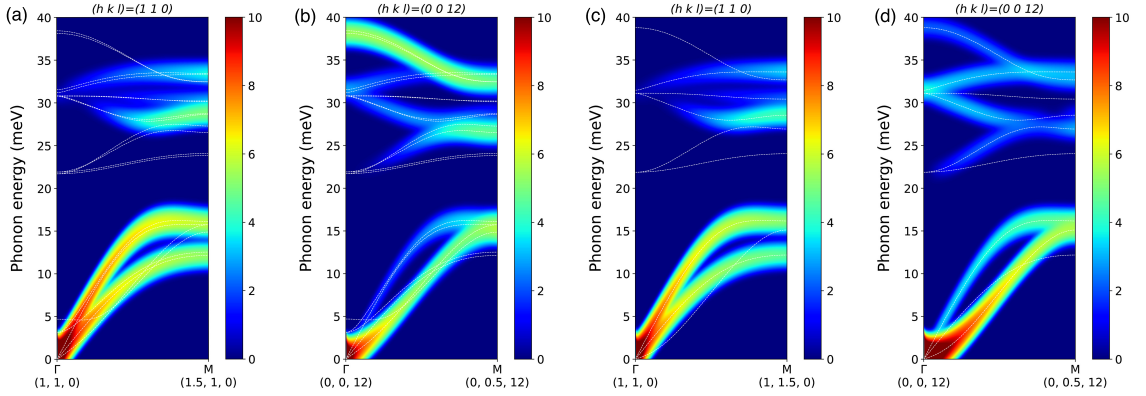


Figure 4.4: Intensity simulation of bulk and monolayer WSe_2 . (a) and (b) represent the dynamical structure factor of phonon branches along Γ –M in Brillouin zone (1 1 0) and (0 0 12) in bulk WSe_2 ; (c) and (d) represent the dynamical structure factor of phonon branches along Γ –M in Brillouin zone (1 1 0) and (0 0 12) in monolayer WSe_2 . The white dashed lines represent the phonon dispersion, the color bar is in log scale. A resolution of 1.5 meV is used in the simulation.

be observed in each Brillouin zone. On the other hand, the calculated phonon dispersion of the monolayer has 9 branches with similar energy to the IXS measurement, as shown in Figure 4.4 (b). Phonon calculation on monolayer used the large vacant space between each layer, which results in much smaller reciprocal lattice constants along a cross-plane direction. Simulation in BZ (0 0 12) of the monolayer is different from that of the bulk WSe_2 (shown in Figure 4.4 (b) and (d)) due to the large difference in their reciprocal lattice

constant c^* . However, simulation in BZ (1 1 0) is similar in monolayer and bulk owing to the similar reciprocal lattice constants a^* and b^* , as shown Figures 4.4-a and 4.4-c.

It can be seen that phonon dispersions calculated from first-principles calculation on bulk and monolayer agree well with the IXS measurement on bulk, including all optical and acoustic branches. In bulk calculation, there is a slight overestimation of the ZA energy near Γ along both Γ -M and Γ -K directions. On the contrary, monolayer calculation has better agreement along these directions. [61, 93] The ZA mode is known as the flexural mode with parabolic dispersion in two-dimensional systems. To better understand this flexural mode, the dispersion relation is fitted by the power-law relation: $\omega = \alpha k^\beta$, where k is the wave vector in reciprocal space, α and β are fit parameters. Table 4.1 shows the fitting parameters of ZA branch along Γ -M ($q < 0.2$) and Γ -K ($q < 0.1$) directions. For ideal parabolic dispersion, β is 2. Our phonon calculation predicts that the parameters are similar along Γ -M and Γ -K, but they differ significantly in the IXS results. The measured β is larger than that in the bulk calculation in both directions. It is also larger than the value in the monolayer along Γ -M. The larger β indicates the ZA branch is closer to a parabolic dispersion, indicating that ZA branch in the bulk WSe₂ retains the characteristic flexural dispersion reported in its 2D system. The flexural mode was also observed by the IXS measurements on bulk MoS₂ and the overestimation of ZA energy in bulk DFT calculation was reported. [138] These results suggest that the used vdW functional likely overestimates the interlayer interactions and underestimates the flexural mode.

Analyzing the temperature dependence of acoustic phonons along Γ -M and Γ -K directions, as shown in Figure 4.5 (a), there are mainly two observations. Firstly, LA and

Table 4.1: β parameter of ZA dispersion within Γ -M ($q < 0.2$) and Γ -K ($q < 0.1$).

	Γ -M ($q < 0.2$)	Γ -K ($q < 0.1$)
Experiment	1.70 ± 0.01	1.34 ± 0.01
DFT-Bulk	1.18 ± 0.01	1.20 ± 0.01
DFT-Monolayer	1.53 ± 0.01	1.51 ± 0.01

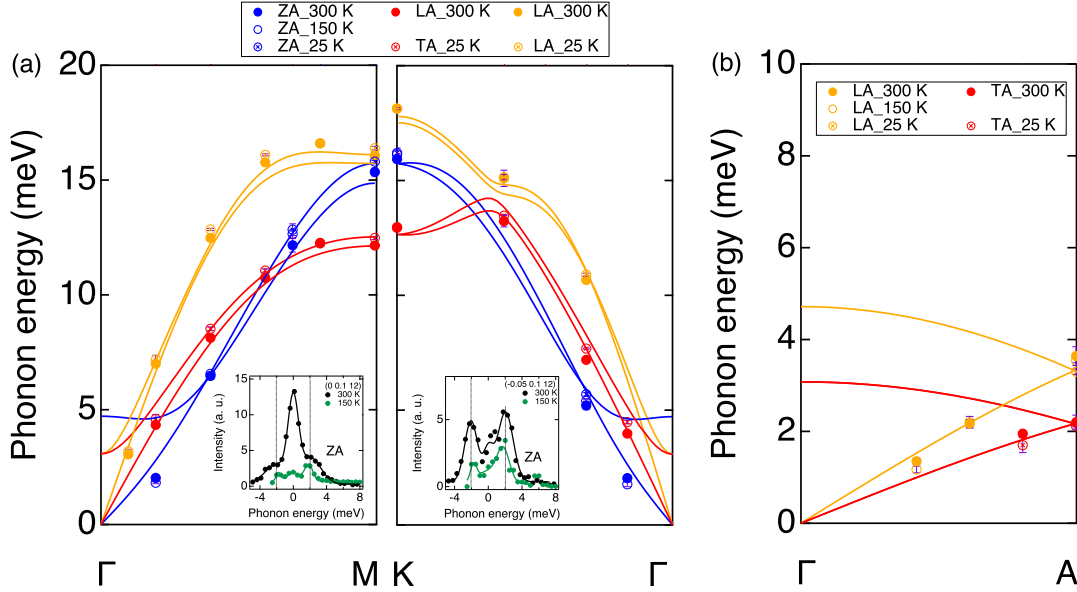


Figure 4.5: Temperature dependent phonon measurement on acoustic phonons (a) Phonon measurement along in-plane high symmetry directions; The insets are the IXS spectra at $(0\ 0.1\ 12)$ and $(-0.05\ 0.1\ 12)$ at 300 K and 150 K respectively. (b) Phonon measurement along out-of-plane direction. The error bar represents the fitting uncertainty. The orange, red and blue colors represent the LA, TA, and ZA modes respectively. The filled, hollow, and crossing markers represent 300, 150, and 25 K.

TA modes stiffen with decreasing temperature. Secondly, ZA mode softens with decreasing temperature near the zone center and stiffens near the zone boundary. Such softening is shown by the IXS spectra at $(-0.05\ 0.1\ 12)$ and $(0\ 0.1\ 12)$ (Figure 4.5). Phonon energy of ZA mode decreases from 2.0 ± 0.1 to 1.8 ± 0.1 meV at $(-0.05\ 0.1\ 12)$ when temper-

ature decreases from 300 to 150 K. With similar temperature dependence, energy of ZA softens from 2.0 ± 0.1 to 1.8 ± 0.04 meV at (0 0.1 12). LA and TA modes along these two directions correspond to the in-plane atomic vibrations and are tightly related to the intralayer interactions of covalent bondings. ZA phonons correspond to the out-of-plane atomic vibrations and are related to the interlayer vdW interactions. The thermal expansion induced by increasing temperature causes longer in-plane covalent bonding length and weaker intralayer interactions, which might result in a smaller vibrational frequency of TA and LA modes. However, the increased in-plane lattices parameters make the stacked layer stiffer to a flexural vibration and may lead to larger vibrational frequency of the flexural mode (just like string effect [44] or membrane effect [105] in 2D system). The results indicate that each stacked layer in bulk material keeps the majority characteristic of acoustic phonons in monolayer WSe₂ and suggest that interlayer vdW interactions do not significantly influence the acoustic and optical phonons. In addition to the phonon energy shift, temperature-dependent linewidth is obtained in Figure 4.7 based on the super-resolution method (Mentioned in Chapter 3). Due to the instrument resolution in energy and momentum, we could not extract the phonon linewidth from all measured \mathbf{Q} point. Therefore, it is difficult to quantify the temperature dependence of acoustic phonons' linewidth. Linewidth of most acoustic phonons at 300 K could be extracted, while most of the phonon linewidths are resolution limited at 150 and 25 K. It suggests that linewidths of the measured acoustic modes broaden with increasing temperature. Broader phonon linewidth indicates larger phonons scattering rates and could lead to the decreasing thermal conductivity from 150 to 300 K. [119, 36]

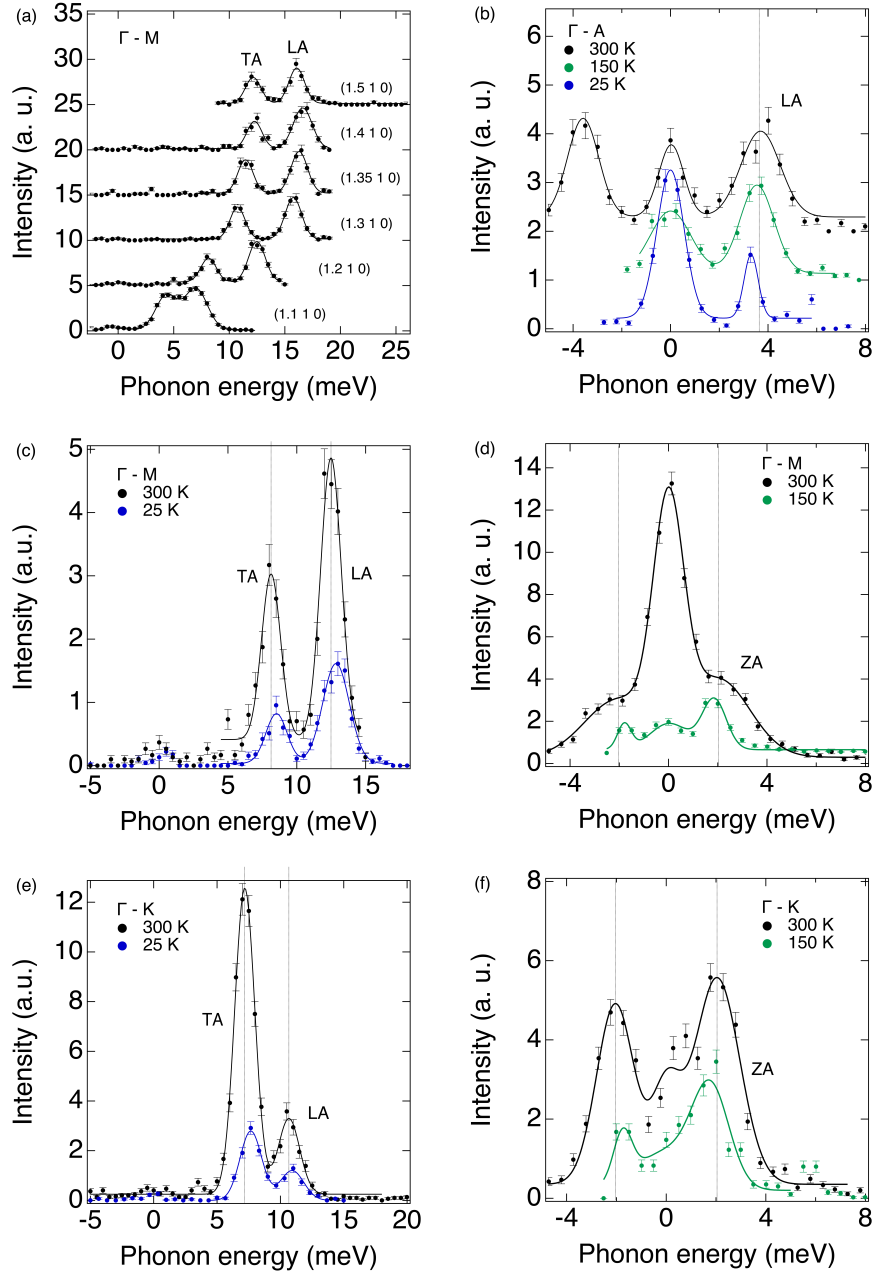


Figure 4.6: IXS spectra with Gaussian fitting. (a) IXS spectra measured along Γ -M direction in BZ (1 1 0) under 300 K; The black points represent raw data, and the red lines represent the Gaussian fitting. (b) IXS spectra measured at (0 0 12.5) along Γ -A direction under 300 K (black), 150 K (green) and 25 K (blue). (c) IXS spectra measured at (1.2 1 0) along Γ -M direction under 300 K (black), and 25 K (blue). (d) IXS spectra measured at (0 0.1 12) along Γ -M direction under 300 K (black), and 150 K (green). (e) IXS spectra measured at (0.9 1.2 0) along Γ -K direction under 300 K (black), and 25 K (blue). (f) IXS spectra measured at (-0.05 0.1 12) along Γ -K direction under 300 K (black), and 150 K (green). The intensity is rescaled to arbitrary unit (a. u.).

Along out-of-plane Γ -A direction in bulk crystals, TA and LA modes soften slightly from 300 to 25 K, as shown in Figure 4.5 (b). As for their extracted phonon linewidth, phonon linewidth of LA mode decreases slightly from 300 to 25 K. The results imply that the acoustic phonons along Γ -A direction have larger group velocity and LA phonons have higher scattering rates at 300 K. It needs to be noted that acoustic phonons along Γ -A direction have smaller energy and larger linewidth than those along Γ -M and Γ -K directions, suggesting the lower phonon group velocity and stronger phonon-phonon scatterings along Γ -A direction. Due to the instrument resolution in energy and momen-

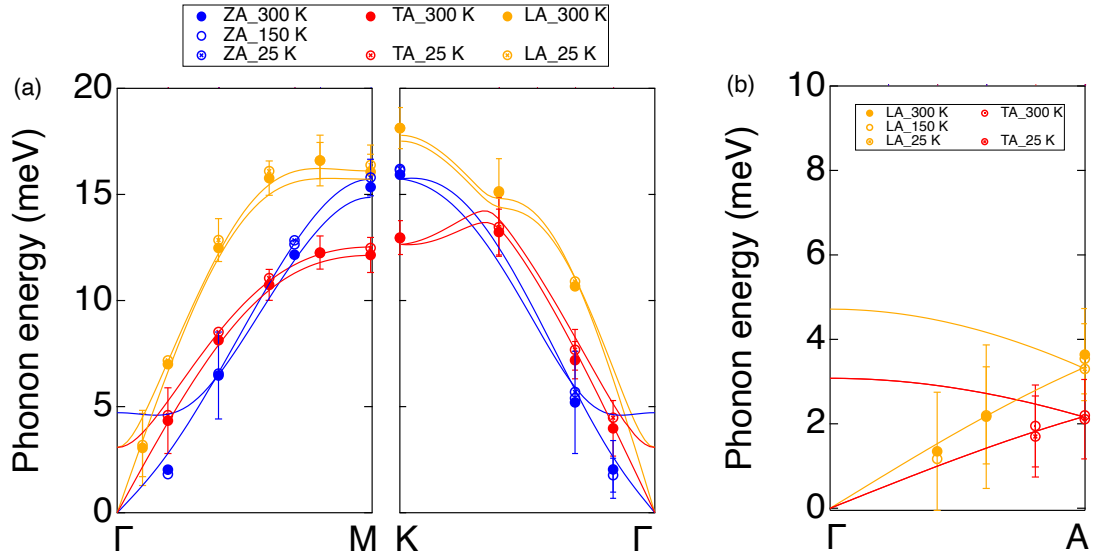


Figure 4.7: Temperature dependent phonon measurement on acoustic phonons (a) Phonon measurement along in-plane high symmetry directions; (b) Phonon measurement along out-of-plane direction. The phonon linewidths are shown as error bars. The points without error bar means the phonon linewidths are resolution limited. The orange, red and blue colors represent the LA, TA, and ZA modes respectively. The filled, hollow, and crossing markers represent 300, 150, and 25 K.

entum, we could not extract the phonon linewidth from all measured \mathbf{Q} point with super-

resolution method. Therefore, it is difficult to quantify the temperature dependence of acoustic phonons' linewidth. Linewidth of most acoustic phonons at 300K could be extracted, while most of the phonon linewidths are resolution limited at 150 and 25 K. It suggests that linewidths of the measured acoustic modes broaden with increasing temperature. Broader phonon linewidth indicates larger phonons scattering rates and could lead to the decreasing thermal conductivity from 150 to 300 K. [119, 36]

Using temperature-dependent IXS results on acoustic phonons along Γ -M and Γ -K directions, experimental isobaric mode Grüneisen parameters were obtained by equation (4.3). based on QHA (estimation of phonon frequency shift associated with the volume change), mode Grüneisen parameters of acoustic branches were calculated by DFT. Figure 4.8 shows the IXS measured isobaric mode Grüneisen parameters of bulk WSe₂ and DFT calculated the mode Grüneisen parameters of bulk (Figure 4.8 (a)) and monolayer WSe₂ (Figure 4.8 (b)). The better agreement found in monolayer calculation also indicates that acoustic phonons in the bulk system keep their 2D nature in monolayer. In Figure 4.8, QHA greatly underestimates the γ of TA and LA modes, especially near Γ point, in bulk calculation. The values of γ in QHA are about $\frac{1}{3}$ of our experimental values. As for ZA modes, QHA shows the positive γ along in-plane directions and predicts the softening behavior with thermal expansion. This prediction is contrary to our observation that ZA mode stiffens from 150 to 300 K. Such discrepancy reveals that QHA fails in predicting the temperature-induced frequency change of acoustic phonons in bulk WSe₂.

In monolayer calculation, as shown in Figure 4.8 (b), QHA has a decent agreement with the IXS measured γ values of the bulk system. The calculation in our work is

slightly different from the reported results in Ref. [61], showing smaller γ values throughout the in-plane directions. QHA works well in using thermal expansion to describe the temperature dependence of LA phonons along Γ –M and Γ –K directions, while it still has some discrepancy at the zone boundary. As for TA phonons, QHA underestimates their γ significantly along Γ –K and shows better agreement along Γ –M. For the featured flexural mode, QHA predicts a divergent γ near Γ point. In bulk IXS measurement, the negative γ of ZA modes at $(-0.05 \ 0.1 \ 12)$ and $(0 \ 0.1 \ 12)$ are $-15.4 \text{ pm}^{-1.7}$ and $-15.4 \text{ pm}^{-1.4}$ respectively, which quantitatively agree with the calculated values in monolayer. This result suggests that QHA in monolayer provides better prediction in the temperature dependence of flexural modes in bulk WSe₂.

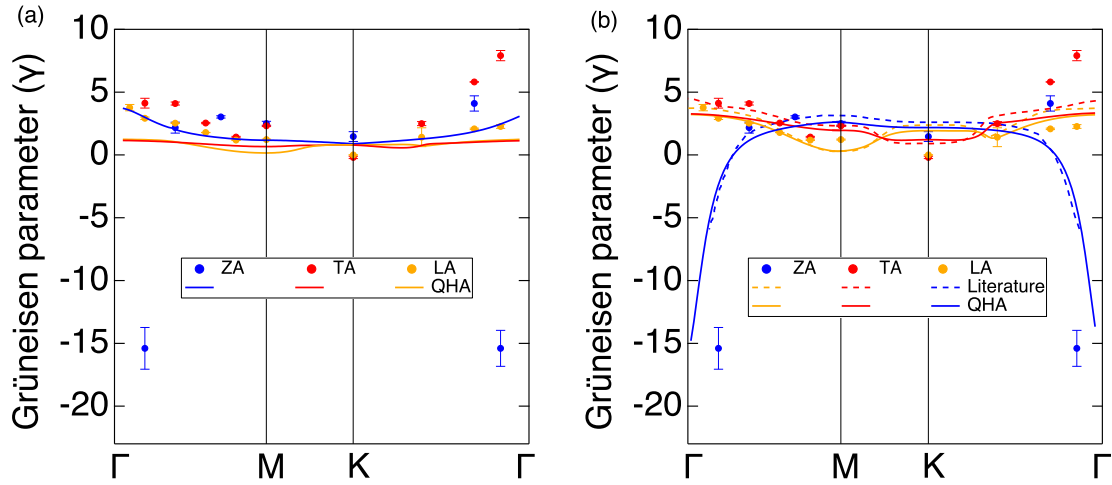


Figure 4.8: (a) Acoustic phonon isobaric modes Grüneisen parameters compared with bulk calculation; (b) Acoustic phonon isobaric modes Grüneisen parameters compared with monolayer calculation. Blue lines and points represent the Grüneisen parameters of ZA mode obtained from calculation and experiment, respectively. Orange and red represent LA and TA, respectively. Solid lines represent the calculation based on QHA, the dashed lines represent the γ dispersion relation from literature. [61]

As for the pressure-dependent results, the Figure 4.9 (a) and (b) shows that the increasing pressure stiffens the in-plane acoustic phonons. The isothermal mode Grüneisen parameters can be calculated [21] and are shown in Figure 4.9 (c) and (d). The results indicate that calculation based on QHA in bulk system is close to the experimental isothermal Grüneisen parameters and has good prediction on the pressure dependence of in-plane acoustic phonons. On the other hand, the discrepancy between isothermal and isobaric Grüneisen parameters reveals the giant phonon anharmonicity in WSe₂.

4.1.4 Discussion

The temperature dependent IXS on bulk WSe₂ and first-principles calculations suggest monolayer-like lattice dynamics in bulk system. The flexural phonons were observed in the bulk WSe₂ and found to have the similar temperature dependence to those in monolayer. The temperature dependence of flexural phonons has only been reported by first-principles calculation on graphene. [143] This is the first observation of the softening of flexural phonons with decreasing temperature. Such observation is of great significance because flexural phonons play essential roles in the thermal conductivity and electron mobility. Flexural phonons have dominant contributions to the thermal conductivity in graphene and graphite. [94] In bulk and monolayer WSe₂, acoustic phonons contribute dominantly to the in-plane thermal conductivity. [36, 103]. The flexural phonons have a similar contribution to the total thermal conductivity when compared with other acoustic branches. [36, 159] However, the reported thermal conductivity calculation did not consider the flexural dispersion of ZA mode. Our results help validate the phonon calculation and improve the

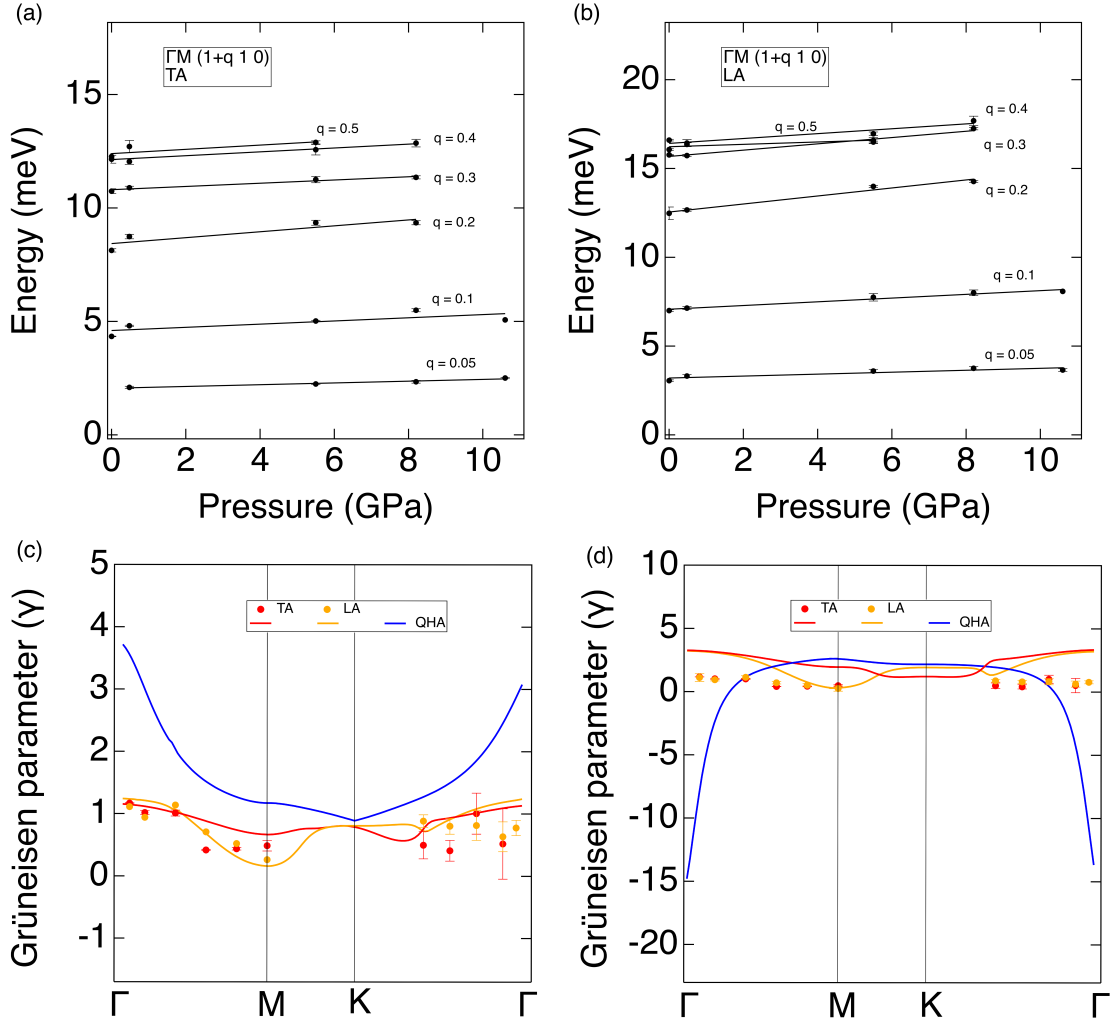


Figure 4.9: (a) Pressure dependence of TA modes along Γ -M; (b) Pressure dependence of LA modes along Γ -M. (c) Acoustic phonon isothermal modes Grüneisen parameters compared with bulk calculation; (d) Acoustic phonon isothermal modes Grüneisen parameters compared with monolayer calculation. Orange, red and blue lines represent the Grüneisen parameters of LA, TA and ZA modes obtained from calculation based on QHA, respectively. Orange and red points represent the experimental isothermal Grüneisen parameters.

accuracy in studying the role of flexural phonons in thermal transport in TMDs. On the other hand, electron mobility is dramatically affected by the scattering by flexural phonons in 2D hexagonal semiconducting TMDs. [67] The measured mobility of atomically thin

MoS₂ is almost two orders of magnitude lower than that of its bulk counterpart. [115, 152] The obvious discrepancy may be related to the much weaker scattering by flexural phonons in bulk system. What's more, the QHA predicts that flexural mode shifts significantly with temperature, which could promote the investigation of its pressure dependence and quantifying the interlayer vdW interactions.

In addition to the ZA mode, LA and TA modes also contribute significantly to the total in-plane thermal conductivity. QHA on TA mode apparently underestimates the temperature-induced energy shift along Γ -K. This result reveals that QHA can not sufficiently account for the temperature dependence of TA modes, which may have large anharmonicity. The anharmonic renormalization of phonon dispersion is very important in calculating the in-plane thermal conductivity contribution from TA phonons. Along the cross-plane direction, our results suggest the lower group velocity and stronger phonon-phonon scatterings in acoustic phonons. This is related to the giant anisotropic thermal conductivity between in-plane and cross-plane directions in TMDs. [65, 30] It is reported that cross-plane thermal conductivity of WSe₂ is ultralow and varies with the sample thickness. [30, 109] Our temperature-dependent phonons along Γ -A could provide valuable validation for thermal calculation and help to explain the giant anisotropic thermal transport in WSe₂ and other TMDs. [69, 27]

The monolayer-like lattice dynamics in bulk WSe₂ further indicates that vdW interactions have little effect on the acoustic phonons in layered materials. The flexural phonons hint that interlayer vdW interactions are much weaker than expected in terms of lattice dynamics. We hope the result can be useful in improving the accuracy of vdW

functionals for DFT calculations on layered materials. The measured acoustic phonons in the bulk system could also be used as reference to study the lattice dynamics in monolayer system. The first-principles calculation predicts that temperature dependence of acoustic phonons in monolayer WSe₂ is weak and neglectable, especially for phonons near the zone center. [103] Our observation is distinct from the prediction and provides significant insights into the temperature-dependent lattice dynamics of monolayer TMDs.

4.1.5 Conclusion

We have conducted the temperature-dependent IXS experiment on bulk WSe₂ to measure the phonon dispersion along some high symmetry directions in BZ. We observed the flexural dispersive ZA branch along Γ -M and Γ -K directions in the bulk system. In addition, we observed the significant ZA mode softening when decreasing temperature from 300 K to 150 K. We also found that the acoustic phonons along Γ -A soften moderately with decreasing temperature. The first-principles calculation on monolayer WSe₂ has better agreement with our IXS measured phonon dispersion and mode Grüneisen parameters. The results reveal the microscopic mechanism of phonon dynamics in WSe₂ and suggest a monolayer-like lattice dynamics in bulk WSe₂. The additional pressure-dependent results are very useful to study the strain effects on the van der Waals interactions. This work provides the theoretical and experimental reference for studying thermodynamics and anisotropic thermal conductivity in other related two-dimensional layered materials.

4.2 Phonon anharmonicity in para-terphenyl

INS has been performed on para-terphenyl at temperatures from 10 to 200 K and under pressures from the ambient pressure to 1.51 kbar. The temperature dependence of phonons, especially low-frequency librational bands, indicates strong anharmonic phonon dynamics. The pressure- and temperature-dependence of the phonon modes suggest a lack of phase transition in the region of 0 - 1.51 kbar and 10 - 30 K. Additionally, the overall lattice dynamics remains similar up to 200 K under the ambient pressure. The results suggest that the boundary between the ordered triclinic phase and the third solid phase, reported at lower temperatures and higher pressures, is out of the pressure and temperature range of this study.

4.2.1 Introduction

Para-terphenyl (p-terphenyl) has attracted much attention due to its unique electro-optical properties. These properties have allowed p-terphenyl to be utilized in many applications including host crystals for single molecule studies, [110, 80] a wavelength shifter, [3] and a radiation detector. [6] Moerner and Lounis have reported the application of p-terphenyl as a host crystal in the generation of triggered single photons at room temperature. [96] Oxborrow et al. have reported the experimental demonstration of a solid-state maser operating in pulsed mode at room temperature. The gain medium of the maser was pentacene crystal doped in a p-terphenyl matrix. [111] Super-conductivity with T_c in the range of 43-123 K has been reported for potassium doped p-terphenyl, [160, 146, 147] and superconducting pairing with a 12 meV gap opening at 60 K was reported. [89] The unknown superconduc-

tivity mechanism is thought to arise from bipolarons or Cooper pair formation. In either case, phonons (electron-lattice interaction) are critical to understanding this phenomenon and deserve investigation.

Linear polyphenyls such as p-terphenyl have unique temperature- and pressure-induced solid-solid phase transitions due to the strong coupling between molecular conformational changes and intermolecular rearrangements. [124, 123] At high temperature, these molecules are flat on average but have unusual large thermal intramolecular rotational motion about their long axis that involves rotation of central phenyl rings through the mean molecular plane. Solid-solid phase transitions are associated with the locking of this rotational motion at low temperature. At high pressure, however, the central phenyl rings become locked in a static planar molecular configuration.

The high temperature phase of p-terphenyl is monoclinic, with the space group $P21/a$ with $a = 8.106 \text{ \AA}$, $b = 5.613 \text{ \AA}$, $c = 13.613 \text{ \AA}$, $\beta = 91^\circ$, and $Z = 2$ (two molecules per unit cell). [118] At temperatures below 193 K, every other molecule becomes constrained to one side of the double well potential for rotation of the central phenyl ring. This leads to an ordered structure, which can be described by a pseudomonoclinic supercell with lattice parameters $a' = 2a$, $b' = 2b$, $c' = c$, $\beta' = \beta$, with 4 times the volume of the high temperature monoclinic cell (e.g., $V' = a'b'c'\sin\beta'$) and 8 molecules per supercell ($Z = 8$). [14] If the diffraction pattern is indexed with respect to the original high temperature monoclinic cell, then the extra peaks appear at $(\frac{1}{2} \frac{1}{2} 0)$, [22] although a triclinic cell of half this volume (with $Z = 4$) is sufficient for generating the crystal. [117] Temperature dependent x-ray diffraction has been utilized to characterize the phase transition of p-terphenyl from the

room temperature disordered monoclinic phase ($P21/a$) to an ordered triclinic phase (C-1) below 193 K. [117] Recently, diffuse neutron scattering has been used to model the connection between intermolecular interactions and short-range order in p-terphenyl. [51] The pair distribution function (PDF) can be extracted from neutron powder diffraction data to yield information about the molecular structure of a compound [114]. This method was applied to p-terphenyl to successfully determine the short-range order. The phase diagram of p-terphenyl and deuterated p-terphenyl have been determined by a collection of Raman, neutron, and optical studies, the results of which are summarized in Figure 21. It needs to be noted that Figure 4.10 does not include any molecular nor pair distribution function data.

Inelastic neutron scattering measurements [139] have revealed evidence for a third solid phase of p-terphenyl (phase III) at low-temperature and high-pressure (with a triple point at $T \sim 71$ K, $P \sim 3.5$ kbar). This phase is characterized by the appearance of a $(\frac{1}{2}, \frac{1}{2}, \frac{1}{2})$ reflection (referred to the high temperature monoclinic unit cell) described by a large monoclinic supercell with $a'' = 2a$, $b'' = 2b$, $c'' = 2c$, with $Z = 16$. [139] However, the smallest repeating unit for this new phase III crystal lattice is still triclinic with $Z = 4$, but with a different (uncharacterized) arrangement of the molecules compared to the low-pressure low-temperature triclinic. To our knowledge, the only other published neutron spectrum was taken at 130 K. [116] Phase transition from the ordered triclinic phase to the third solid phase in the low-temperature high-pressure region has not been investigated. In the current work, low-temperature high-pressure inelastic neutron scattering is performed to characterize the lattice dynamics and its relation to potential phase transformations.

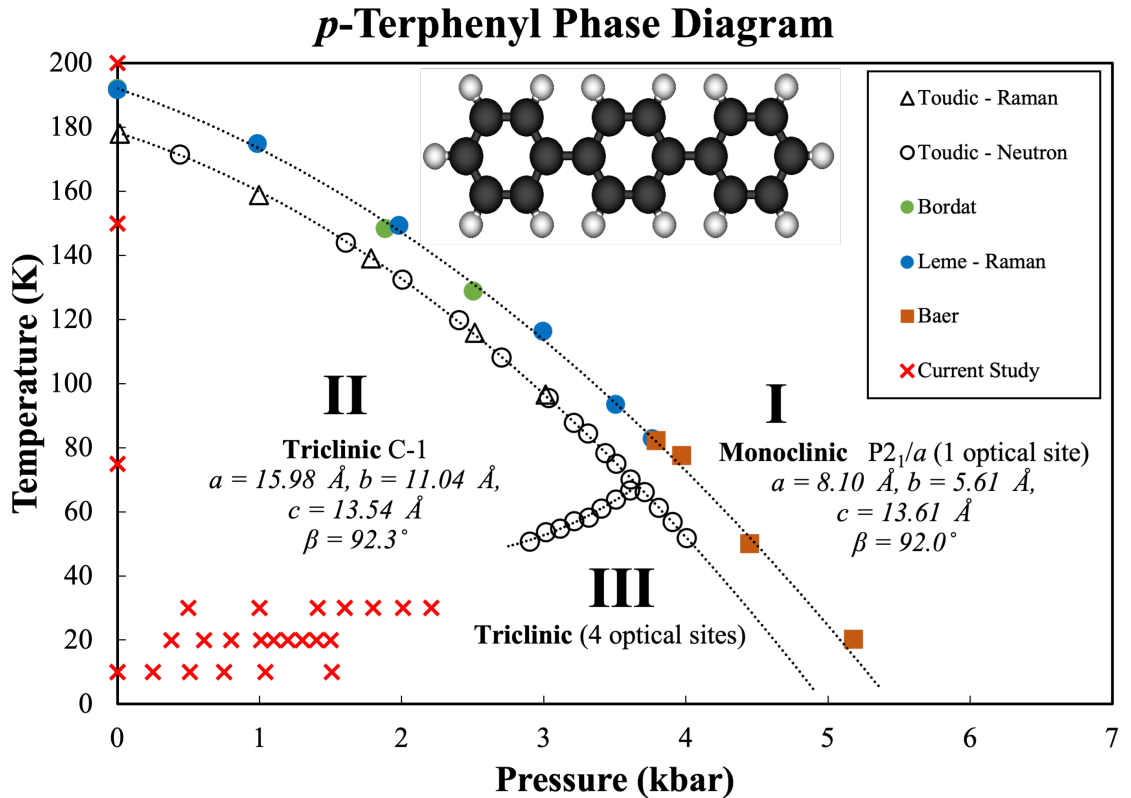


Figure 4.10: Phase diagram of *p*-terphenyl. The open markers represent data collected on deuterated *p*-terphenyl [139][Toudic] through inelastic neutron scattering (open circles) and Raman scattering (open triangles). The filled markers represent Raman scattering data [87] [Leme] (blue filled circles) on *p*-terphenyl and molecular dynamic simulations [18] (green filled circles). The filled orange squares represent optical spectroscopy results on pentacene-doped *p*-terphenyl [49] [Baer]. The green filled triangles show the temperature dependence at ambient pressure. The red symbols indicate the temperature and pressure regime of the current study on crystalline *p*-terphenyl. No solid-solid phase transition is observed in the measured regime. The black dotted lines represent a guide to denote the different solid-solid phase boundaries. A boundary gap exists between the deuterated and nondeuterated *p*-terphenyl.

4.2.2 Experiment

Inelastic Neutron Scattering (INS) experiments were conducted at Lujan Center at Los Alamos Neutron Science Center (LANSCE) and Spallation Neutron Source (SNS) at Oak Ridge National Laboratory. At Lujan Center, the data were collected on the Filter Dif-

ference Spectrometer (FDS) beamline. FDS is an indirect geometry neutron spectrometer that uses a combination of beryllium and beryllium oxide filters to screen neutrons for final energies. [49, 102] The difference spectra were used to improve the resolution and reduce the background. It has an energy resolution about 2~5 percent of the energy transfer. [134] At SNS, the data were collected on the Vibrational Spectrometer (VISION). (See Chapter 2) An aluminum high-pressure gas cell and an aluminum clamp cell were used at FDS and VISION respectively with closed-cycle refrigerators to investigate the vibrational dynamics of p-terphenyl under various temperatures and pressures. Data were collected for p-terphenyl from 10 to 30 K over different pressures up to 1.51 kbar (on the VISION spectrometer) and from 10 to 200 K under the ambient pressure (on the FDS spectrometer). The raw data were background-subtracted, and the temperature-dependent results were corrected for phonon thermal occupation. Slight differences in phonon energies measured by the two instruments are a result of their different reciprocal space coverages.

4.2.3 Results and discussion

The inelastic neutron scattering data on p-terphenyl provide a comprehensive measurement on lattice dynamics and highlight interesting dynamical features of the p-terphenyl crystal system under various pressure and temperature conditions. The FDS experiment was limited to pressures below 680 bar and has lower counting statistics than the VISION experiment so the data from the latter is presented for the pressure-dependent results. Because hydrogen has a neutron scattering cross section 14.8 times that of carbon, the INS vibrational spectra are strongly weighted to modes that involve hydrogen motions. Based on prior Raman spectroscopy work, [164] Infrared (IR) spectroscopy study [122, 151] and

vibrational analysis of PTP, [125] types of motion for most phonon modes can be assigned using the calculation of low-pressure high-temperature monoclinic solid phase. The modes below 20 meV are mainly librational motions that correspond to low-energy long-wavelength phonons; the modes between 20 and 100 meV are primarily the ring deformation modes with the ring breath mode near 76 and 130 meV; Out-of-plane and in-plane C-H bending modes are between 100 and 150 meV; finally, C-C and C-H stretching modes are near 200 and 382 meV respectively. The measured INS spectra are in good agreement with prior Raman and IR measurements, as shown in Table 4.2. Small energy differences are expected because inelastic neutron scattering cover different parts of the reciprocal space for periodic lattices, in which phonons are not localized.

Effect of pressure on phonon energy

The pressure-dependent results at 10, 20, and 30 K are quite similar. The data show pressure-induced changes in both the low-energy and some high-energy modes as illustrated by Figure 4.11. However, these changes are generally small, suggesting no phase transition in this pressure and temperature region. The phonon features are fitted with Gaussian functions to examine the phonon energy shifts. Most of the phonons modes are pressure independent showing small energy shifts. In low-energy librational modes, such as the one at 4.9 meV in Figure 4.11 (d), show slight shifts with increasing pressure. While the high-energy modes have more noticeable shifts. For example, The mode at 24.2 meV in Figure 4.11 (d) stiffens by ~ 0.3 meV monotonically from 0 to 1.51 kbar at 10 K. In contrast, the phonon mode at 23.7 meV softens by ~ 0.3 meV, shown in Figure 4.11 (a). This mode is related to the deformation of the rings and is susceptible to changes

in intermolecular distances under pressure. The phonon mode softens inhomogeneously with enhanced intermolecular interactions induced by increased pressure. It indicates that phonon frequencies do not depend on volume alone as in the quasiharmonic model, revealing significant phonon anharmonicity. The anharmonicity is also suggested by their negative Grüneisen parameters, which are defined as the ratio between relative change in phonon energy as a response to the relative volume change: [42]

$$\gamma_i = -\frac{V}{\nu_i} \left(\frac{d\nu_i}{dV} \right) = -\frac{d \ln(\nu_i)}{d \ln(V_i)}, \quad (4.4)$$

where i is the index of phonon mode, ν and V are the phonon frequency and volume of the unit cell, respectively. This definition is equivalent as the slope in the log-log plot of energy ratio vs volume ratio, as shown in Figure 23. [42] In materials with harmonic or quasi-harmonic phonons, these values are usually small ($< 1 \sim 2$) and positive. To evaluate the Grüneisen parameters from pressure-dependent measurements, isothermal mode Grüneisen parameter can be expressed as: $\gamma_{iT} = -\left(\frac{d \ln(\nu_i)}{d \ln(V_i)}\right)_T = \frac{B}{\nu_i} \left(\frac{d\nu_i}{dP}\right)_T$. The bulk modules from literature, $B = 60.15$ kbar, [140, 10] is used to calculate the volume change as a function of pressure in triclinic crystal.

The results from the pressure-dependent measurements are quite surprising. Five phonon modes below 15.5 meV have been studied at low temperature with pressure dependence and they have similar energy as the pressure dependent Raman results at 300 K. [125, 71] The calculated phonon energy increases from 0 kbar to 33 kbar at low temperature, calculated Grüneisen parameters of these modes are relatively large ($1 \sim 3$) when compared with our pressure dependent results. Such difference might be attributed to the

difference in pressure range and phases (monoclinic and triclinic, respectively) between calculation and our measurement. Our results indicate that the low energy librational modes, related to the intermolecular interactions, are surprisingly harmonic below 1.5 kbar and have more moderate pressure dependence when compared with previous study. [125, 71] The pressure-dependent results suggest that higher pressure is required to drive the solid-solid phase transition to the proposed phase III near these temperatures.

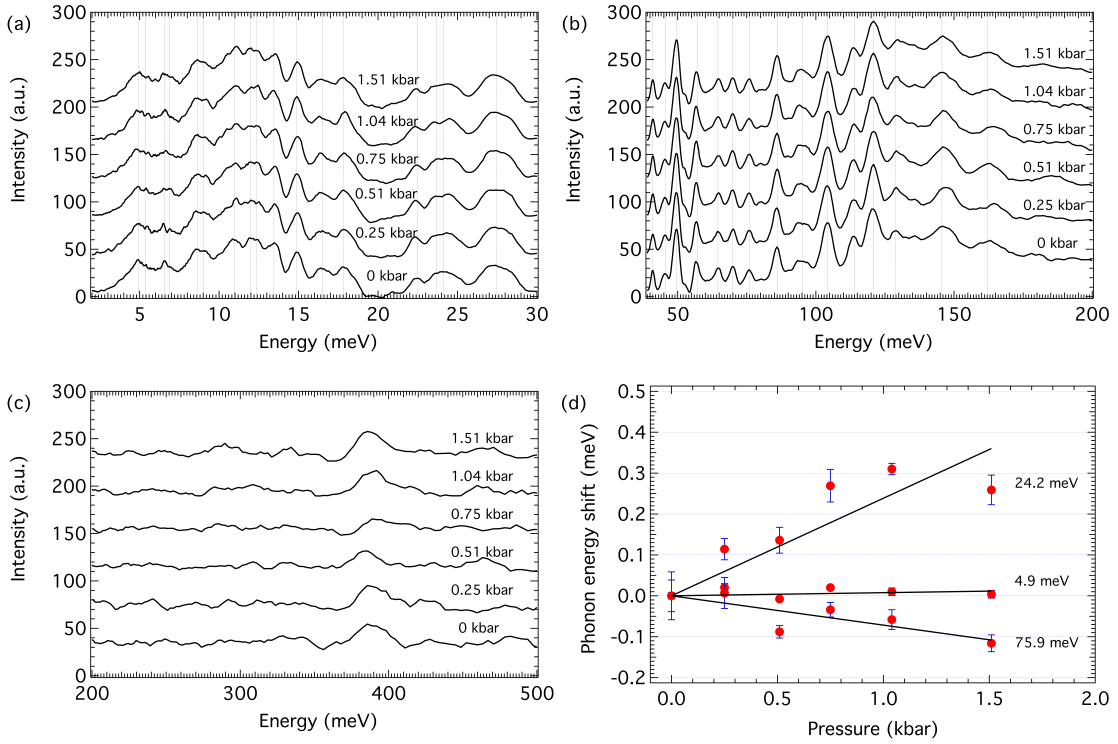


Figure 4.11: Pressure-dependent phonon spectra of para-terphenyl acquired on VISION. (a)(b)(c) Pressure-dependent spectra show only minor changes from 0 to 1.51 kbar at 10 K; (d) The pressure-dependent phonon energy shifts from 0 to 1.51 kbar at 10 K. Peaks in spectra are fitted with Gaussian functions. Error bars indicate the fitting tolerance of phonon energy in spectra. Phonon energies at ambient pressure are labelled and the energy shifts with respect to the energy at 0 kbar are fitted by linear functions. Three representative types of phonon modes are plotted based on the pressure dependence. Phonon mode at 14.9 meV does not show much change with pressure; phonon mode at 75.9 meV softens with increasing pressure; and phonon mode at 24.2 meV stiffens with increasing pressure.

Table 4.2: Phonon modes measured by inelastic neutron scattering compared with the results from Raman and IR spectroscopy. [LMA-long molecular axis, SMA1-short molecular axis (perpendicular to molecular plane), SMA2-short molecular axis (parallel to molecular plane), OP-out-of-plane, IP-in plane, Trans-translation, Lib-libration]. Zig-Zag motion looks like a six C alkane which turns into its mirror image.

Method	INS (meV)	INS (cm ⁻¹)	Raman (cm ⁻¹) [164]	IR (cm ⁻¹) [122]	IR (cm ⁻¹) [151, 47]	Type of Motion [125]
Temperature/K	10	10	5	25	1.3	
	4.9	40	36.3			Lib SMA1
	5.4	43	45.5		45.5	Trans LMA
					49	
	6.6	53	52.2		54	
	6.9	55	57.4		56.5	
	8.6	70	69.8		63	Lib SMA1
	9.0	73			72	OP-LMA bend
					74	
			81.7		81	
					85.5	
	11.0	88.3	90.3		91.5	Symmetric ring twist
	12.0	97.0	95.9			Zig-Zag motion
	12.4	99.6	101.4		102	Trans SMA1 w/ sym outer ring torsion
	13.5	109	108.9		110	Lib SMA2
					114	
	14.9	120	118.6		121	Outer ring twists w/ center ring staying put
	16.5	133	135.7		135	IP-LMA bend
	17.8	144	146.2		135	Lib LMA w/ central ring twist
	22.5	181				
	23.7	191	191.65			
	24.2	195				
	27.4	221	218			Low frequency snake wiggle
			228			
	41.0	330	327			OP-ring torsion
	45.5	367				OP-ring torsion
	49.5	399	394			IP-ring rock
	57.1	460				Ring breathing of outer rings
	64.6	521				OP-ring bend
	69.8	563				OP-ring bend
	75.9	612	610			Ring breathing
	86.0	693		693.1		OP-H-bend
	95.1	767	771	756.3		OP-H-bend
	104.2	840.2	821	846.67		OP-H-bend
	114.1	920.3		921.15		OP-H-bend
	120.9	974.8	991	970.2		
			1005	1016.45		Ring breathing
	145.6	1175	1167			IP-H-bend
			1222			
			1273			
	162.1	1308	1278			IP-H-bend

Effect of temperature on phonon energy

The ambient-pressure temperature-dependent phonon spectra from FDS covers a temperature range from 10 to 200 K for the librational and ring deformation modes, as shown Figure 4.13. Most of these phonon peaks broaden with the increase of temperature because of the reduction in phonon lifetime. It is reported that p-terphenyl by potassium can bring about superconductivity at 123 K. [147, 89] Significant phonon broadening from

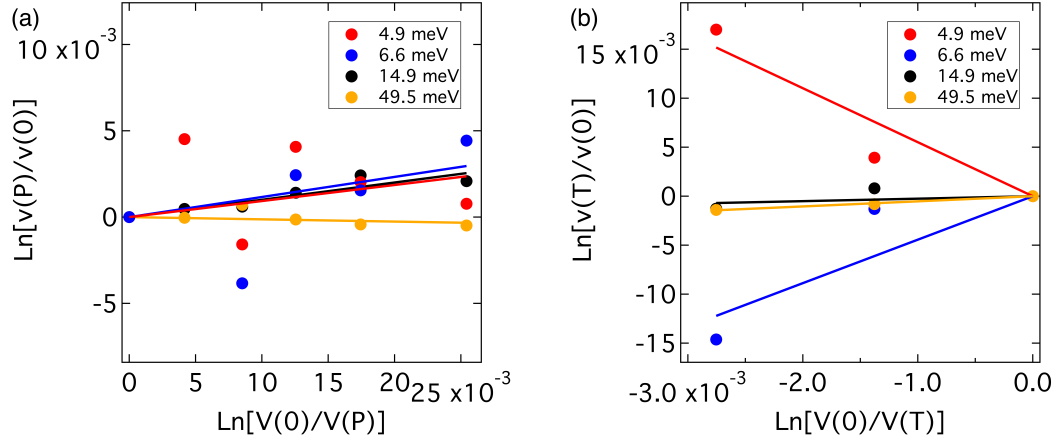


Figure 4.12: The log-log plot of the energy ratio vs. the volume ratio for four vibrational modes at $\nu_1=4.9$ meV, $\nu_2=6.6$ meV, $\nu_3=14.9$ meV, and $\nu_4=49.5$ meV. (a) Pressure dependent data yield the Grüneisen parameters of $\gamma_{1T}=0.09\pm 0.07$, $\gamma_{2T}=0.12\pm 0.07$, $\gamma_{3T}=0.10\pm 0.01$, and $\gamma_{4T}=-0.02\pm 0.01$. (b) Temperature dependent data yield the Grüneisen parameters of $\gamma_{1P}=-5.5\pm 0.9$, $\gamma_{2P}=4.4\pm 1.2$, $\gamma_{3P}=0.3\pm 0.2$, and $\gamma_{4P}=0.5\pm 0.1$. The data points are calculated from the peaks fitting of spectra in Figure 4.11 and Figure 4.14. The lines are linear fits, and their slopes are the mode Grüneisen parameters, γ , with error bars shown in Figure 4.15 (b). The magnitude of γ is larger in the temperature dependent data, especially for the low-frequency librational modes. Linear fitting quality depends on the phonon energy from Gaussian fitting, related to the peak statistics in spectra.

100 K to 200 K suggests the enhanced phonon interactions, including the electron-phonon interactions, which likely influence the superconductivity performance. In general, the result

indicates that overall lattice dynamics remains similar at up to 200 K under the ambient pressure.

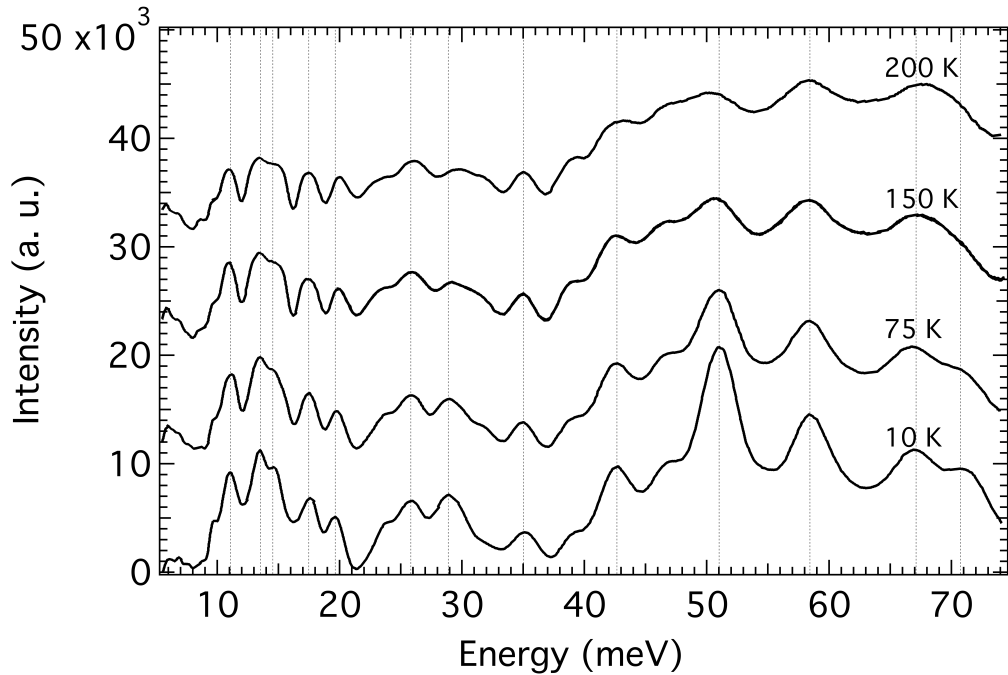


Figure 4.13: Temperature-dependent phonons below 74.4 meV (600 cm^{-1}) acquired on FDS. Temperature-dependent neutron spectra of the low-frequency librational region for p-terphenyl from 10 to 200 K. The spectra were corrected for thermal neutron occupation. There are strong temperature-induced changes in intensity, energy, and linewidth for various phonon modes but no signs of phase transition.

The temperature-dependent phonon spectra below 30 meV near 0.5 kbar show little changes from 10 to 30 K (from VISION spectrometer, Figure 4.14 (a)), even for librational bands below 8 meV. This is expected because below 30 K these phonon modes are barely excited. The results also indicate that the boundary of solid-solid phase transition needs to be at lower temperature and/or higher pressure. Phonons in materials usually soften (decrease in energy) at elevated temperature due to the thermal expansion, resulting

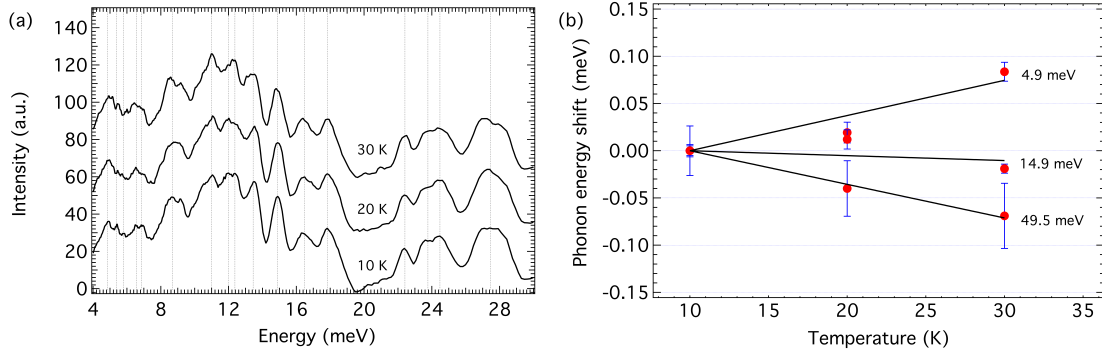


Figure 4.14: Temperature-dependent phonon spectra of p-terphenyl acquired on VISION. (a) Temperature-dependent phonon spectra of the low energy modes at 0.5 kbar; (b) The pressure-dependent phonon energy shifts from 10 K to 30 K at 0.5 kbar. Error bars indicate the fitting tolerance of phonon energy in spectra. Phonon energy at 10 K is labelled at the first points and the lines are linear fits.

in positive Grüneisen parameters. In p-terphenyl, the results are quite complicated, as shown in Figure 4.14 (b). While some modes, such as the ones near 49.5 and 64.7 meV (399 and 522 cm^{-1}), behave normally; some other modes, such as the ones at 4.9 and 75.8 meV (40 and 611 cm^{-1}), move to higher energy with the increase of temperature. The temperature dependence of mode at 4.9 meV looks different from that of Raman results. [164] We have much broader access to the modes beyond zone center, so the different trends are not in conflict. Most other phonon modes are nearly temperature independent, such as the modes at 45.5 and 69.8 meV (367 and 563 cm^{-1}).

Taking into account the thermal expansion, the effective mode Grüneisen parameters in equation (4.4) are calculated based on temperature-dependent phonon spectra. Isobaric mode Grüneisen parameter can be expressed as: $\gamma_{iP} = -\left(\frac{d\ln(\nu_i)}{d\ln(V_i)}\right)_P = -\frac{1}{\alpha\nu_i}\left(\frac{d\nu_i}{dT}\right)_P$ where α is the thermal expansion coefficient (Mentioned in equation (4.3)). Triclinic lattice structure is used to calculate the temperature dependent volume. The volumetric ther-

mal expansion is calculated from the anisotropic linear thermal expansion coefficients. [11] It should be noted that the thermal expansion is anisotropic in this material. The mode Grüneisen parameters calculated from temperature- and pressure-dependent data, γ_{iP} and γ_{iT} , differ significantly, as shown in Figure 4.12, and Figure 4.15. The mismatch between the two sets of Grüneisen parameters is a strong indication that their associated phonon modes are very anharmonic and such anharmonicity might be related to the phase instability near the solid-solid phase transition. In particular, while the pressure data show moderate Grüneisen parameters between ± 1 , the temperature data show much larger effective Grüneisen parameters between ± 6 .

The total energy change with temperature dependence can be expressed as [16]:

$$\left(\frac{d\nu_i}{dT}\right)_P = \left(\frac{d\nu_i}{dT}\right)_{implicit} + \left(\frac{d\nu_i}{dT}\right)_{explicit}. \quad (4.5)$$

In equation (4.5), $\left(\frac{d\nu_i}{dT}\right)_P$ represents the temperature dependent isobaric energy shift, consisting of implicit and explicit contributions. Here, the implicit part arises from the energy change induced by volume change with temperature (quasiharmonic contributions), the explicit part is attributed to the anharmonic contributions due to phonon interactions. Equation (4.5) can be used to build a relation between $\gamma_{iP}(T)$ and $\gamma_{iT}(T)$ as: $\gamma_{iP}(T) = \gamma_{iT}(T) + \gamma_{iV}(T)$, in which temperature dependent Grüneisen parameter under constant volume, $\gamma_{iV}(T)$, represents anharmonic contributions to the phonon energy shift. In quasi-harmonic approximation, $\gamma_{iV}(T) = 0$, so $\gamma_{iP}(T) = \gamma_{iT}(T)$, Only volume change contributes to the total phonon energy shift. Thus, the contradiction between $\gamma_{iP}(T)$ and $\gamma_{iT}(T)$ in our results suggests that quasi-harmonic approximation cannot describe the temperature dependence of phonon modes in p-terphenyl

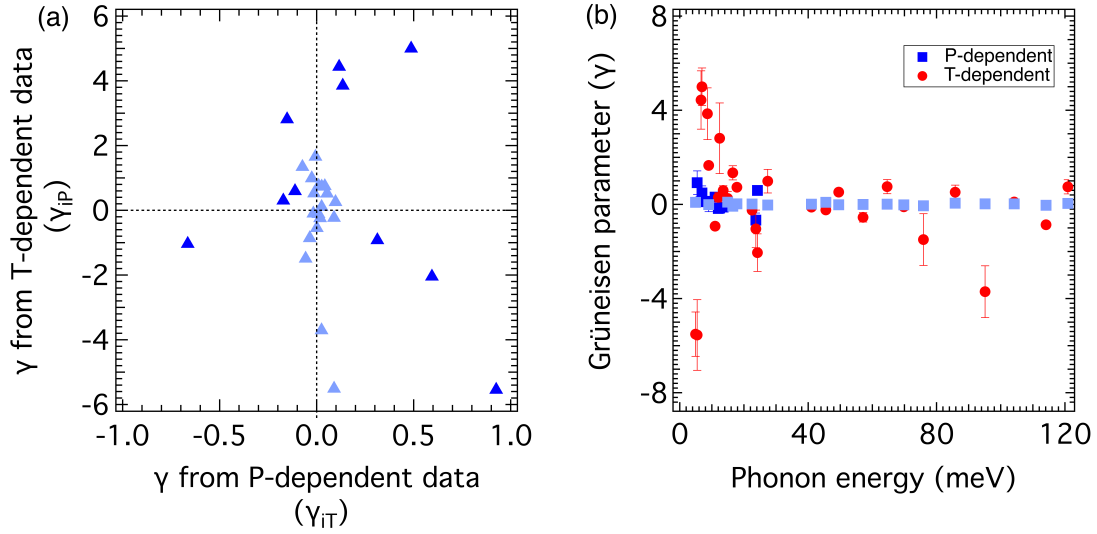


Figure 4.15: The comparison between the Grüneisen parameters calculated from temperature- and pressure-dependent data. Large differences are found with no simple correlations between them. The temperature dependent Grüneisen parameters show large variations. Light blue symbols in (a) and (b) represent the modes with little pressure dependence.

Significant contributions from anharmonic phonon potentials could be attributed to the low-symmetry lattice structure and the phonon eigenmodes but could also be related to the strong electron-phonon interactions. In the potassium-doped p-terphenyl crystals, the vibrational properties could play an important role in the formation of Cooper pairs induced by electron-phonon couplings with high energy phonons. [113] Electronic properties and superconductivities of alkaline-earth metal-doped phenanthrene, also one of the polycyclic aromatic hydrocarbons, have also been studied. [45] From prior electron-phonon interaction simulations, phonons induced by C-H vibrations and the coupling among molecules, with energy at 20 meV \sim 200 meV, were shown to have strong electron-phonon coupling. From our data, phonons below 200 meV in crystalline p-terphenyl are also related to the molecular coupling and C-H vibrations, similar to the potassium-doped p-terphenyl case.

Such phonons may participate in electron-phonon interactions and enhance the superconductivity. Therefore, the measured phonon anharmonicity in our work could be valuable to the study of electron-phonon interactions in p-terphenyl and the related high-temperature superconductivity.

Phase transition estimation

Together, the pressure- and temperature-dependent phonon spectra provide some insights on the lower end of the boundary separating phase II and III (Figure 4.10). The measurements suggest that this phase boundary may have an intercept at $T = 0$ K above 2 kbar. The boundary of phase II and III has only been reported for deuterated p-terphenyl in Figure 4.10. Thus, it is possible that such phases transition may not even exist in p-terphenyl. It is also likely that the phase boundary is shifted to higher temperature (e.g., + 10 to + 20 K) and higher pressure (e.g., + 0.5 kbar), analogous to the shift in the phase I/II boundary between deuterated and nondeuterated samples. However, it is also possible that the phase boundary terminates at a critical point beyond measured region.

4.2.4 Conclusion

The temperature- and pressure-dependent phonon lattice dynamics measurements on p-terphenyl were conducted by inelastic neutron scattering. The low-temperature high-pressure results indicate the absence of a solid-solid phase transition between 0 and 1.51 kbar at 10 ~ 30 K and the lattice dynamics remains similar at up to 200 K under ambient pressure. The results suggest a likely positive intercept or critical point above 2 kbar for the solid-solid phase boundary. It is also possible that this phase II/III boundary is shifted to

higher temperature and higher pressure, analogous to the shift in the phase I/II boundary. The inelastic neutron scattering results also show a variety of energy dependence of different phonon modes with respect to temperature and pressure. The large discrepancy between the Grüneisen parameters calculated from temperature- and pressure-dependent spectra indicates strong anharmonicity in the librational phonon modes.

4.3 Quantify the Van der Waals interactions in layered PdSe₂

Van der Waals (vdW) force, weakly holding the layers together in two-dimensional (2D) materials, plays a key role in many physical properties, such as superconductivity and quantum Hall effect. Quantifying the vdW force, therefore, is essential for understanding the fundamental mechanisms of these novel properties. However, due to the difficulty of probing the interlayer forces directly, it is still a challenge to quantify the vdW interactions effectively. Here, by using IXS technique with diamond anvil cell, we quantified the vdW interactions through the investigation of pressure-dependent acoustic phonons, especially the classical flexure mode (ZA), in 2D-layered palladium diselenide (PdSe₂). To our best knowledge, the evolution of ZA with pressure was characterized for the first time. The interlayer binding changes from the weak vdW force to the covalent bond while the orthorhombic structure of PdSe₂ evolves into a cubic one (from ambient pressure to 6 GPa). The interlayer-related elastic constants and the compression and shear force constants all show linear relations with pressure. These results indicate that the interlayer vdW interactions increased dramatically with increasing pressure and the covalent bond takes over after phase transition. Our work not only quantifies the pressure-dependent ZA mode, but also, more significantly, paves a new path to measure the vdW interactions in 2D materials.

4.3.1 Introduction

In 2D-layered materials, vdW force holds together the neighboring atomic layers, while stronger covalent or ionic bond holds the atoms together in the layers, leading to the anisotropy of crystal structures. Many unique physical properties and applications, such

as high temperature superconductivity, [158] ferromagnetism, [70] and anomalous lattice vibrations, [132, 83] have been reported to relate closely to the interlayer vdW interactions of 2D-layered materials. Therefore, measuring and tuning the vdW interactions are essential in exploring the extraordinary properties in 2D-layered materials. To date, various methods have been attempted to quantify the vdW interactions: atomic force microscopy (AFM) measurement, [66] Raman, [66, 7] and pressure enhanced band splitting. [32] However, due to the limited capability in measuring the force and potential between the neighboring atomic layers, more efficient and accurate quantification of vdW interactions is still in urgent need.

Due to the weak interlayer vdW interactions, the phonon dispersions of 2D-layered materials are extremely sensitive to pressure. As is known, the elastic constants, which describe relationship between stress and strain in solids, can be extracted from the acoustic phonons by using the semi-continuum model. [107, 74] In the acoustic phonons in 2D-layered materials, the flexural ZA mode is tightly related to the interlayer weak vdW interactions. [149] Thus, probing the pressure-dependence of ZA mode is expected to obtain the pressure-dependence of elastic constants related to vdW forces. Generally, phonon dispersion of materials with small flake sample can be obtained successfully by IXS at ambient pressure. [148] However, it is difficult to obtain the pressure dependence of phonon modes on layered materials, especially the ZA mode, because the sample and beam scattering geometries are both significantly limited by the diamond anvil cell (DAC). [40] Therefore, it is still a challenge to investigate the pressure-dependence of ZA mode in 2D-layered materials.

Palladium diselenide (PdSe_2), one of the 2D-layered transition metal dichalcogenides family, has attracted ever-increasing interests recently. It shows various promising

applications due to its anisotropic thermal conductivity, [148] multiple phase transition, [40] negative Poisson's ratio, [95] and photovoltaic properties. [86] PdSe₂ undergoes a phase transition from an orthorhombic structure (Pbca) with a square-planar of Pd atoms to a cubic structure ($Pa\bar{3}$) with an octahedral of Pd atoms when hydrostatic pressure reaching 6 GPa (Figure 4.16). [131] The vdW force between layers increases and the layer spacing decreases gradually when increasing pressure before phase transition; the vdW force disappears and the neighboring layers are connected by the covalent bond after phase transition. Thus, such structural evolution of PdSe₂ provides a natural advantage to probe the evolution of vdW interactions.

Here, we report a new method to study the vdW interactions through the acoustic phonons measured by pressure-dependent IXS in layered PdSe₂. The pressure-dependent dispersion of acoustic phonons, especially of the ZA mode, were measured at 0.36, 1.85, 3.7, and 6 GPa. Phase transition is observed when the hydrostatic pressure is increased to 6 GPa. With increasing pressure, the interlayer interactions become stronger and are taken over by the covalent bond after phase transition, and were confirmed by the significant increasing of interlayer-related mechanical parameters extracted from the measured acoustic phonons. The elastic constants, C_{33} and C_{44} , are respectively increased by 6 and 8 times, and the interlayer compression and shear force constants, f_{direct} and f_{shear} , are respectively increased by 3.5 and 6 times through the phase transition. These results provide insight on the detailed evolution of vdW interactions in 2D-layered PdSe₂.

4.3.2 Experiment and calculation

High-pressure inelastic X-ray experiment

High quality 2D-layered PdSe₂ single crystal in this work was purchased commercially and grown by the chemical vapor transport method. The quality of the crystal was checked by X-ray diffraction shown in Figure 4.17 (a). The full width at half maximum (FWHM) of Bragg peak at (002) plane is about $0.24 \pm 0.01^\circ$, showing high crystalline quality of the sample (inset in Figure 4.17 (a)).

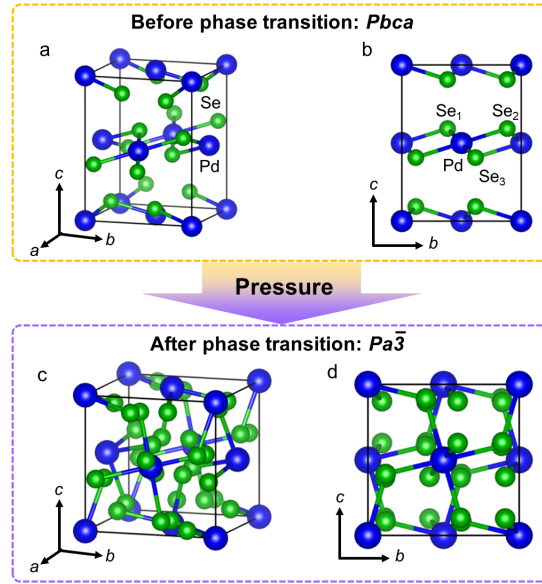


Figure 4.16: Crystal structures of layered PdSe₂. a and b are the front and side views of the orthorhombic structure with space group *Pbca* before phase transition, respectively, while c and d are the front and side views of the cubic structure with space group *Pa* $\bar{3}$ after phase transition, respectively. The arrow with color from yellow to purple represents the increasing of pressure.

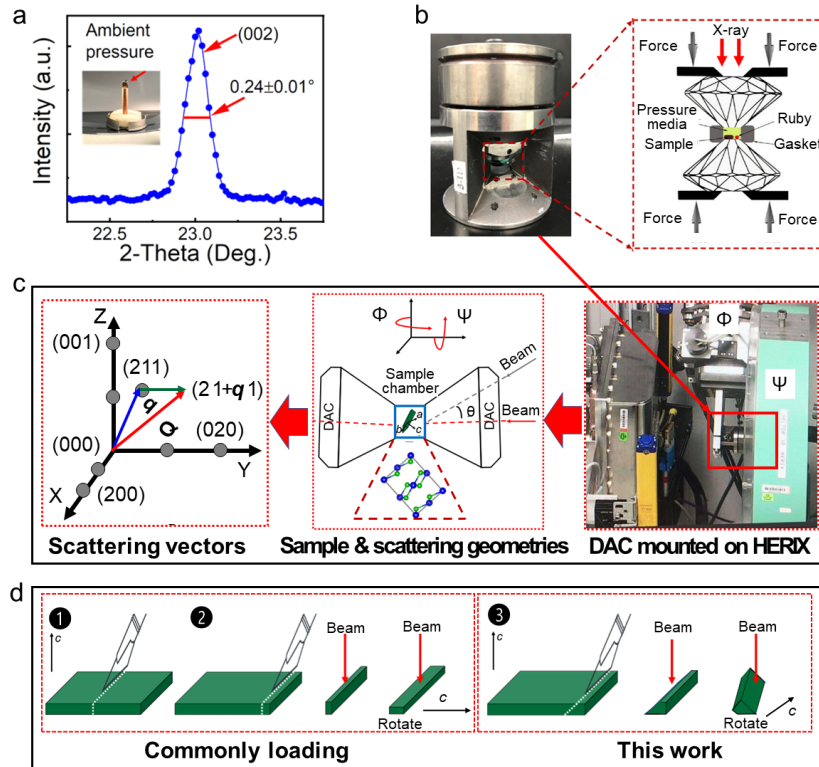


Figure 4.17: Sample preparation for pressure-dependent IXS measurement of 2D-layered PdSe₂ single crystal. a, Rocking curve for (002) Bragg peak of PdSe₂ crystal. The narrow peak width indicates by the arrow shows high crystalline quality. Inset is the sample attached on a copper post for the ambient pressure measurement. b, Sample loading for high-pressure measurement with panoramic DAC. Left and right panels are the object and schematics of DAC, respectively. c, Schematic of the beam scattering geometry for the high-pressure experiment. Solid red frame in the right panel shows the DAC mounted on HERIX. Middle panel shows the sample and beam scattering geometries. Left panel shows the scattering vectors in zone (211). d, Sample geometry for ZA mode measurement under high pressure. The first and second methods are commonly used for high-pressure IXS measurement, while the third one is the method used in this work.

High energy resolution IXS experiment was performed to measure the acoustic phonons of PdSe₂ under ambient pressure (≈ 0), 0.36, 1.85, 3.7, and 6 GPa at room temperature. The measurements were conducted at 30-ID-C (HERIX) at Advanced Photon Source, Argonne National Laboratory. [121, 135] The detailed measurement under ambient pressure can be found from our previous work. [148]

For high pressure measurements, a small crystal ($80 \mu m \times 50 \mu m \times 40 \mu m$) was loaded in a panoramic diamond anvil cell (DAC) (Figure 4.17 (b)), and the DAC was aligned parallel to the electric field vectors of incident X-ray (right panel in Figure 4.17 (c)). Culet size of DAC was $800 \mu m$, and rhenium with thickness at $250 \mu m$ was used as the gasket. The gasket was pre-indented to $120 \mu m$ and a $400 \mu m$ hole was drilled. Helium was used as the medium to minimize the background and ensure the hydrostatic pressure inside the chamber. Ruby fluorescence excited by 532 nm laser was used to measure the hydrostatic pressure. After gas loading, the initial pressure was 0.36 GPa, which was increased to 1.85, 3.7, and 6 GPa by step. Sample quality and the orientation matrix were checked before the measurements at each pressure. At specific wave vector transfer (\mathbf{Q} point), the counting time at each energy step is set as $60 \sim 120 \text{ s}$. Due to the relative low statistics under high pressure, 3 or 5 scans were performed at each \mathbf{Q} point and the data are combined for analysis.

Sample geometry was designed specially for the ZA mode measurement. As shown in the right and middle panels in Figure 4.17 (c), when the DAC was mounted on the rotational stage, the incident beam angle is limited by the opening angle of DAC, the Φ angle of the rotational stage is fixed, the Ψ angle has a certain degree of rotational freedom,

and thus the beam scattering geometry is extremely limited. In order to measure the ZA mode, a Brillouin zone (BZ) with out-of-plane value and the q points along in-plane direction should be reached. Thus, if the single crystal sample is cut regularly as the first and second methods shown in Figure 4.17 (d) and loaded lying on the diamond, there are two problems should be concerned: a) the obtained BZ only along one of the high-symmetry directions, which limits the rotation along the other direction; b) although the crystal is loaded along the right direction, it is difficult to keep the direction after He gas loading. In these cases,

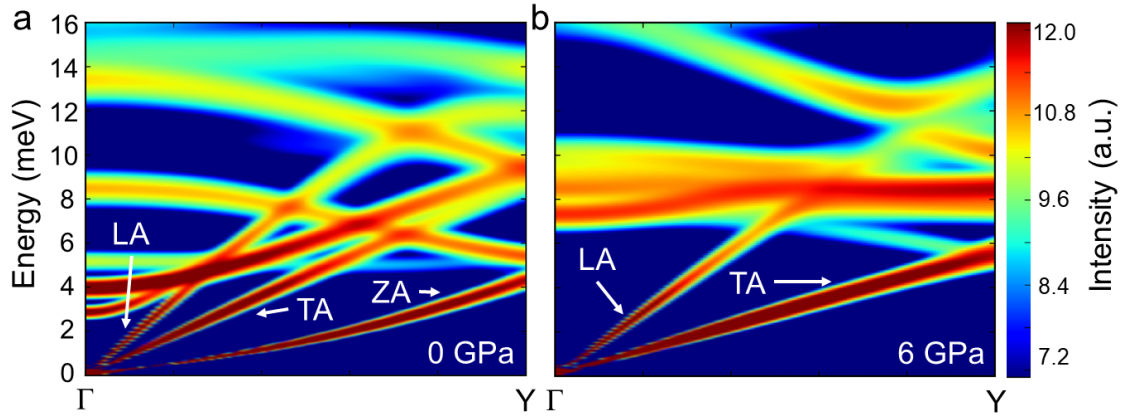


Figure 4.18: Calculated dynamic structure factors of PdSe₂ along Γ -Y direction by IXS at zone $(2 \ 1+\mathbf{q} \ 1)$ under 0 GPa (a) and 6 GPa (b). Arrows indicate the longitudinal, transverse, and flexural acoustic modes (LA, TA, and ZA). Color bar indicates the phonon intensity plotted on a logarithmic scale.

the scattering geometry and the rotation matrix can not satisfy the requirement for ZA measurement. Here, we use the third method in Figure 28 (d), where the sample is cut with a certain angle along an arbitrary direction between the c -axis. In this case, a cross-plane

BZ can be easier obtained, and the sample is more stable during gas loading, maintaining the scattering geometry. The $(2\ 1+\mathbf{q}\ 1)$ zone was obtained for ZA mode measurement after He gas loading (left panel in Figure 4.17 (c)), and other phonons were also measured except for ZA according to dynamic structure factor $S(\mathbf{Q}, E)$ simulation (Figure 4.18).

Phonon calculation

First-principles calculations were performed based on the density functional theory (DFT) as implemented in the Vienna Ab Initio Simulation Package (VASP). [76] The generalized gradient approximation (GGA) Perdew-Burke-Ernzerhof (PBE) functional was used for structural relaxations with plane-wave cut-off energy of 600 eV. The optPBE functional [73] was used to estimate the vdW force due to layered structure of PdSe₂. [136] The BZ of the reciprocal space was sampled by a Γ -centered grid of $5 \times 5 \times 4$. The force components of each atom were smaller than 0.001 eV/Å and the difference of total energy was less than 10⁻⁶ eV during the structure relaxation. The Phonopy code [137] was used to calculate the phonon dispersion of PdSe₂. In this approach, the second-order interatomic force constants were computed by the finite difference method in a $2 \times 2 \times 2$ supercell. The lattice constants at each hydrostatic pressure were used from the measurements by HERIX.

4.3.3 Results and discussion

Phase transition under high pressure

Phase transition under pressure is determined by tracking the variance of lattice constants. Before measuring the phonon dispersions, it is necessary to check the sample quality and confirm that the sample is intact under high pressure. Due to the limited 2-theta

angle by the opening angle of DAC, only several crystal planes on lower-order BZ can be observed (Figure 4.19). As shown in Figure 4.21 (a), each (211) plane holds a relatively sharp peak under pressure, which is partially reflected by the bright Bragg points in Figures 4.19 (a) and (b), indicating high quality of the sample and good agreement with the predictions. The 2-theta increases with increasing pressure below 6 GPa due to the reduction of lattice constants and then drops to the minimum value at 6 GPa. Figure 4.21(c) shows that the in-plane lattice constants, a and b, and unit cell volume V declines moderately with increasing pressure, while the drop of out-of-plane lattice constant c is more significant with pressure. The sharp drop of c and V indicates the structure transition from 3.7 (orthorhombic) to 6 GPa (cubic), which is also revealed by the increased systematic free energy from our calculation (Figure 4.20) and in agreement with previous work. [97] The detailed diffraction and lattice information versus pressure can be found in Table 4. The ratios of a/c and b/c increase with the increasing pressure, implying the compression along c-axis and the structure evolution of PdSe₂. By fitting the trend of the lattice constants versus pressure from equation $y = A + Bx + Cx^2$, it is found that the reduction of c (B=0.041, C=0.005) is larger than that of a (B=0.023, C=0.003) and b (B=0.026, C=0.003). This behavior reveals the negative Poisson's ratio in the orthorhombic structure of PdSe₂, which confirms the prediction in monolayer PdSe₂ to some extent.

Further exploring this phase transition, the bond length, energy integrated crystal orbital Hamiltonian population (ICOHP), and force constants were calculated to evaluate

Table 4.3: Pressure-dependent lattice information of PdSe₂.

Space group	Pressure (GPa)	2-Theta (Deg.)	FWHM (Deg.)	<i>a</i> (Å)	<i>b</i> (Å)	<i>c</i> (Å)	<i>V</i> (Å ³)	<i>a/c</i>	<i>b/c</i>
<i>Pbca</i>	Ambient	12.26	0.08	5.741	5.868	7.705	259.6	0.745	0.762
	0.36	12.27	0.09	5.74	5.866	7.691	258.9	0.746	0.763
	1.85±0.2	12.33	0.09	5.71	5.835	7.649	254.8	0.747	0.763
	3.7±0.3	12.36	0.09	5.7	5.826	7.639	253.4	0.748	0.764
	6±0.4	12.08	0.09	6.08	6.08	6.08	224.7	1	1

Table 4.4: Fitted data from LA mode along Γ –Y of PdSe₂.

Pressure (GPa)	v_L (m/s)	ρ (g/cm ³)	C_{22} (GPa)
Ambient	5874	6.764	233
0.36	5914	6.78	237
1.85±0.2	6124	6.89	258
3.7±0.3	6704	6.92	311
6±0.4	5292	7.811	219

Table 4.5: Fitted data from TA mode along Γ –Y of PdSe₂.

Pressure (GPa)	v_T (m/s)	ρ (g/cm ³)	C_{66} (GPa)
Ambient	2653	6.764	48
0.36	2703	6.78	50
1.85±0.2	2963	6.89	60
3.7±0.3	3286	6.92	75
6±0.4	2105	7.811	35

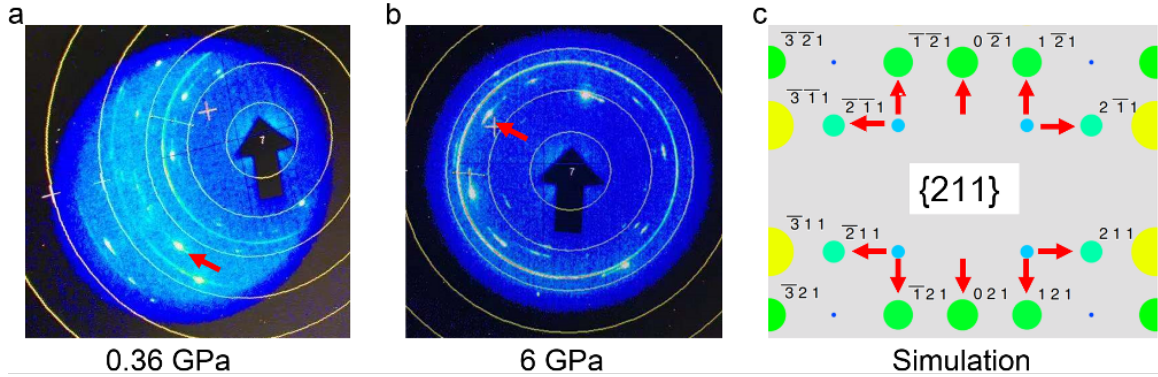


Figure 4.19: Diffraction patterns of (211) plane of PdSe₂. Patterns at 0.36 GPa (a) and 6 GPa (b) show the phase transition and indicate the high quality of the single crystal sample. The yellow circles are the reference line for sample alignment. (c) Simulation of the reciprocal space of PdSe₂ along the experimental view axis. The red arrows indicate the (211) plane group.

the evolution of bonds versus pressure, shown in Figures 4.21 (d)-(f). For Pd-Se₁ and Pd-Se₂ bonds, the bond lengths increase, and the bond strengths (ICHOP) decrease gradually with the increasing pressure. While for Pd-Se₃, the bond length decreases, and the bond strength increase significantly with the increasing pressure. The force constant of heavier Pd-Pd (Pd: 106.4 > Se: 78.97), which dominates the phonon energy around BZ center, increases gradually along a- and b-axis below 6 GPa and drop down at 6 GPa, while they keep increasing along c-axis with the increasing pressure. As reported, the octahedral [PdSe₆] evolves a Jahn-Teller distortion during the phase transition: in orthorhombic structure, the low spin configuration $(z^2)^2(x^2 - y^2)^0$ induces the square-planar [PdSe₄] (composed by Pd-Se₁ and Pd-Se₂), while in cubic structure, the high spin configuration $(z^2)^1(x^2 - y^2)^1$ induces the octahedral [PdSe₆] (composed by Pd-Se₁, Pd-Se₂, and Pd-Se₃ in orthorhombic structure) (Figure 4.21 (b)). Such distortion will lead to weaker in-plane and stronger out-of-plane binding of Pd and Se atom at 6 GPa than below that. [78, 150]

Table 4.6: Fitted data from ZA mode along Γ -Y of PdSe₂.

Pressure (GPa)	ρ (g/cm ³)	C_{44} (GPa)	b_y (mm ² /s)
Ambient	6.76	4.59	1.43
0.36	6.78	6.14	1.42
1.85±0.2	6.89	9.10	1.28
3.7±0.3	6.92	20.33	1.02
6±0.4	7.81	36.60	—

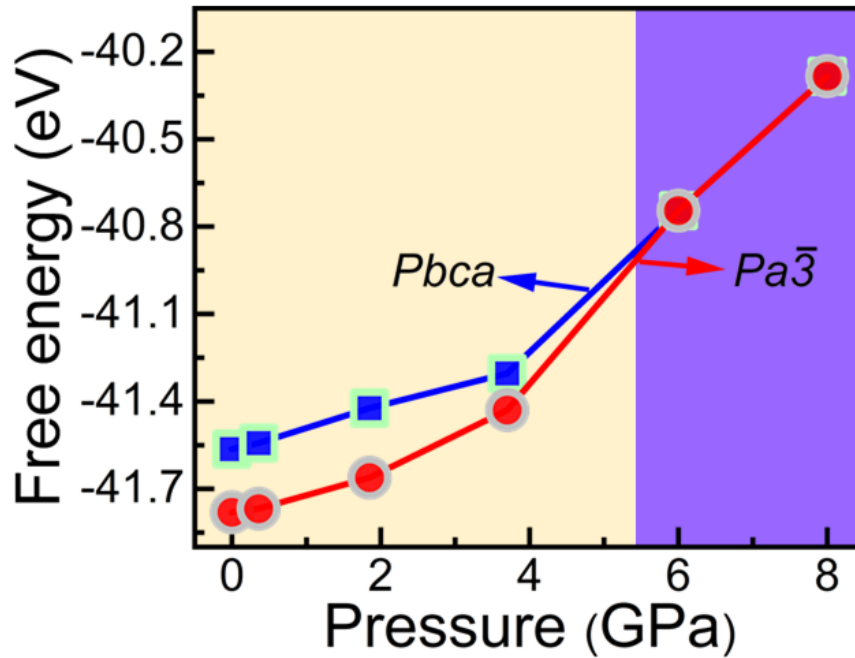


Figure 4.20: Calculated systematic free energy of PdSe₂ with pressure. Yellow and purple shadows represent before and after phase transition, and the position of interface is estimated from ref. [131]

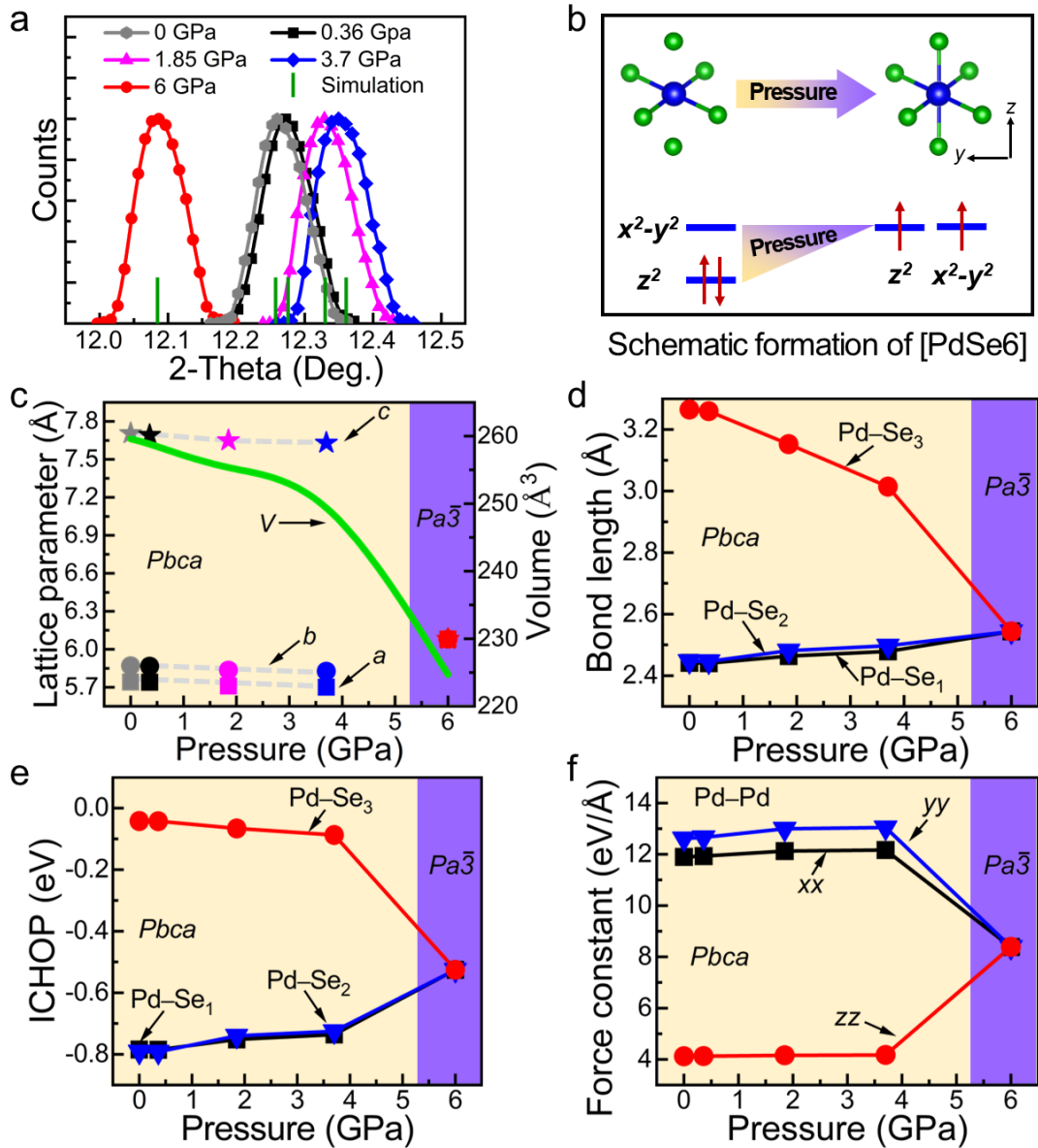


Figure 4.21: Pressure-dependent crystal change of PdSe₂. a, Bragg peak of (211) plane by HERIX. The vertical green solid lines are the predictions by Single Crystal software. b, Schematic formation of octahedral [PdSe₆] from the orthorhombic to cubic structure, including the orbital correlation, reproduced from ref. [97]. c, Pressure-dependent lattice constants and the volume. Dashed lines are the fitting curves from $y = A + Bx + Cx^2$. Green curve is guide for eyes. d and e are the bond length and ICOHP of Pd-Se₁, Pd-Se₂, and Pd-Se₃, respectively. f, Force constant of Pd-Pd. Yellow and purple shadows represent before and after phase transition, and the position of interface is estimated from ref. [97].

Pressure dependence of ZA mode

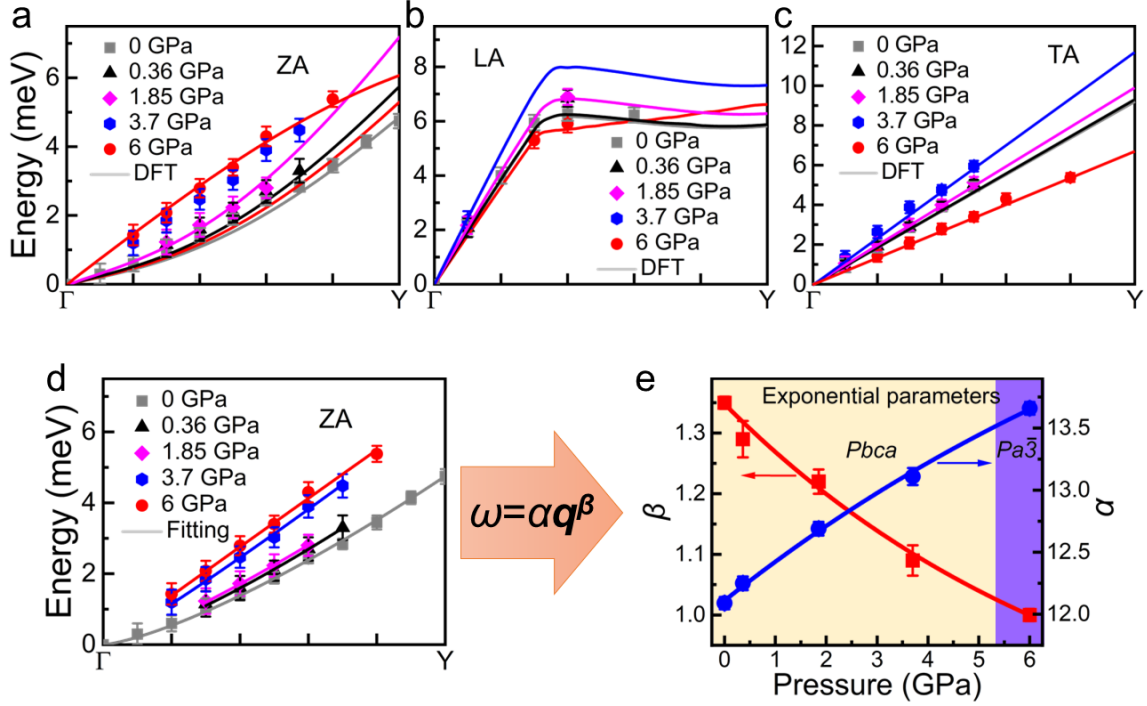


Figure 4.22: Pressure-dependent acoustic phonon dispersions along Γ – Y of PdSe_2 . a–c, Measured phonon modes of LA, TA, and ZA branches (symbols), overlaid with the corresponding first-principles calculations (lines). d, Exponential fittings of the ZA branches with $\omega = \alpha q^\beta$ function (arrow). e, Pressure-dependent fitting parameters α and β . Error bars are the fitting uncertainty. Shadows represent the different structures as described in previous figures.

The lattice constants of PdSe_2 are sensitive to the pressure, so phonon dispersions will change with pressure as well, especially for the ZA mode. Figures 4.22 (a)–(c) show the pressure-dependent acoustic phonon dispersions along Γ – Y direction obtained by IXS (the calculated low-energy phonon dispersions of PdSe_2 under pressure are shown in Figure

4.23). It is found that our first-principles calculation shows excellent agreement with the measurements for LA and TA phonons under pressure (Figure 4.22 (b) and Figure 4.22 (c)), but it is unable to predict the pressure dependence of ZA phonons (Figure 4.22 (a)). This discrepancy may result from the pressure dependent vdW interactions which may not be accurately described by the optPBE functional, though it shows good accuracy to estimate the lattice constant at ambient condition. Furthermore, unlike the trend of TA and LA with pressure, the ZA mode keeps stiffening as the pressure increases. This behavior mainly results from the evolution of the lattice constants with pressure: In-plane lattice constants a and b decrease continuously before phase transition and increase significantly after that, while c keeps decreasing with the increasing pressure up to 6 GPa. Thus, the slope of featured flexural ZA mode in 2D-layered PdSe₂ around the BZ center steepens with increasing pressure, as reflected by the increasing Pd-Pd force constant along c -axis in Figure 4.21 (f).

To our knowledge, it is the first experiment to measure the ZA dispersion curves with pressure dependence in 2D-layered materials. Due to the failure of first-principles calculations in estimating the pressure-dependent phonon energy in ZA mode, the exponential function, $\omega = \alpha \mathbf{q}^\beta$, is applied to fit the measured phonon energy of ZA, [64] showing the excellent agreement. As shown in Figures 4.22 (d) and (e), with increasing pressure, the ZA dispersion curve evolves toward linear gradually and the exponential coefficient β decreases from 1.35 to 1. As is known, the dispersion curve exhibits a parabolic behavior in monolayer materials, and β is usually smaller than 2 in the bulk 2D-layered materials due to the existing interlayer vdW force. After phase transition, the dispersion curve is linear

($\beta = 1$). The change of β indicates that the interlayer vdW force increases gradually with the increasing pressure in the orthorhombic structure and is taken over by the covalent bond after phase transition in the cubic structure. These results present the evolution of the pressure-dependence of ZA mode in PdSe₂, and provide significant reference for other related 2D-layered materials to investigate the ZA mode.

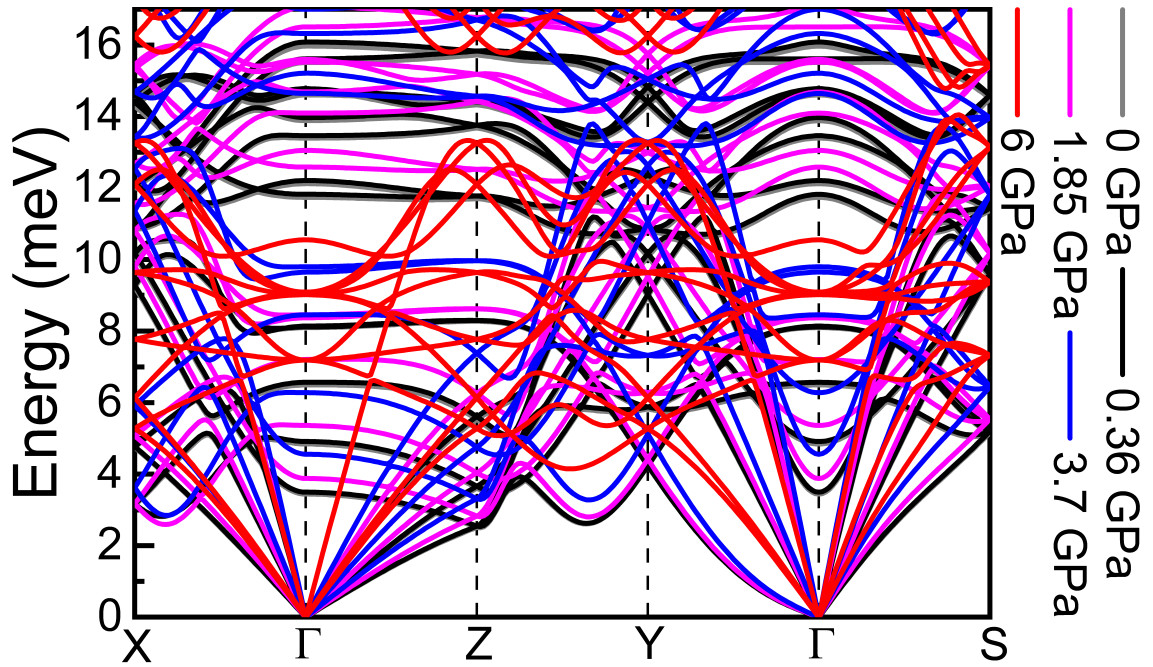


Figure 4.23: Calculated low-energy phonon dispersions of PdSe₂ under each pressure.

Quantification of the vdW interactions

The elastic constant, representing the stress-strain relationship in materials, is highly sensitive to the pressure. The vdW interactions can be quantified through their

corresponding elastic constants. The pressure-dependent elastic constants can be extracted from the acoustic phonons by using the semi-continuum model [107]:

$$v_{LA(\Gamma-Y)} = \frac{\omega}{\mathbf{q}} = \sqrt{\frac{C_{22}}{\rho}}, v_{LA(\Gamma-Z)} = \frac{\omega}{\mathbf{q}} = \sqrt{\frac{C_{33}}{\rho}}, v_{TA(\Gamma-Y)} = \frac{\omega}{\mathbf{q}} = \sqrt{\frac{C_{66}}{\rho}}, \quad (4.6)$$

where v is the phonon group velocity near BZ center, ω the phonon energy, ρ the mass density and \mathbf{q} the wavevector. For the ZA mode, we can obtain both C_{44} and the bending elastic parameter by fitting the ZA dispersion from the following equation [74] (Figure 4.24):

$$\omega^2 = \frac{C_{44}}{\rho} \mathbf{q}^2 + b_y^2 \mathbf{q}^2, \quad (4.7)$$

b_y represents the resistance of a layer to bend. The detailed fitted group velocities from

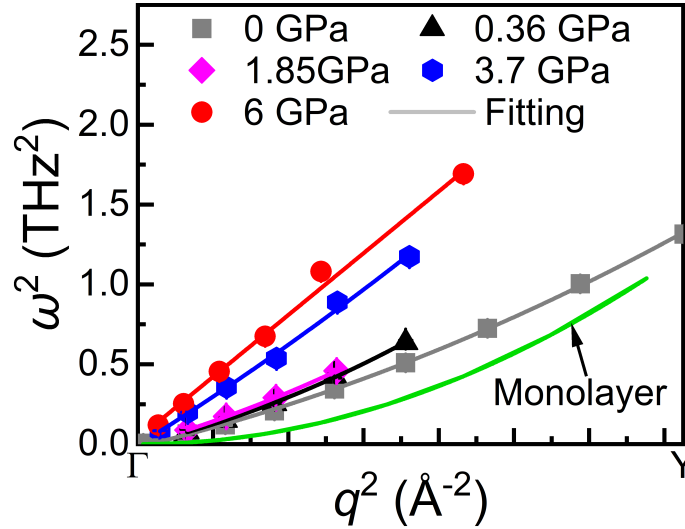


Figure 4.24: Fitted ZA mode of layered PdSe₂ by equation (4.7) at each pressure.

the IXS data and the elastic constants are shown in Tables 4.4-4.6 and plotted in Figure 4.25. C_{22} is associated with the compression vibration along b-axis, corresponding to LA mode along $\Gamma-Y$ and the change of the lattice parameter b , while C_{66} is associated with

the shear vibration along the in-plane direction, corresponding to the change of in-plane lattice parameters a and b . Below 6 GPa, C_{22} and C_{66} both show linear relation with pressure and increase by 50% near the phase transition; at 6 GPa, C_{22} and C_{66} both drop down to a lower value than that at ambient pressure. Such behavior is mainly attributed to the much larger in-plane lattice parameters in cubic structure. C_{33} is associated with the compression vibration along c -axis, corresponding to the LA mode along $\Gamma-Z$ and the change of the lattice parameter c . It is a direct evaluation of the change of vdW interactions between layers. Due to the beam scattering limitation and the ambiguous resolution to distinguish the extremely low energy of the LA mode along $\Gamma-Z$, we only obtain C_{33} under the ambient pressure and 6 GPa. As shown in Figure 4.25 (c), C_{33} is much smaller than C_{22} under ambient pressure due to the weak vdW force between layers. With increasing pressure, C_{33} increases dramatically and the value in cubic structure (equivalent to C_{22}) is 6 times higher than that in orthorhombic structure, indicating the continuous increase of the interlayer force.

C_{44} represents the shear vibration where the atoms vibrate along c direction and vibrational wave propagates along $\Gamma-Y$, corresponding to the ZA mode along $\Gamma-Y$ and the change of the lattice parameters b and c . C_{44} shows the lowest value among the elastic constants because of the interlayer shear vibration affected by the weak vdW force, as shown in Figure 4.25 (c). With the decreasing layer distance and the increasing ratio of b/c , the shear stress will increase significantly and lead to a linear relationship with pressure (Figure 4.25(d)). At 6 GPa, C_{44} (equivalent to C_{66}) shows seven times higher than that at ambient pressure. Due to the bulk single crystal of PdSe₂ used in this work where the vdW force is

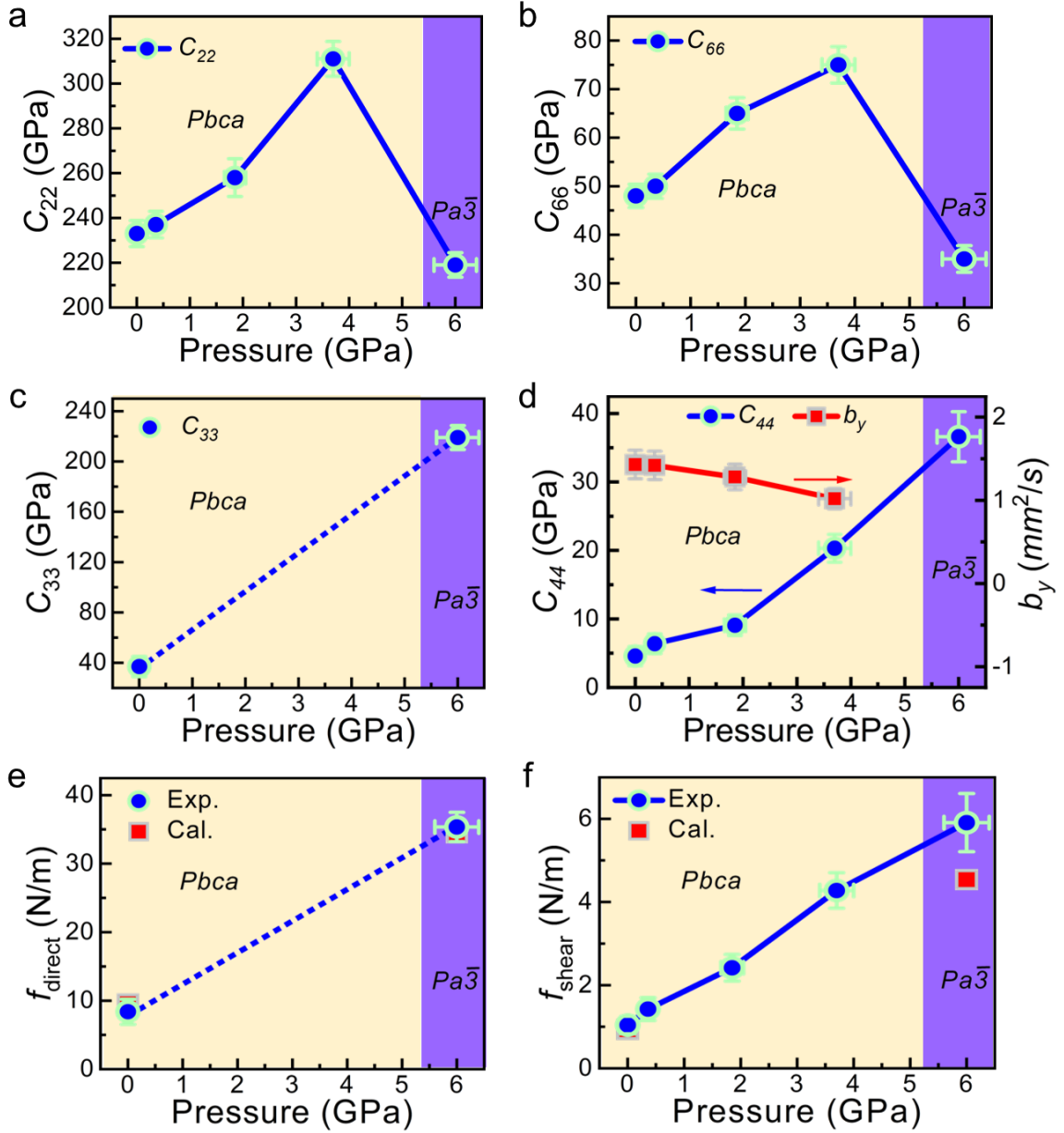


Figure 4.25: Pressure-dependent elastic constants of PdSe₂. a-d are the results of C₂₂, C₆₆, C₃₃, and C₄₄ and b_y, respectively. e and f are the interlayer compression (f_{direct}) and shear (f_{shear}) force constants, respectively. Dashed lines in (c) and (e) indicate the trend with pressure. Error bars are the fitting uncertainty. Shadows represent the different structures as described in previous figures.

Table 4.7: Pressure-dependent layer spacing of PdSe₂.

	Ambient Pressure	0.36 GPa	1.85 GPa	3.7 GPa	6 GPa
Layer spacing	2.265 Å	2.248 Å	2.217 Å	2.202 Å	1.614 Å

stronger than that in monolayer materials, b_y is 1.43 mm²/s at ambient pressure and is five times higher than that of single layer graphene (0.313 mm²/s). [107] With the pressure increased, during the bending on PdSe₂, the intralayer tension or compression and interlayer shear behaviors will both emerge and compete with each other. b_y decreases slightly with increasing pressure, resulting from the increasing shear effect between layers. [142] Compared with C_{22} and C_{66} , the interlayer related C_{33} and C_{44} increases significantly faster with pressure (C_{22} and C_{66} increase by about 50% near the phase transition, while C_{33} and C_{44} increase by 6 and 8 times, respectively.).

The interlayer compression (f_{direct}) and shear (f_{shear}) force constants are utilized to evaluate the interlayer interactions with the layer spacing (c), expressed as: $f_{direct} = c \cdot C_{33}$ and $f_{shear} = c \cdot C_{44}$ [144]. In Figures 4.25 (e) and (f), our first-principles calculations show good agreement with the experiments. The layer spacing decreases gradually with increasing pressure, shown in Table 4.7. f_{direct} changes from around 10 N/m to around 35 N/m before and after phase transition, increased by 3.5 times, while f_{shear} shows a linear relation with pressure, which changes from 1 N/m to 6 N/m, increased by 6 times. These behaviors are mainly due to the enhancement of vdW force between layers, and provide an effective reflection on the evolution of vdW interactions with the layer distance.

4.3.4 Conclusion

In this work, the vdW interactions of 2D-layered PdSe₂ were studied by the combination of high-pressure IXS and first-principles calculations. The pressure-induced phase transition was confirmed and the pressure-dependent acoustic phonon dispersions, especially the ZA mode, along Γ -Y direction were measured. The TA and LA modes stiffen with the increasing pressure below 6 GPa and drop down at 6 GPa, and the ZA mode keeps stiffening as the pressure increases up to 6 GPa. The lattice structure transfers from the orthorhombic to cubic and the interlayer vdW force may disappear from 3.7 to 6 GPa. Below 6 GPa, C_{22} , C_{33} , C_{44} and C_{66} increase linearly with increasing pressure. C_{11} decreases with increasing pressure due to the enhancement of the interlayer shear effect when the competition between the intralayer tension or compression with the interlayer shear effect. The interlayer compression and shear force constants, f_{direct} and f_{shear} , increase with increasing pressure, indicating the enhancement of the interlayer vdW interactions.

Our experimental results show that with the change of pressure, f_{direct} and f_{shear} reflect the evolution of interlayer vdW interactions with pressure. Our work confirmed that the high-pressure IXS measurement is effective to characterize the interlayer vdW interaction. It should be noted that the sample need to be loaded in a special orientation to satisfy the required scattering geometry of high-pressure IXS measurement to directly measure the interlayer vdW interactions. In addition, due to the weak interaction between layers, the acoustic phonons along Γ -Z are localized in the low energy region, a spectrometer with higher resolution is thus needed to distinguish these phonon modes. However, although the sample loading and the instrument setup are still challenging, with the development of

experimental technology, high-pressure IXS will be more effective to characterize the vdW interaction. Our work is not only expected to measure other 2D-materials, but also paves a new path to characterize the vdW interactions.

4.4 Anomalous phonon softening in Fe_3GeTe_2

Raman scattering was performed on Fe_3GeTe_2 at temperatures from 8 to 300 K and under pressures from the ambient pressure to 9.43 GPa. Temperature-dependent and pressure-dependent Raman spectra were reported. Pressure-dependent density functional theory and phonon calculations were conducted and used to assign the observed vibrational modes. The calculations suggest a synergistic interplay of FM/AFM competition, pressure dependence of spin exchange interactions, and spin-orbit coupling effect, resulting in strong spin-phonon coupling and anharmonic phonon dynamics.

4.4.1 Introduction

The intensive research on magnetic thin films has been driven by the rapid development of nanoelectronic and spintronic devices. [43, 155, 57] In two-dimensional (2D) materials, according to the conventional Mermin–Wagner theorem, [171] thermal fluctuations could strongly suppress the magnetic order of materials. However, the discovery of long-range ferromagnetic order in $\text{Cr}_2\text{Ge}_2\text{Te}_6$ [50] and CrI_3 [59] monolayers breaks the conventional theorem. [100] This breakthrough promotes tremendous effort in exploring the potential applications of 2D magnetic materials in magnetoelectrics, electrical control of magnetism, and magnetic tunnel junction. [20, 72, 58] Fe_3GeTe_2 (FGT), a valuable member of 2D layered magnetic materials, has attracted special interests recently due to its rare metallic itinerant ferromagnetism with high Curie temperature (~ 230 K) [41, 5] and novel physical properties, including anomalous hall effect, Kondo effect, and giant tunneling magnetoresistance. [68, 167, 34]

FGT crystallizes in a hexagonal structure with space group $P63/mmc$ (No.194), as shown in Figure 4.26. The unit cell has two layers that are bonded by interlayer van der Waals (vdW) interactions. Each layer comprises five covalently bonded atomic planes. The planar $\text{Fe}^{\text{II}}\text{Ge}$ is sandwiched by two planes of Fe^{I} atoms, and the triple planes are then sandwiched by two layers of Te atoms. The Fe^{I} and Fe^{II} atoms in each layer contribute to both the itinerant electrons and local ferromagnetic moments, which play significant roles in the magnetic spin order transition with pressure and temperature dependence. [144, 170] The reported first-principles calculation has predicted that spin ordering could affect lattice dynamics and reveals notable spin-phonon interactions in FGT. [75] However, pressure- and temperature-dependent lattice vibrations and spin-phonon interactions have not been reported experimentally.

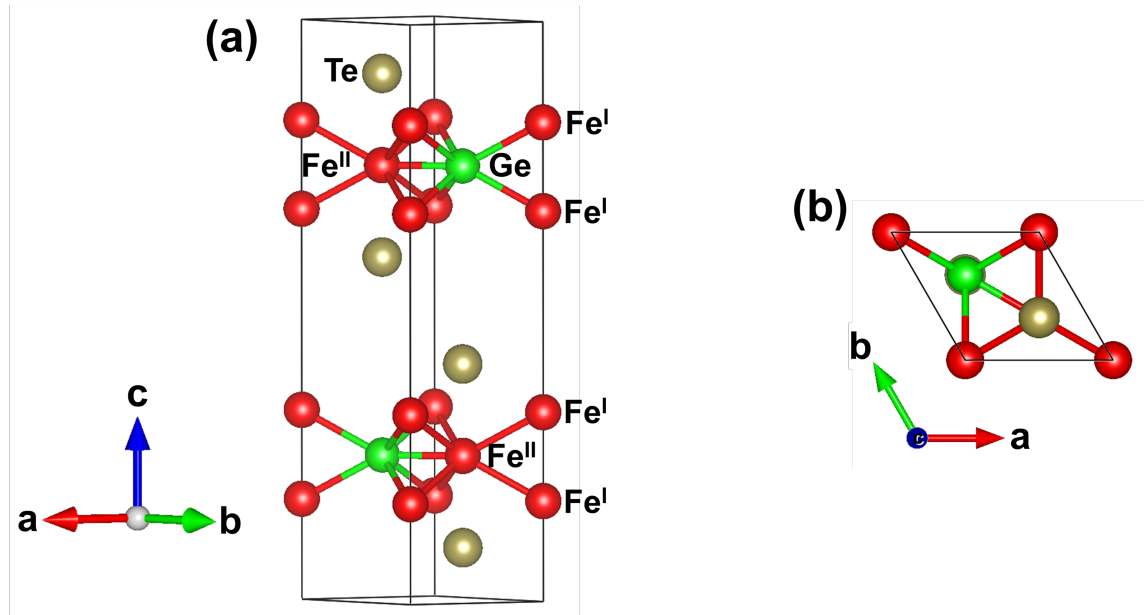


Figure 4.26: a) Side and (b) top view of hexagonal lattice crystal structure of Fe_3GeTe_2 . The red, green, and tan spheres represent the Fe, Ge, and Te atoms, respectively.

Raman spectroscopy is a powerful technique for probing the lattice vibrations in a crystal. Previous studies have reported an anomalous pressure-induced phonon softening behavior [154] and a temperature-driven strong spin-phonon coupling in FGT [38] through Raman studies. However, they did not obtain information about the temperature and pressure dependence simultaneously. The combined effects of temperature and pressure on lattice dynamics may provide information that is not available through only one of them.

In this work, we conducted the pressure-dependent (PD) Raman measurement on FGT at room temperature. In addition, we also performed the combined pressure- and temperature- dependent (PTD) measurements. Two Raman active modes (E_{2g}^2 and A_{1g}^1) were observed. The two types of measurements show that increasing pressure softens the E_{2g}^2 mode anomalously and the decreasing temperature suppresses softening moderately. Temperature-dependent (TD) results were extracted from the two. The extracted TD phonon frequency is much higher than the reported direct measurement. Our first-principles calculations predict the two Raman active modes, but fail in explaining their pressure dependence with a simple magnetic model. These results suggest strong phonon anharmonicity of these two modes, especially E_{2g}^2 . This might be attributed to the strong spin-phonon interactions. Our work provides insightful information for studying the strain effect and thermal properties of FGT for its applications in nanoelectronic and spintronic devices.

4.4.2 Methods

Experimental method: The FGT samples were prepared by solid-state reaction of elements at 800 °C for 5 days. After mixing the elements Fe, Ge, and Te in their

stoichiometric molar ratio, the mixture was pressed into a pellet, sealed in a quartz glass ampule under vacuum, and loaded into the furnace for reaction. [153] The phase purity and crystallinity of the sample were determined by powder X-ray diffraction using a Rigaku Miniflex diffractometer. The excitation source for the Raman spectrometer was 532 nm. The laser power was set at 30 mW to minimize sample damage. An ultrasteep long-pass edge filter (ODabs > 6) was used to block the laser line, and a spectrometer (PI Acton Series 500 mm) was used for spectral imaging on a thermoelectrically cooled 2D CCD camera (PI PIXIS 400B). An Almax plate diamond anvil cell (DAC) with tungsten carbide seats was used for high-pressure environments inside a closed-cycle cryostat. The culet size of the diamonds is 250 μm . A stainless steel gasket with a 100 μm hole was used. Silicone oil was used as the pressure medium in the PD experiment and sodium chloride was used for the PTD experiment. At lower temperatures, thermal contraction of the DAC and gasket shrinks the gasket hole and increases pressure. Therefore, temperature and pressure changes are correlated in the PTD experiments. The PD measurement was conducted at room temperature.

Computational method: To investigate the phonon dynamics of Fe_3GeTe_2 , non-spin and spin-polarized density functional theory (DFT) calculations and phonon calculations were performed. Electronic structure calculations were performed using the projector augmented wave method of Blöchl [17, 77] coded in the Vienna ab initio simulation package (VASP). [76] All VASP calculations employed the generalized gradient approximation (GGA) with exchange and correlation treated by the Perdew-Burke-Enzerhoff functional. [112] The cutoff energy for the plane wave calculations was set to 500 eV and the

Brillouin zone integrations were carried out using Γ -centered $11 \times 11 \times 3$ and $4 \times 4 \times 2$ k-point mesh for a unit cell and $2 \times 2 \times 1$ supercell, respectively. To study the pressure dependence of the phonon vibrations, structure optimization was performed under external pressures of 1, 3, 5, and 7 GPa and followed by phonon calculations using the Phonopy software. [137] The convergence threshold for structural relaxation was set to be 0.01 eV/Å in force. GGA+SOC calculations were employed to examine the spin-orbit coupling (SOC) effect. VASP total energies of spin in the ab-plane ($E_{SOC}(\parallel a)$) and parallel to the c-axis ($E_{SOC}(\parallel c)$) for each compound were calculated. The magnetocrystalline anisotropy energy was then obtained using the relation $\Delta E_{SOC} = E_{SOC}(\parallel a) - E_{SOC}(\parallel c)$. For the experimental structure and four fully relaxed structures under external pressure, phonon calculations were carried out using the finite difference method implemented in the Phonopy software [137] to obtain the Raman peak energies at the Γ point. Phonon calculations were applied to non-spin polarized state, the ferromagnetic state (FM interlayer interaction), the antiferromagnetic state (AFM interlayer interaction), and the antiferromagnetic state with spin-orbit coupling for each structure using $2 \times 2 \times 1$ supercell. To study the effect of pressure on spin interactions in Fe_3GeTe_2 , the effective Fe-Fe exchange parameters in the experimentally observed structure and the relaxed structure under 7 GPa external pressure were evaluated using the spin polarized, relativistic Korringa-Kohn-Rostoker (SPRKKR) package [39] with GGA-PBE as the exchange and correlation corrections and 500 k-points in the Brillouin zone.

4.4.3 Results

Pressure-dependent (PD) Raman spectra

Figure 4.27 (a) shows the Raman spectra of FGT in the frequency range of 80 200 cm^{-1} from ambient pressure to 9.52 GPa at 300 K. Bulk FGT has 12 atoms per unit cell and 36 phonon modes. [75] The two observed Raman active modes E_{2g}^2 and A_{1g}^1 are at 122.7 and 139.8 cm^{-1} at room temperature under ambient pressure, similar to the reported results. [154, 38, 101] Our spin-polarized DFT calculation for the antiferromagnetic state predicts the phonon frequencies of E_{2g}^2 and A_{1g}^1 modes, respectively, at 115.7 and 126.6 cm^{-1} , showing decent agreement with the measurement. As shown in Figure 4.27 (b), A_{1g}^1 mode stiffens slightly with increasing pressure, but E_{2g}^2 mode softens by 21 cm^{-1} monotonically from ambient pressure to 9.52 GPa at room temperature. As for the pressure dependence of the phonon linewidth of these two modes, Figure 4.27 (c) shows an obvious broadening with increasing pressure.

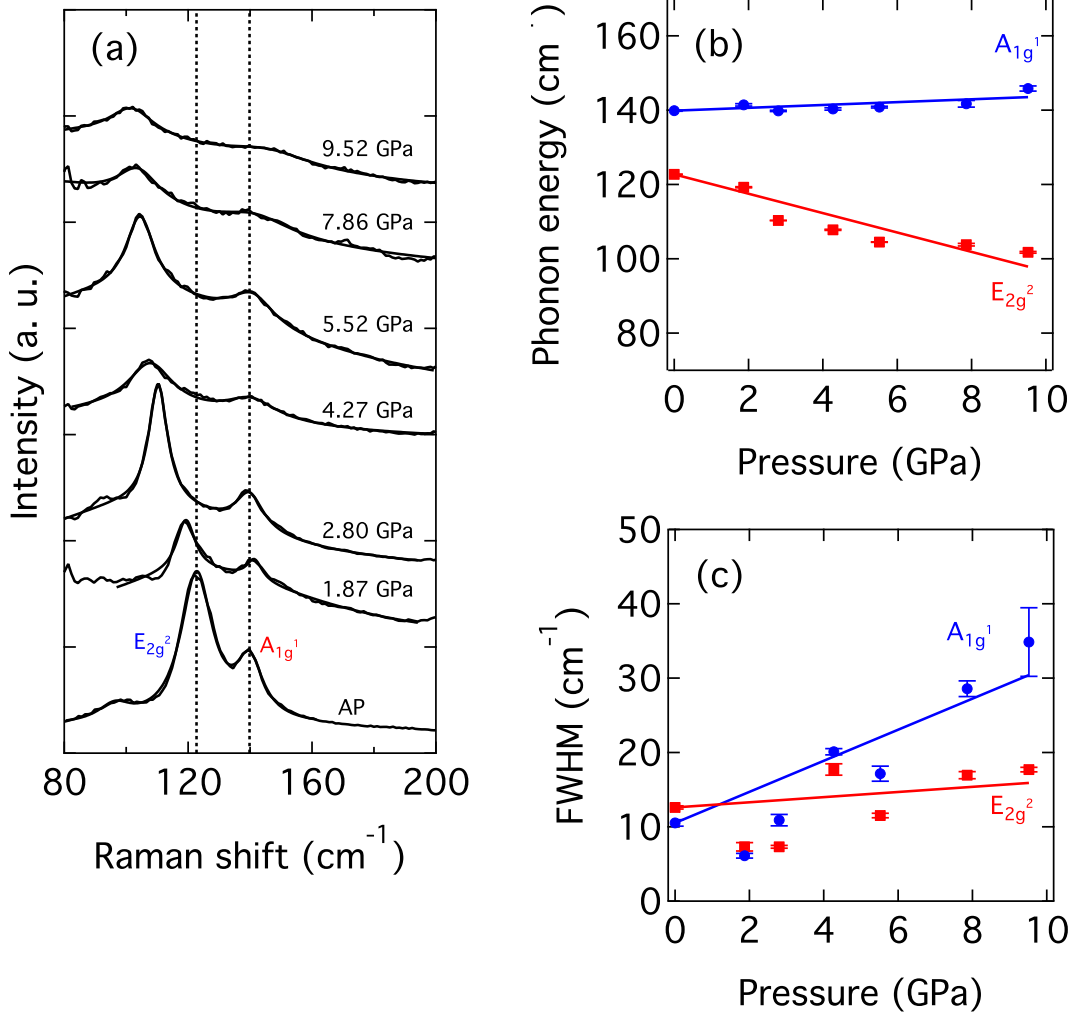


Figure 4.27: Pressure-dependent (PD) Raman spectra at 300 K. (a) Raman spectra from ambient pressure to 9.52 GPa, (b) Pressure dependence of phonon frequency, and (c) pressure dependence of phonon linewidth. The phonon peaks are fitted by Lorentzian function. FWHM stands for the Full Width at Half Maximum. The lines in (b) and (c) are linear fits.

Figure 4.28 shows that E_{2g}^2 mode involves the in-plane atomic vibrations and A_{1g}^1 mode is related to the out-of-plane vibrations of Te, Fe, and/or Ge atoms. Increasing pressure usually decreases the bond lengths and unit cell volume, [35] leading to larger

interatomic force constants and higher vibrational frequency. However, our results reveal a pressure-induced softening of E_{2g}^2 mode. To better understand the abnormal softening, quasi-harmonic approximation (QHA) and density functional theory calculations were employed and the results are analyzed in Discussion.

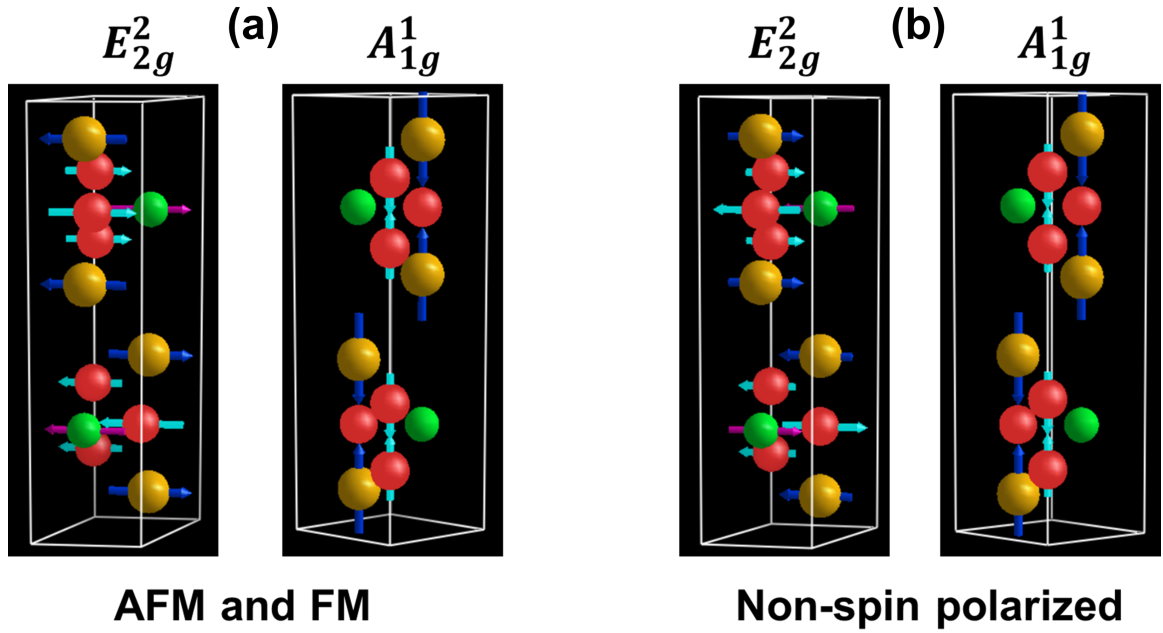


Figure 4.28: Schematic animation of E_{2g}^2 and A_{1g}^1 modes from (a) spin-polarized and (b) non-spin polarized calculations. The red, green, and tan spheres represent the Fe, Ge, and Te atoms, respectively. The arrows represent phonon eigenvectors.

Pressure- and temperature- dependent (PTD) Raman spectra

The PTD phonon frequencies and linewidths of E_{2g}^2 and A_{1g}^1 modes are shown in Figure 4.29 and Figure 4.30. Figure 4.29 (a) shows Raman spectra of FGT at temperatures from 8 to 300 K and pressures from 9.43 GPa to ambient pressure. Our PTD data points cross the phase transition boundary near 6.3 GPa (Figure 4.30 (a)). The PTD phonon

frequencies of the two modes are higher than those of the PD data, as shown in Figure 4.29 (b), suggesting that the decrease in temperature suppresses the E_{2g}^2 softening and enhances the A_{1g}^1 stiffening. The PTD phonon linewidths are shown in Figure 4.30 (b). The phonon linewidth of A_{1g}^1 mode increases monotonically, but for E_{2g}^2 mode, its phonon linewidth decreases cross the phase transition (near 160 K and 6.3 GPa). To quantify the temperature effects on the phonon frequencies, we assume that the PTD phonon shifts are a linear combination of the temperature contribution and the pressure contribution. In this way, the temperature induced shift $\Delta\omega_{AP,T}$ could be calculated based on the following equations:

$$\omega_{P,T} = \omega_{AP,300K} + \Delta\omega_{P,300K} + \Delta\omega_{AP,T}, \quad (4.8)$$

$$\omega_{AP,T} = \omega_{AP,300K} + \Delta\omega_{AP,T}, \quad (4.9)$$

$$\omega_{P,300K} = \omega_{AP,300K} + \Delta\omega_{P,300K}, \quad (4.10)$$

where $\omega_{P,T}$ represents the PTD phonon frequency. $\omega_{AP,300K}$ is our measured phonon frequency at 300 K and ambient pressure. $\omega_{AP,T}$ represents the TD phonon frequency. $\Delta\omega_{AP,T}$ represents the temperature induced frequency shift under ambient pressure. $\omega_{P,300K}$ represents our measured PD phonon frequency. $\Delta\omega_{P,300K}$ represents the pressure-induced frequency shift.

After subtracting the $\Delta\omega_{P,300K}$ from equation (4.8), $\omega_{AP,T}$ of the two modes are obtained and shown in Figure 4.29 (c). Like the behavior of pressure dependence, the effect of temperature on A_{1g}^1 mode is much weaker than that on E_{2g}^2 . A_{1g}^1 mode stiffens moderately by 4.4 cm^{-1} from 300 to 8 K, while E_{2g}^2 mode stiffens by 10.6 cm^{-1} in the same temperature range. For A_{1g}^1 mode, both the increasing pressure and the descending temperature could

lead to the phonon stiffening. Therefore, the PTD phonon frequency is higher than the PD one. For E_{2g}^2 mode, the increasing pressure softens the phonon frequency, but decreasing temperature results in stiffening. The reported TD results under ambient pressure show a slight stiffening from 300 to 8 K, [28] which is much weaker than our extracted results. This discrepancy indicates that the effect of decreasing temperature will be enhanced and could compensate for pressure-induced phonon softening. The discrepancy also suggests that the linear subtraction in equation (4.8) could not quantify the effect of temperature and pressure on the phonon frequency of E_{2g}^2 mode. Considering higher-order effects by simultaneous pressure and temperature is needed to explain the PTD phonon frequency.

4.4.4 Discussion

Quasi-harmonic approximation (QHA) assumes that the phonon frequency is volume-dependent and that the phonon mode remains harmonic at each volume. The Grüneisen parameter provides the connections between phonon frequency and volume change. The isothermal mode Grüneisen parameter can be expressed as: $\gamma_{iT} = -(\frac{d \ln(\omega_i)}{d \ln(V_i)})_T = \frac{B}{\omega_i} (\frac{d\omega_i}{dP})_T$. [21] ω_i is the phonon frequency of i th phonon mode, B is the bulk modulus, which is calculated according to the PD XRD measurement. [38] Based on our PD data, the γ_T of E_{2g}^2 and A_{1g}^1 are -0.88 and 0.11 respectively. The negative value of E_{2g}^2 mode suggests significant phonon anharmonicity. Furthermore, with increasing pressure, the broadening phonon linewidth in Figure 4.27 (c) reveals a shorter phonon lifetime and higher phonon scattering rates, which also suggest the anharmonicity of this mode. On the other hand, our PTD results indicate that the decreasing temperature could suppress the E_{2g}^2 softening with increasing pressure.

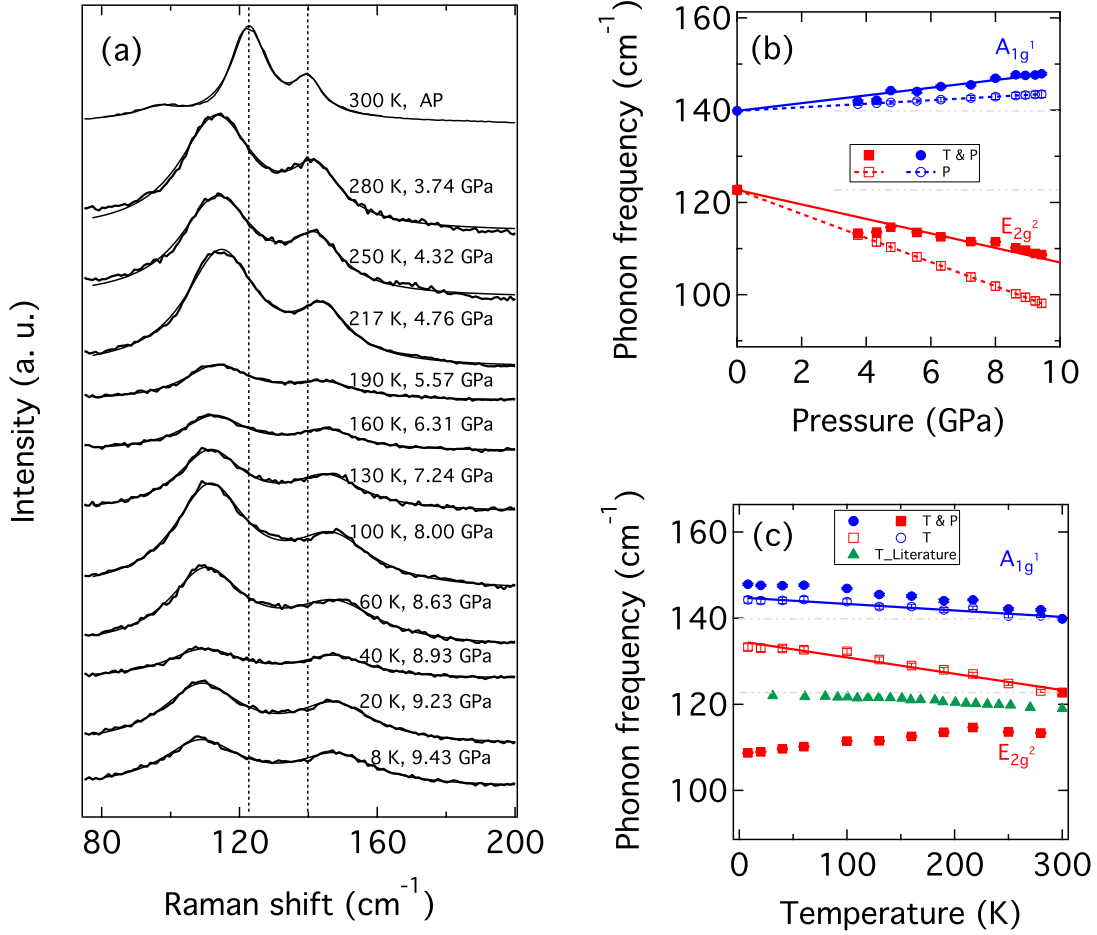


Figure 4.29: Pressure and temperature-dependent (PTD) Raman spectra. (a) Raman spectra of FGT at temperatures from 8 to 300 K and under pressures from 9.43 GPa to ambient pressure. (b) Comparison between PD data and PTD data. The solid red squares and blue circles represent the PTD E_{2g}^2 and A_{1g}^1 , respectively. The hollow red squares and blue circles represent the PD E_{2g}^2 and A_{1g}^1 , calculated from the fitted pressure dependence. (c) Extracted temperature-dependent (TD) phonon frequency. The solid red squares and blue circles represent the PTD E_{2g}^2 and A_{1g}^1 , respectively. The hollow red squares and blue circles represent the extracted TD E_{2g}^2 and A_{1g}^1 , respectively. The green triangles represent the TD E_{2g}^2 obtained from the literature. [38]

The deep of phonon linewidth near phase transition in Figure 4.30 (b) also suggests that the phonon scattering rates are suppressed with increasing pressure and decreasing temperature. In Figure 4.27 (c), we find that increasing pressure only slightly broadens the

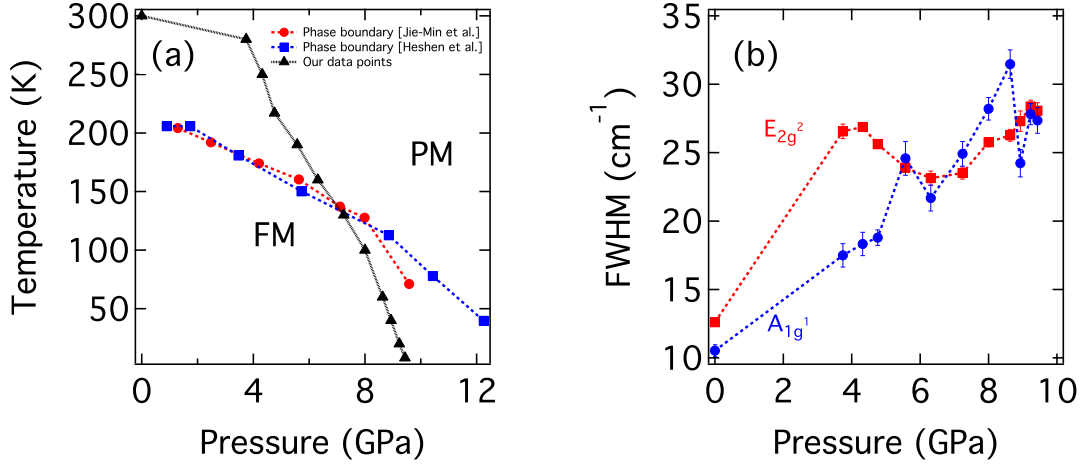


Figure 4.30: Magnetic phase transition and spin-phonon interactions. (a) Pressure-dependent phase diagram. PM and FM represent paramagnetic and ferromagnetic, respectively. The blue square dashed line represents the phase boundary from Heshen et al. [144]. The red circle dashed line represents the phase boundary from Jie-Min et al. [154]. The black triangle solid line represents our measured data points. (b) Phonon linewidth of the two measured modes.

phonon linewidth of the E_{2g}^2 mode. Therefore, we can infer that the temperature effect is opposite and plays a more important role in suppressing the phonon scattering rates below the phase transition.

To understand pressure-induced abnormal softening and anharmonic lattice dynamics in FGT, density functional theory and phonon calculations were applied to study the magnetic properties and Raman frequencies of the experimental structure at ambient pressure and the relaxed structures at external pressure of 1, 3, 5, and 7 GPa.

Although most studies proposed that Fe_3GeTe_2 has an interlayer ferromagnetic spin order, [75] it was reported that the ferromagnetic layers of Fe_3GeTe_2 order antiferromagnetically along the c axis below 152 K. [156] To resolve this inconsistency, we examined the interlayer magnetic interactions in FGT by comparing the total energy of two magnetic

states, the ferromagnetic (FM) and antiferromagnetic (AFM) states. Both states contain ferromagnetic intralayer interactions, but ferromagnetic and antiferromagnetic interlayer interactions for the FM and AFM states, respectively. Based on our results in Figure 4.31 (b), the AFM state is lower in energy for all pressures used, indicating that the AFM state is the ground state. However, the FM states are only slightly higher in energy (6-10 meV/Fe) than the AFM states. Therefore, there might be a competition between the FM and AFM ordering between the FGT layers. Additionally, as pressure increases, the lattice parameters (Figure 4.31 (a)) and Fe-Fe distances (Table 4.8) decrease, leading to more Fe-Fe orbital overlaps, and less localized magnetic moments on Fe atoms. As a result, spin exchange interactions become weaker in FGT as the pressure increases. This is supported by the spin exchange parameters calculated from the SPRKKR calculations. Table 4.8 lists the values of eight spin exchange parameters in FGT at ambient pressure and at 7 GPa. The spin exchange interaction between adjacent Fe^I atoms, J_1 , decreases from 86.9 to 45.2 meV. $J_2 - J_6$ and J_8 also decrease dramatically from ambient pressure to 7 GPa. Therefore, external pressure can reduce spin exchange interactions in FGT, which is consistent with the lower Curie temperature at higher pressure demonstrated in Figure 4.30 (a). Moreover, magnetic anisotropy was investigated using spin-orbit coupling calculations. We evaluated the magnetocrystalline anisotropy energy for FGT at external pressure of 0, 1, 3, 5, 7 GPa by comparing the energy of each FGT with spins in the ab-plane ($E_{SOC}(\parallel a)$) and parallel to the c-axis ($E_{SOC}(\parallel c)$), i.e., $\Delta E_{SOC} = E_{SOC}(\parallel a) - E_{SOC}(\parallel c)$. The results, listed in Figure 4.31 (c), demonstrate that spin parallel to the c-axis is lower in energy at all pressures, indicating easy axis anisotropy. As pressure increases, the magnetocrystalline anisotropy

energy becomes smaller, suggesting that the magnetic anisotropy in FGT becomes weaker under pressure.

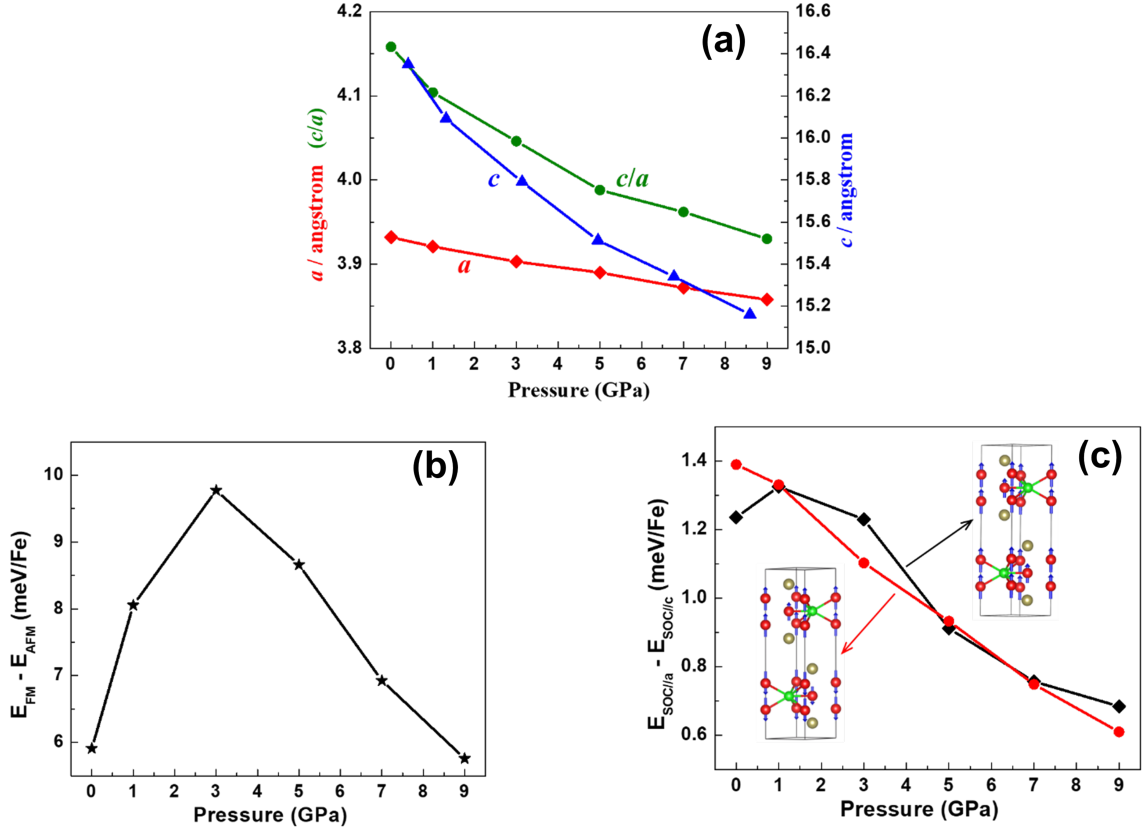
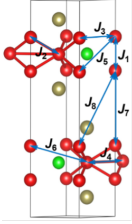


Figure 4.31: (a) Calculated pressure-dependent lattice parameters of Fe_3GeTe_2 . (b) Calculated energy difference between the FM and AFM magnetic states at different pressures. (c) Pressure-dependence of magnetocrystalline anisotropy energy for the FM and AFM states.

In our phonon calculation, we examined the Raman active modes, E_{2g}^2 and A_{1g}^1 , for nonmagnetic, FM state, AFM state without and with spin-orbit coupling. Results are shown in Table 10. For the E_{2g}^2 mode, under external pressures, the calculated frequency increases dramatically from the nonmagnetic state to the FM state. In addition, the AFM state is $\sim 10 \text{ cm}^{-1}$ higher in frequency than the FM state. Therefore, magnetic ordering has a high

Table 4.8: Spin exchange parameters for experimental and 7 GPa structures obtained from SPRKKR calculations.

	Interactions	Spin exchange	# of pairs	Distance (Å)		J (meV)	
				Ambient Pressure	7 GPa	Ambient Pressure	7 GPa
	Fe ^I - Fe ^I	J_1	2	2.558	2.463	86.9	45.2
		J_3	12	4.005	3.872	-9.33	-6.34
		J_5	12	4.752	4.588	-4.50	-1.40
		J_7	2	5.630	5.208	1.03	-2.63
		J_8	12	6.909	6.489	-2.21	-1.18
Fe ^I - Fe ^{II}	J_2	12	2.642	2.552	22.3	16.4	
	J_6	12	4.798	4.639	3.73	3.66	
Fe ^{II} - Fe ^{II}	J_4	6	4.005	3.872	-4.00	-2.06	

impact on Raman frequency, suggesting strong spin-phonon coupling in the system. [75] AFM state with spin-orbit coupling has a slightly lower Raman frequency than the AFM state, so spin-orbit coupling also has some impact on the frequency of the E_{2g}^2 mode. As discussed in the previous paragraph, increased pressure could reduce the spin exchange interactions and spin-orbit coupling effect in FGT, hence reducing the spin-phonon coupling in the system, resulting in an overall phonon softening. In other words, our calculations examined ideal FM and AFM states, and our results demonstrated E_{2g}^2 mode stiffens as pressure increases. However, the real spin arrangement in FGT can be paramagnetic above critical temperature and pressure (Figure 4.30 (a)), or in general FM or AFM ordering with different magnetic domains depending on the strength of spin exchange interactions and magnetic anisotropy controlled by temperature and pressure. For example, as pressure increases, spin exchange interactions and spin-orbit coupling effect decrease, while interlayer FM/AFM competition increases. Consequently, the compound will be more magnetically

Table 4.9: Calculated frequencies (cm^{-1}) of Raman active modes under various pressure.

Pressure (GPa)	E_{2g}^2				A_{1g}^1			
	Non-magnetic	FM	AFM	AFM+SOC	Non-magnetic	FM	AFM	AFM+SOC
Ambient Pressure	57.7	114.0	115.7	112.9	109.4	125.2	126.6	127.0
1	68.7	108.7	126.2	122.1	139.8	140.0	141.4	146.7
3	87.3	119.3	128.3	128.1	149.1	144.0	159.7	146.0
5	61.9	123.6	133.4	132.0	152.0	156.0	162.2	126.8
7	75.1	128.8	137.8	136.3	156.6	162.5	156.4	155.6

disordered with weaker spin-phonon coupling and exhibit lower frequency of the E_{2g}^2 Raman mode. Therefore, the interplay of FM/AFM competition, pressure-induced decline of spin exchange interactions and spin-orbit coupling effect, leads to an overall softening of the E_{2g}^2 Raman mode as the pressure increases. For the A_{1g}^1 mode, the frequency change from the non-magnetic state to magnetic states and AFM+SOC state is small, so the impact of spin exchange and spin-orbit coupling is smaller compared to the E_{2g}^2 mode. Consequently, the A_{1g}^1 mode has smaller frequency shift under pressure.

4.4.5 Conclusion

We conducted the pressure-dependent (PD) and pressure- and temperature- dependent (PTD) Raman scattering measurements and performed first-principles pressure-dependent phonon calculations on FGT. We observed the anomalous E_{2g}^2 softening in PD data, but the DFT predicts stiffening for simple FM or AFM states with increasing pressure, indicating a strong phonon anharmonicity and spin-phonon coupling. Using the linear pressure dependence of E_{2g}^2 and A_{1g}^1 modes, we extracted the temperature-induced phonon

frequency shift from PTD data. The obtained temperature effect was stronger than the reported direct results, indicating that the higher-order contribution from simultaneous pressure and temperature effect is non-negligible. Our results suggest that the anomalous phonon softening may be related to spin-phonon interactions and an interplay of FM/AFM competition, spin-orbit coupling and spin exchange interaction weakening under pressure.

Chapter 5

Conclusion

Inelastic scattering techniques have been used to measure chiral phonons in topological semimetal WC, investigate the lattice dynamics in monolayer and bulk WSe₂, quantify the vdW forces in layered PdSe₂, study the anharmonic lattice dynamics in paraterphenyl and observe the anomalous phonon softening in Fe₃GeTe₂. Most of the experiments were performed under extreme conditions, and first-principles phonon calculations were interpreted to provide supportive explanation for our observations.

The work about chiral phonons by IXS was the first attempt in probing phonon chirality directly throughout the full Brillouin zone in materials with broken inversion symmetry. It paves a new avenue in measuring chiral phonons and study the effects of phonon chirality in phonon-phonon/spin interactions for designing phononic devices. It also points out that the present inelastic scattering theory of phonons needs to be revised to consider the role of phonon/photon polarizations. In order to improve the scattering theory, we tested and excluded several models based on the current-current correlation function according to

the atomic motions. More efforts should be paid in developing and verifying the scattering theory by chiral phonons in various systems. In addition to the scattering intensity, it is also worthwhile to study the relation between phonon linewidth and phonon chirality. Such relation is important in finding the selection rules in three-phonon and four-phonon scattering processes, and provide discerning insights in studying the thermal conductivity and thermal hall effect in chiral materials.

By combining temperature-dependent IXS and first-principles calculations, we found a monolayer-like lattice dynamics in bulk WSe₂. This observation indicates that lattice dynamics in bulk WSe₂ hold the characterization of monolayers. Since it is extremely difficult to conduct the full phonon dispersion measurement on monolayer system due to its low X-ray absorption and scattering intensities. The measured acoustic phonons in the bulk system could be used as reference to study the lattice dynamics in monolayer system. With the rapid development in the research and industrial applications of low-dimensional materials, it is of great importance to extend the comprehensive lattice dynamics measurement from bulk system to 2D system or thin films. Even though electron energy loss spectroscopy has been reported to determine phonon dispersion of free-standing graphene, the scattering intensity and resolution still need to be improved. [172] IXS can be the possible solution to this challenge on superlattice and thin films by using longer data acquisition time when the X-ray source become more brilliant in the future. Such breakthrough will open a new window to investigate the physical and chemical properties of low-dimensional materials.

High-pressure lattice dynamics in para-terphenyl, layered PdSe₂ and Fe₃GeTe₂ were obtained by using INS, IXS, and Raman scattering respectively. The selection on

inelastic scattering techniques and DAC for high-pressure studies is purposeful. In paraterphenyl, we aimed at using the lattice dynamics to study the phase transition. It is not required to increase pressure to GPa level at low temperature, the sample is not a single crystal, Raman spectrometer could only observe limited number of phonon modes, thus we use VISION for the measurement. In layered PdSe₂, we aimed at quantifying the vdW interactions by measuring the pressure-dependent acoustic phonon dispersion. It is difficult to have a large PdSe₂ single crystal and find suitable DAC to increase pressure over 5 GPa for INS, so IXS comes to the best solution. In Fe₃GeTe₂, we changed the temperature and pressure simultaneously, the DAC was mounted inside the cryostat, it could only be realized in Raman scattering measurement. High-pressure research on lattice dynamics in monolayer and layered materials, such as graphene and graphite, is becoming increasingly intensive recently. While the quantification of vdW interactions was not reported previously, high-pressure IXS on layered material make it possible and provide a new pathway in probing vdW interactions experimentally. However, this method is rarely reported because it is extremely difficult to prepare the high-quality tiny bulk sample, which also needs to be loaded in specific orientation in the DAC to measure all the phonon branches. It is also interesting to extend the high-pressure IXS for chiral phonon measurements in layered materials, like Tellurium (Te). The various scattering intensity of chiral phonons at each pressure can reveal the evolution of phonon chirality, which help us realize the manipulation on chiral phonons by pressure.

Bibliography

- [1] <https://www.2spi.com/item/4375wse2-ab/>.
- [2] Soft phonon mode coupled with antiferromagnetic order in incipient-ferroelectric Mott insulators $\text{Sr}_{1-x}\text{Ba}_x\text{MnO}_3$, author=Sakai, H and Fujioka, J and Fukuda, T and Bahramy, MS and Okuyama, D and Arita, R and Arima, T and Baron, AQR and Taguchi, Y and Tokura, Y, journal=Physical Review B, volume=86, number=10, pages=104407, year=2012, publisher=APS.
- [3] D Yu Akimov, AV Akindinov, IS Alexandrov, VA Belov, OV Borshchev, AA Burenkov, MV Danilov, AG Kovalenko, Yu N Luponosov, SA Ponomarenko, et al. Development of vuv wavelength shifter for the use with a visible light photodetector in noble gas filled detectors. *Nuclear Instruments and Methods in Physics Research Section A: Accelerators, Spectrometers, Detectors and Associated Equipment*, 695:403–406, 2012.
- [4] A Alatas, AH Said, H Sinn, G Bortel, MY Hu, J Zhao, CA Burns, E Burkel, and EE Alp. Atomic form-factor measurements in the low-momentum transfer region for Li, Be, and Al by inelastic X-ray scattering. *Physical Review B*, 77(6):064301, 2008.
- [5] Mohammed Alghamdi, Mark Lohmann, Junxue Li, Palani R Jothi, Qiming Shao, Mohammed Aldosary, Tang Su, Boniface PT Fokwa, and Jing Shi. Highly efficient spin-orbit torque and switching of layered ferromagnet Fe_3GeTe_2 . *Nano letters*, 19(7):4400–4405, 2019.
- [6] M Angelone, G Battistoni, F Bellini, V Bocci, F Collamati, Erika De Lucia, R Faccini, Fernando Ferroni, S Fiore, M Marafini, et al. Properties of para-terphenyl as a detector for α , β and γ radiation. *IEEE Transactions on Nuclear Science*, 61(3):1483–1487, 2014.
- [7] Sriharsha V Aradhya, Michael Frei, Mark S Hybertsen, and L Venkataraman. Van der Waals interactions at metal/organic interfaces at the single-molecule level. *Nature materials*, 11(10):872–876, 2012.
- [8] Owen Arnold, Jean-Christophe Bilheux, JM Borreguero, Alex Buts, Stuart I Campbell, L Chapon, Mathieu Doucet, N Draper, R Ferraz Leal, MA Gigg, et al. Mantid—data analysis and visualization package for neutron scattering and μ sr experi-

- ments. *Nuclear instruments and methods in physics research section a: accelerators, spectrometers, detectors and associated equipment*, 764:156–166, 2014.
- [9] Bruce J Baer and Eric L Chronister. Pressure induced phase transitions in pentacene doped para-terphenyl probed by changes in the impurity absorption spectrum. *The Journal of chemical physics*, 99(4):3137–3138, 1993.
- [10] Bruce J Baer and Eric L Chronister. Temperature and pressure dependent optical dephasing of pentacene in triclinic and monoclinic p-terphenyl. *The Journal of Physical Chemistry*, 99(19):7324–7329, 1995.
- [11] Luisa Barba, Giuseppe Chita, Gaetano Campi, Lorenza Suber, Elvira Maria Bauer, Augusto Marcelli, and Antonio Bianconi. Anisotropic thermal expansion of p-terphenyl: A self-assembled supramolecular array of poly-p-phenyl nanoribbons. *Journal of Superconductivity and Novel Magnetism*, 31(3):703–710, 2018.
- [12] Alfred QR Baron. Phonons in crystals using inelastic X-ray scattering. *arXiv preprint arXiv:0910.5764*, 2009.
- [13] Alfred QR Baron. Introduction to high-resolution inelastic X-ray scattering. *arXiv preprint arXiv:1504.01098*, 2015.
- [14] JL Baudour, Y Delugeard, and H Cailleau. Transition structurale dans les polyphényles. i. structure cristalline de la phase basse température du p-terphényle à 113 k. *Acta Crystallographica Section B: Structural Crystallography and Crystal Chemistry*, 32(1):150–154, 1976.
- [15] Kristian Berland and Per Hyldgaard. Exchange functional that tests the robustness of the plasmon description of the van der Waals density functional. *Physical Review B*, 89(3):035412, 2014.
- [16] Sandip V Bhatt, MP Deshpande, Vasant Sathe, Rekha Rao, and SH Chaki. Raman spectroscopic investigations on transition-metal dichalcogenides MX_2 (M= Mo, W; X= S, Se) at high pressures and low temperature. *Journal of Raman Spectroscopy*, 45(10):971–979, 2014.
- [17] Peter E Blöchl. Projector augmented-wave method. *Physical review B*, 50(24):17953, 1994.
- [18] Patrice Bordat, Alain Marbeuf, and Ross Brown. Molecular simulation of solid–solid phase transitions. *Molecular Simulation*, 32(12-13):971–984, 2006.
- [19] PJ Brown, AG Fox, EN Maslen, MA O’Keefe, and BTM Willis. International tables for crystallography. *Vol. B, Kluwer Academic Publishers*, 27, 1992.
- [20] Kenneth S Burch, David Mandrus, and Je-Geun Park. Magnetism in two-dimensional van der Waals materials. *Nature*, 563(7729):47–52, 2018.

- [21] Qingan Cai, Michael McIntire, Luke L Daemen, Chen Li, and Eric L Chronister. Pressure- and temperature-dependent inelastic neutron scattering study of the phase transition and phonon lattice dynamics in para-terphenyl. *Physical Chemistry Chemical Physics*, 23(14):8792–8799, 2021.
- [22] H Cailleau, A Girard, JC Messenger, Y Delugeard, and C Vettier. Influence of pressure on structural phase transitions in p-polyphenyls. *Ferroelectrics*, 54(1):257–260, 1984.
- [23] Xiaoyan Cao and Michael Dolg. Relativistic pseudopotentials. In *Relativistic methods for chemists*, pages 215–277. Springer, 2010.
- [24] Hao Chen, Weikang Wu, Jiaojiao Zhu, Shengyuan A Yang, and Lifa Zhang. Propagating chiral phonons in three-dimensional materials. *Nano Letters*, 21(7):3060–3065, 2021.
- [25] Hao Chen, Wei Zhang, Qian Niu, and Lifa Zhang. Chiral phonons in two-dimensional materials. *2D Materials*, 6(1):012002, 2018.
- [26] Shao-Yu Chen, Changxi Zheng, Michael S Fuhrer, and Jun Yan. Helicity-resolved raman scattering of MoS₂, MoSe₂, WS₂, and WSe₂ atomic layers. *Nano letters*, 15(4):2526–2532, 2015.
- [27] Shunda Chen, Aditya Sood, Eric Pop, Kenneth E Goodson, and Davide Donadio. Strongly tunable anisotropic thermal transport in MoS₂ by strain and lithium intercalation: first-principles calculations. *2D Materials*, 6(2):025033, 2019.
- [28] Xiaotong Chen, Xin Lu, Sudipta Dubey, Qiang Yao, Sheng Liu, Xingzhi Wang, Qihua Xiong, Lifa Zhang, and Ajit Srivastava. Entanglement of single-photons and chiral phonons in atomically thin WSe₂. *Nature Physics*, 15(3):221–227, 2019.
- [29] Xin Chen, Lei Wang, Hai-Yu Wang, Xue-Peng Wang, Yang Luo, and Hong-Bo Sun. Electronic structure evolution and exciton energy shifting dynamics in WSe₂: from monolayer to bulk. *Journal of Physics D: Applied Physics*, 54(35):354002, 2021.
- [30] Catalin Chiritescu, David G Cahill, Ngoc Nguyen, David Johnson, Arun Bodapati, Pawel Koblinski, and Paul Zschack. Ultralow thermal conductivity in disordered, layered WSe₂ crystals. *Science*, 315(5810):351–353, 2007.
- [31] Hsun-Jen Chuang, Xuebin Tan, Nirmal Jeevi Ghimire, Meeghage Madusanka Perera, Bhim Chamlagain, Mark Ming-Cheng Cheng, Jiaqiang Yan, David Mandrus, David Tomanek, and Zhixian Zhou. High mobility WSe₂ p- and n-type field-effect transistors contacted by highly doped graphene for low-resistance contacts. *Nano letters*, 14(6):3594–3601, 2014.
- [32] Penghong Ci, Yabin Chen, Jun Kang, Ryuji Suzuki, Hwan Sung Choe, Joonki Suh, Changhyun Ko, Taegyun Park, Ke Shen, Yoshihiro Iwasa, et al. Quantifying van der Waals interactions in layered transition metal dichalcogenides from pressure-enhanced valence band splitting. *Nano letters*, 17(8):4982–4988, 2017.

- [33] Sinisa Coh. Classification of materials with phonon angular momentum and microscopic origin of angular momentum. *arXiv preprint arXiv:1911.05064*, 2019.
- [34] Yujun Deng, Yijun Yu, Yichen Song, Jingzhao Zhang, Nai Zhou Wang, Zeyuan Sun, Yangfan Yi, Yi Zheng Wu, Shiwei Wu, Junyi Zhu, et al. Gate-tunable room-temperature ferromagnetism in two-dimensional Fe_3GeTe_2 . *Nature*, 563(7729):94–99, 2018.
- [35] Shilei Ding, Zhongyu Liang, Jie Yang, Chao Yun, Peijie Zhang, Zefang Li, Mingzhu Xue, Zhou Liu, Guang Tian, Fuyang Liu, et al. Ferromagnetism in two-dimensional Fe_3GeTe_2 ; tunability by hydrostatic pressure. *Physical Review B*, 103(9):094429, 2021.
- [36] Yingchun Ding, Min Chen, and Bing Xiao. Anisotropy in lattice thermal conductivity tensor of bulk hexagonal- MT_2 (M= W, Mo and T= S and Se) by first principles phonon calculations. *RSC advances*, 6(10):7817–7828, 2016.
- [37] Martin T Dove. *Introduction to lattice dynamics*. Number 4. Cambridge university press, 1993.
- [38] Luojun Du, Jian Tang, Yanchong Zhao, Xiaomei Li, Rong Yang, Xuerong Hu, Xueyin Bai, Xiao Wang, Kenji Watanabe, Takashi Taniguchi, et al. Lattice dynamics, phonon chirality, and spin–phonon coupling in 2d itinerant ferromagnet Fe_3GeTe_2 . *Advanced Functional Materials*, 29(48):1904734, 2019.
- [39] Hubert Ebert, Diemo Koedderitzsch, and Jan Minar. Calculating condensed matter properties using the kkr-green’s function method—recent developments and applications. *Reports on Progress in Physics*, 74(9):096501, 2011.
- [40] Moaz A ElGhazali, Pavel G Naumov, Hossein Mirhosseini, Vicky Süß, Lukas Mühler, Walter Schnelle, Claudia Felser, and Sergey A Medvedev. Pressure-induced superconductivity up to 13.1 K in the pyrite phase of palladium diselenide PdSe_2 . *Physical Review B*, 96(6):060509, 2017.
- [41] Zaiyao Fei, Bevin Huang, Paul Malinowski, Wenbo Wang, Tiancheng Song, Joshua Sanchez, Wang Yao, Di Xiao, Xiaoyang Zhu, Andrew F May, et al. Two-dimensional itinerant ferromagnetism in atomically thin Fe_3GeTe_2 . *Nature materials*, 17(9):778–782, 2018.
- [42] James J Flores and Eric L Chronister. Pressure-dependent raman shifts of molecular vibrations in poly (methyl methacrylate) and polycarbonate polymers. *Journal of Raman spectroscopy*, 27(2):149–153, 1996.
- [43] Hiroyasu Fujimori, Shigehiro Ohnuma, Nobukiyo Kobayashi, and Tsuyosi Masumoto. Spintronics in metal–insulator nanogranular magnetic thin films. *Journal of magnetism and magnetic materials*, 304(1):32–35, 2006.
- [44] Brent Fultz. Vibrational thermodynamics of materials. *Progress in Materials Science*, 55(4):247–352, 2010.

- [45] Lei Gao, Guo-Hua Zhong, and Hai-Qing Lin. Structures, electronic properties, and superconductivities of alkaline-earth metal-doped phenanthrene and charge transfer characteristics of metal-doped phenanthrene. *Physical Chemistry Chemical Physics*, 22(41):23847–23855, 2020.
- [46] Thanasis Georgiou, Rashid Jalil, Branson D Belle, Liam Britnell, Roman V Gorbachev, Sergey V Morozov, Yong-Jin Kim, Ali Gholinia, Sarah J Haigh, Oleg Makarovskiy, et al. Vertical field-effect transistor based on graphene–WS₂ heterostructures for flexible and transparent electronics. *Nature nanotechnology*, 8(2):100–103, 2013.
- [47] A Girard, H Cailleau, Y Marqueton, and C Ecolivet. Raman scattering study of the order—disorder phase transition in para-terphenyl. *Chemical Physics Letters*, 54(3):479–482, 1978.
- [48] Feliciano Giustino. *Materials modelling using density functional theory: properties and predictions*. Oxford University Press, 2014.
- [49] JA Goldstone, J Eckert, AD Taylor, and EJ Wood. Beryllium-beryllium oxide filter difference spectrometer. *Los Alamos National Lab., NM (USA)*, 1982.
- [50] Cheng Gong, Lin Li, Zhenglu Li, Huiwen Ji, Alex Stern, Yang Xia, Ting Cao, Wei Bao, Chenzhe Wang, Yuan Wang, et al. Discovery of intrinsic ferromagnetism in two-dimensional van der Waals crystals. *Nature*, 546(7657):265–269, 2017.
- [51] DJ Goossens and MJ Gutmann. Revealing how interactions lead to ordering in para-terphenyl. *Physical Review Letters*, 102(1):015505, 2009.
- [52] EA Goremychkin, DG Hinks, AI Kolesnikov, and R Osborn. Phonon density of states in MgB₂. *Physical Review Letters*, 87(01), 2003.
- [53] G Grissonnanche, S Thériault, A Gourgout, M-E Boulanger, E Lefrançois, A Ataei, F Laliberté, M Dion, J-S Zhou, S Pyon, et al. Chiral phonons in the pseudogap phase of cuprates. *Nature Physics*, 16(11):1108–1111, 2020.
- [54] San-Dong Guo and Peng Chen. Soft phonon modes driven huge difference on lattice thermal conductivity between topological semimetal WC and WN. *The Journal of chemical physics*, 148(14):144706, 2018.
- [55] Masato Hamada, Emi Minamitani, Motoaki Hirayama, and Shuichi Murakami. Phonon angular momentum induced by the temperature gradient. *Physical review letters*, 121(17):175301, 2018.
- [56] Fuxiang Han. *A modern course in the quantum theory of solids*. World Scientific, 2013.
- [57] Frances Hellman, Axel Hoffmann, Yaroslav Tserkovnyak, Geoffrey SD Beach, Eric E Fullerton, Chris Leighton, Allan H MacDonald, Daniel C Ralph, Dario A Arena, Hermann A Dürr, et al. Interface-induced phenomena in magnetism. *Reviews of modern physics*, 89(2):025006, 2017.

- [58] Bevin Huang, Genevieve Clark, Dahlia R Klein, David MacNeill, Efrén Navarro-Moratalla, Kyle L Seyler, Nathan Wilson, Michael A McGuire, David H Cobden, Di Xiao, et al. Electrical control of 2D magnetism in bilayer CrI_3 . *Nature nanotechnology*, 13(7):544–548, 2018.
- [59] Bevin Huang, Genevieve Clark, Efrén Navarro-Moratalla, Dahlia R Klein, Ran Cheng, Kyle L Seyler, Ding Zhong, Emma Schmidgall, Michael A McGuire, David H Cobden, et al. Layer-dependent ferromagnetism in a van der Waals crystal down to the monolayer limit. *Nature*, 546(7657):270–273, 2017.
- [60] Chunming Huang, Sanfeng Wu, Ana M Sanchez, Jonathan JP Peters, Richard Bealand, Jason S Ross, Pasqual Rivera, Wang Yao, David H Cobden, and Xiaodong Xu. Lateral heterojunctions within monolayer MoSe_2 – WSe_2 semiconductors. *Nature materials*, 13(12):1096–1101, 2014.
- [61] Liang-Feng Huang and Zhi Zeng. Roles of mass, structure, and bond strength in the phonon properties and lattice anharmonicity of single-layer Mo and W dichalcogenides. *The Journal of Physical Chemistry C*, 119(32):18779–18789, 2015.
- [62] Wen Huang, Xin Luo, Chee Kwan Gan, Su Ying Quek, and Gengchiao Liang. Theoretical study of thermoelectric properties of few-layer MoS_2 and WSe_2 . *Physical Chemistry Chemical Physics*, 16(22):10866–10874, 2014.
- [63] Adam J. Jackson. ascii-phonons, July 2018.
- [64] Jin-Wu Jiang and Jian-Sheng Wang. A universal exponential factor in the dimensional crossover from graphene to graphite. *Journal of Applied Physics*, 108(12):124311, 2010.
- [65] Puqing Jiang, Xin Qian, Xiaokun Gu, and Ronggui Yang. Probing anisotropic thermal conductivity of transition metal dichalcogenides MX_2 (M= Mo, W and X= S, Se) using time-domain thermoreflectance. *Advanced Materials*, 29(36):1701068, 2017.
- [66] Shigeki Kawai, Adam S Foster, Torbjörn Björkman, Sylwia Nowakowska, Jonas Björk, Filippo Federici Canova, Lutz H Gade, Thomas A Jung, and Ernst Meyer. Van der Waals interactions and the limits of isolated atom models at interfaces. *Nature communications*, 7(1):1–7, 2016.
- [67] P Kepple and Hans R Griem. Improved stark profile calculations for the hydrogen lines $\text{H}\alpha$, $\text{H}\beta$, $\text{H}\gamma$, and $\text{H}\delta$. *Physical Review*, 173(1):317, 1968.
- [68] Kyoo Kim, Junho Seo, Eunwoo Lee, K-T Ko, BS Kim, Bo Gyu Jang, Jong Mok Ok, Jinwon Lee, Youn Jung Jo, Woun Kang, et al. Large anomalous Hall current induced by topological nodal lines in a ferromagnetic van der Waals semimetal. *Nature materials*, 17(9):794–799, 2018.
- [69] Shi En Kim, Fauzia Mujid, Akash Rai, Fredrik Eriksson, Joonki Suh, Preeti Poddar, Ariana Ray, Chibeom Park, Erik Fransson, Yu Zhong, et al. Extremely anisotropic van der Waals thermal conductors. *Nature*, 597(7878):660–665, 2021.

- [70] T Kimura and Y Tokura. Layered magnetic manganites. *Annual Review of Materials Research*, 30:451, 2000.
- [71] D Kirin, SL Chaplot, GA Mackenzie, and GS Pawley. The pressure dependence of the low-frequency raman spectra of crystalline biphenyl and p-terphenyl. *Chemical physics letters*, 102(1):105–108, 1983.
- [72] Dahlia R Klein, David MacNeill, Jose L Lado, David Soriano, Efrén Navarro-Moratalla, Kenji Watanabe, Takashi Taniguchi, Soham Manni, Paul Canfield, Joaquín Fernández-Rossier, et al. Probing magnetism in 2D van der Waals crystalline insulators via electron tunneling. *Science*, 360(6394):1218–1222, 2018.
- [73] Jiří Klimeš, David R Bowler, and Angelos Michaelides. Chemical accuracy for the van der Waals density functional. *Journal of Physics: Condensed Matter*, 22(2):022201, 2009.
- [74] Kozo Komatsu and Takeo Nagamiya. Theory of the specific heat of graphite. *Journal of the Physical Society of Japan*, 6(6):438–444, 1951.
- [75] Xiangru Kong, Tom Berlijn, and Liangbo Liang. Thickness and spin dependence of raman modes in magnetic layered Fe_3GeTe_2 . *Advanced Electronic Materials*, 7(7):2001159, 2021.
- [76] Georg Kresse and Jürgen Furthmüller. Efficient iterative schemes for ab initio total-energy calculations using a plane-wave basis set. *Physical review B*, 54(16):11169, 1996.
- [77] Georg Kresse and Daniel Joubert. From ultrasoft pseudopotentials to the projector augmented-wave method. *Physical review B*, 59(3):1758, 1999.
- [78] Kliment I Kugel and Khomskii. The Jahn-Teller effect and magnetism: transition metal compounds.
- [79] S Kumar and U Schwingenschlogl. Thermoelectric response of bulk and monolayer MoSe_2 and WSe_2 . *Chemistry of Materials*, 27(4):1278–1284, 2015.
- [80] S Kummer, F Kulzer, R Kettner, Th Basché, C Tietz, Ch Glowatz, and C Kryschi. Absorption, excitation, and emission spectroscopy of terrylene in p-terphenyl: Bulk measurements and single molecule studies. *The Journal of chemical physics*, 107(19):7673–7684, 1997.
- [81] A Kundu, J Ma, Jesús Carrete, GKH Madsen, and W Li. Anomalously large lattice thermal conductivity in metallic tungsten carbide and its origin in the electronic structure. *Materials Today Physics*, 13:100214, 2020.
- [82] Dattatray J Late, Sharmila N Shirodkar, Umesh V Waghmare, Vinayak P Dravid, and CNR Rao. Thermal expansion, anharmonicity and temperature-dependent raman spectra of single-and few-layer MoS_2 and WSe_2 . *ChemPhysChem*, 15(8):1592–1598, 2014.

- [83] Changgu Lee, Hugen Yan, Louis E Brus, Tony F Heinz, James Hone, and Sunmin Ryu. Anomalous lattice vibrations of single-and few-layer MoS₂. *ACS nano*, 4(5):2695–2700, 2010.
- [84] Changhoon Lee, Jisook Hong, Myung-Hwan Whangbo, and Ji Hoon Shim. Enhancing the thermoelectric properties of layered transition-metal dichalcogenides 2H-MQ₂ (M= Mo, W; Q= S, Se, Te) by layer mixing: Density functional investigation. *Chemistry of Materials*, 25(18):3745–3752, 2013.
- [85] June Gunn Lee. *Computational materials science: an introduction*. CRC press, 2016.
- [86] Wen Lei, Shengli Zhang, Gunter Heymann, Xin Tang, Jianfeng Wen, Xiaojun Zheng, Guanghui Hu, and Xing Ming. A new 2D high-pressure phase of PdSe₂ with high-mobility transport anisotropy for photovoltaic applications. *Journal of Materials Chemistry C*, 7(7):2096–2105, 2019.
- [87] MH Lemée-Cailleau. *Structural study of the aluminophosphate AlPO 4-5 by neutron powder diffraction*. PhD thesis, PhD thesis, Université de Rennes I, 1989.
- [88] Chen W Li. *Phonon anharmonicity of ionic compounds and metals*. California Institute of Technology, 2012.
- [89] Haoxiang Li, Xiaoqing Zhou, Stephen Parham, Thomas Nummy, Justin Griffith, Kyle N Gordon, Eric L Chronister, Daniel S Dessau, et al. Spectroscopic evidence of low-energy gaps persisting up to 120 k in surface-doped p-terphenyl crystals. *Physical Review B*, 100(6):064511, 2019.
- [90] Zhipeng Li, Tianmeng Wang, Chenhao Jin, Zhengguang Lu, Zhen Lian, Yuze Meng, Mark Blei, Mengnan Gao, Takashi Taniguchi, Kenji Watanabe, et al. Momentum-dark intervalley exciton in monolayer tungsten diselenide brightened via chiral phonon. *ACS nano*, 13(12):14107–14113, 2019.
- [91] Jiao YY Lin, Gabriele Sala, and Matthew B Stone. A super-resolution technique to analyze single-crystal inelastic neutron scattering measurements using direct-geometry chopper spectrometers. *Review of Scientific Instruments*, 93(2):025101, 2022.
- [92] Daniel O Lindroth and Paul Erhart. Thermal transport in van der Waals solids from first-principles calculations. *Physical Review B*, 94(11):115205, 2016.
- [93] L Lindsay, DA Broido, and Natalio Mingo. Flexural phonons and thermal transport in graphene. *Physical Review B*, 82(11):115427, 2010.
- [94] L Lindsay, DA Broido, and Natalio Mingo. Flexural phonons and thermal transport in multilayer graphene and graphite. *Physical Review B*, 83(23):235428, 2011.
- [95] Gang Liu, Qimiao Zeng, Pengfei Zhu, Ruge Quhe, and Pengfei Lu. Negative poisson’s ratio in monolayer PdSe₂. *Computational Materials Science*, 160:309–314, 2019.
- [96] Brahim Lounis and William E Moerner. Single photons on demand from a single molecule at room temperature. *Nature*, 407(6803):491–493, 2000.

- [97] Peng Lv, Gang Tang, Yanyu Liu, Yingzhuo Lun, Xueyun Wang, and Jiawang Hong. Van der Waals direction transformation induced by shear strain in layered PdSe₂. *Extreme Mechanics Letters*, 44:101231, 2021.
- [98] J-Z Ma, J-B He, Y-F Xu, B-Q Lv, D Chen, W-L Zhu, S Zhang, L-Y Kong, X Gao, L-Y Rong, et al. Three-component fermions with surface fermi arcs in topological semimetal tungsten carbide. *arXiv preprint arXiv:1706.02664*, 2017.
- [99] Paul McEuen and C Kittel. Introduction to solid state physics. 2005.
- [100] N David Mermin and Herbert Wagner. Absence of ferromagnetism or antiferromagnetism in one-or two-dimensional isotropic heisenberg models. *Physical Review Letters*, 17(22):1133, 1966.
- [101] A Milosavljević, A Šolajić, S Djurdjić-Mijin, J Pešić, B Višić, Yu Liu, C Petrovic, N Lazarević, ZV Popović, et al. Lattice dynamics and phase transitions in Fe_{3-x}GeTe₂. *Physical Review B*, 99(21):214304, 2019.
- [102] Philip Charles Harry Mitchell. *Vibrational spectroscopy with neutrons: with applications in chemistry, biology, materials science and catalysis*, volume 3. World Scientific, 2005.
- [103] Arash Mobaraki, Cem Sevik, Haluk Yapicioglu, Deniz Çakır, and Oğuz Gülseren. Temperature-dependent phonon spectrum of transition metal dichalcogenides calculated from the spectral energy density: Lattice thermal conductivity as an application. *Physical Review B*, 100(3):035402, 2019.
- [104] M Mohr, J Maultzsch, E Dobardžić, S Reich, I Milošević, M Damnjanović, A Bosak, M Krisch, and C Thomsen. Phonon dispersion of graphite by inelastic X-ray scattering. *Physical Review B*, 76(3):035439, 2007.
- [105] Nicolas Mounet and Nicola Marzari. First-principles determination of the structural, vibrational and thermodynamic properties of diamond, graphite, and derivatives. *Physical Review B*, 71(20):205214, 2005.
- [106] R Murray and B Evans. The thermal expansion of 2H-MoS₂ and 2H-WSe₂ between 10 and 320 K. *Journal of Applied Crystallography*, 12(3):312–315, 1979.
- [107] Takeshi Nihira and Tadao Iwata. Temperature dependence of lattice vibrations and analysis of the specific heat of graphite. *Physical Review B*, 68(13):134305, 2003.
- [108] Y Nii, Y Hirokane, T Koretsune, D Ishikawa, AQR Baron, and Y Onose. Effect of symmetry breaking on short-wavelength acoustic phonons in the chiral magnet mnsi. *Physical Review B*, 104(8):L081101, 2021.
- [109] Payam Norouzzadeh and David J Singh. Cross-plane thermal conductivity of tungsten diselenide. *physica status solidi c*, 14(3-4):1700078, 2017.
- [110] Michel Orrit and J Bernard. Single pentacene molecules detected by fluorescence excitation in a p-terphenyl crystal. *Physical review letters*, 65(21):2716, 1990.

- [111] Mark Oxborrow, Jonathan D Breeze, and Neil M Alford. Room-temperature solid-state maser. *Nature*, 488(7411):353–356, 2012.
- [112] John P Perdew, Kieron Burke, and Matthias Ernzerhof. Generalized gradient approximation made simple. *Physical review letters*, 77(18):3865, 1996.
- [113] Nicola Pinto, Corrado Di Nicola, Angela Trapananti, Marco Minicucci, Andrea Di Cicco, Augusto Marcelli, Antonio Bianconi, Fabio Marchetti, Claudio Pettinari, and Andrea Perali. Potassium-doped para-terphenyl: Structure, electrical transport properties and possible signatures of a superconducting transition. *Condensed Matter*, 5(4):78, 2020.
- [114] Nadine Rademacher, Luke L Daemen, Eric L Chronister, and Th Proffen. Pair distribution function analysis of molecular compounds: significance and modeling approach discussed using the example of p-terphenyl. *Journal of Applied Crystallography*, 45(3):482–488, 2012.
- [115] Branimir Radisavljevic, Aleksandra Radenovic, Jacopo Brivio, Valentina Giacometti, and Andras Kis. Single-layer MoS₂ transistors. *Nature nanotechnology*, 6(3):147–150, 2011.
- [116] PA Reynolds and JW White. Inelastic neutron scattering spectrum of p-terphenyl. *Journal of the Chemical Society, Faraday Transactions 2: Molecular and Chemical Physics*, 68:1434–1438, 1972.
- [117] Andrew P Rice, Fook S Tham, and Eric L Chronister. A temperature dependent X-ray study of the order–disorder enantiotropic phase transition of p-terphenyl. *Journal of chemical crystallography*, 43(1):14–25, 2013.
- [118] HM Rietveld, EN Maslen, and CJB Clews. An X-ray and neutron diffraction refinement of the structure of p-terphenyl. *Acta Crystallographica Section B: Structural Crystallography and Crystal Chemistry*, 26(6):693–706, 1970.
- [119] Jason S Ross, Philip Klement, Aaron M Jones, Nirmal J Ghimire, Jiaqiang Yan, DG Mandrus, Takashi Taniguchi, Kenji Watanabe, Kenji Kitamura, Wang Yao, et al. Electrically tunable excitonic light-emitting diodes based on monolayer WSe₂ p–n junctions. *Nature nanotechnology*, 9(4):268–272, 2014.
- [120] Ayman H Said, Harald Sinn, and Ralu Divan. New developments in fabrication of high-energy-resolution analyzers for inelastic X-ray spectroscopy. *Journal of synchrotron radiation*, 18(3):492–496, 2011.
- [121] Ayman H Said, Harald Sinn, Thomas S Toellner, Ercan E Alp, Thomas Gog, Bogdan M Leu, Sunil Bean, and Ahmet Alatas. High-energy-resolution inelastic X-ray scattering spectrometer at beamline 30-ID of the advanced photon source. *Journal of synchrotron radiation*, 27(3):827–835, 2020.

- [122] Bohdan Schatschneider and Eric L Chronister. High-resolution ftir study of the para-terphenyl phase transition at high pressure. *Journal of luminescence*, 127(1):34–40, 2007.
- [123] Bohdan Schatschneider and Eric L Chronister. Molecular dynamics simulations of temperature-and pressure-induced solid–solid phase transitions in crystalline para-terphenyl. *Molecular Simulation*, 34(10-15):1159–1166, 2008.
- [124] Bohdan Schatschneider and Eric L Chronister. Molecular simulation of the pressure-induced crystallographic phase transition of p-terphenyl. *The Journal of Physical Chemistry B*, 115(3):407–413, 2011.
- [125] Bohdan Hindulak Schatschneider. *Structural and vibrational dynamics of molecular solids under variable temperature and pressure*. University of California, Riverside, 2008.
- [126] Ryosuke Senga, Kazu Suenaga, Paolo Barone, Shigeyuki Morishita, Francesco Mauri, and Thomas Pichler. Position and momentum mapping of vibrations in graphene nanostructures. *Nature*, 573(7773):247–250, 2019.
- [127] Guoyin Shen and Ho Kwang Mao. High-pressure studies with X-rays using diamond anvil cells. *Reports on Progress in Physics*, 80(1):016101, 2016.
- [128] Z-X Shen, A Lanzara, S Ishihara, and N Nagaosa. Role of the electron-phonon interaction in the strongly correlated cuprate superconductors. *Philosophical magazine B*, 82(13):1349–1368, 2002.
- [129] Sunil K Sinha. Theory of inelastic X-ray scattering from condensed matter. *Journal of Physics: Condensed Matter*, 13(34):7511, 2001.
- [130] Michael Sommer, Wolf-Dieter Schubert, Erich Zobetz, and Peter Warbichler. On the formation of very large WC crystals during sintering of ultrafine WC–Co alloys. *International Journal of Refractory Metals and Hard Materials*, 20(1):41–50, 2002.
- [131] C Souillard, X Rocquefelte, P-E Petit, M Evain, S Jobic, J-P Itié, P Munsch, H-J Koo, and M-H Whangbo. Experimental and theoretical investigation on the relative stability of the pds₂-and pyrite-type structures of PdSe₂. *Inorganic chemistry*, 43(6):1943–1949, 2004.
- [132] Andrea Splendiani, Liang Sun, Yuanbo Zhang, Tianshu Li, Jonghwan Kim, Chi-Yung Chim, Giulia Galli, and Feng Wang. Emerging photoluminescence in monolayer MoS₂. *Nano letters*, 10(4):1271–1275, 2010.
- [133] Motohiro Suzuki, Yuichi Inubushi, Makina Yabashi, and Tetsuya Ishikawa. Polarization control of an X-ray free-electron laser with a diamond phase retarder. *Journal of synchrotron radiation*, 21(3):466–472, 2014.

- [134] AD Taylor, EJ Wood, JA Goldstone, and J Eckert. Lineshape analysis and filter difference method for a high intensity time-of-flight inelastic neutron scattering spectrometer. *Nuclear Instruments and Methods in Physics Research*, 221(2):408–418, 1984.
- [135] TS Toellner, A Alatas, and AH Said. Six-reflection mev-monochromator for synchrotron radiation. *Journal of synchrotron radiation*, 18(4):605–611, 2011.
- [136] Atsushi Togo, Fumiyasu Oba, and Isao Tanaka. First-principles calculations of the ferroelastic transition between rutile-type and CaCl_2 -type SiO_2 at high pressures. *Physical Review B*, 78(13):134106, 2008.
- [137] Atsushi Togo and Isao Tanaka. First principles phonon calculations in materials science. *Scripta Materialia*, 108:1–5, 2015.
- [138] Hans Tornatzky, Roland Gillen, Hiroshi Uchiyama, and Janina Maultzsch. Phonon dispersion in mos_2 . *Physical Review B*, 99(14):144309, 2019.
- [139] B Toudic, P Launois, F Moussa, A Girard, and H Cailleau. Pressure dependence of conformational instabilities in crystalline p-terphenyl. *Ferroelectrics*, 80(1):241–244, 1988.
- [140] SN Vaidya and GC Kennedy. Compressibility of 18 molecular organic solids to 45 kbar. *The Journal of Chemical Physics*, 55(3):987–992, 1971.
- [141] Ganesan Venkataraman, Lee A Feldkamp, and Vinod C Sahni. *Dynamics of perfect crystals [by] G. Venkataraman, LA Feldkamp [and] VC Sahni*. 1975.
- [142] Guorui Wang, Zhaohu Dai, Junkai Xiao, ShiZhe Feng, Chuanxin Weng, Luqi Liu, Zhiping Xu, Rui Huang, and Zhong Zhang. Bending of multilayer van der Waals materials. *Physical Review Letters*, 123(11):116101, 2019.
- [143] Hengjia Wang and Murray S Daw. Anharmonic renormalization of the dispersion of flexural modes in graphene using atomistic calculations. *Physical Review B*, 94(15):155434, 2016.
- [144] Heshen Wang, Runzhang Xu, Cai Liu, Le Wang, Zhan Zhang, Huimin Su, Shanmin Wang, Yusheng Zhao, Zhaojun Liu, Dapeng Yu, et al. Pressure-dependent intermediate magnetic phase in thin Fe_3GeTe_2 flakes. *The Journal of Physical Chemistry Letters*, 11(17):7313–7319, 2020.
- [145] Qing Hua Wang, Kourosch Kalantar-Zadeh, Andras Kis, Jonathan N Coleman, and Michael S Strano. Electronics and optoelectronics of two-dimensional transition metal dichalcogenides. *Nature nanotechnology*, 7(11):699–712, 2012.
- [146] R Wang, Y Gao, Z Huang, and X Chen. Superconductivity at 43 K in a single CC bond linked terphenyl. arxiv 2017. *arXiv preprint arXiv:1703.05804*.
- [147] Ren-Shu Wang, Yun Gao, Zhong-Bing Huang, and Xiao-Jia Chen. Superconductivity above 120 kelvin in a chain link molecule. *arXiv preprint arXiv:1703.06641*, 2017.

- [148] Bin Wei, Junyan Liu, Qingan Cai, Ahmet Alatas, Meihua Hu, Chen Li, Jiawang Hong, et al. Giant anisotropic in-plane thermal conduction induced by anomalous phonons in pentagonal PdSe₂. *Materials Today Physics*, 22:100599, 2022.
- [149] Bin Wei, Qiyang Sun, Chen Li, and Jiawang Hong. Phonon anharmonicity: a pertinent review of recent progress and perspective. *Science China Physics, Mechanics & Astronomy*, 64(11):1–34, 2021.
- [150] M-H Whangbo and H-J Koo. Orbital interaction analysis of cooperative Jahn–Teller distortion, orbital ordering, spin ordering, and spin exchange interactions in magnetic solids. *Solid state sciences*, 4(3):335–346, 2002.
- [151] B Wyncke, F Brehat, and A Hadni. Variation du spectre infrarouge lointain du p-terphényle entre 300 k et 1, 3 k. *Journal de Physique*, 38(9):1171–1176, 1977.
- [152] Xiaoxiang Xi, Zefang Wang, Weiwei Zhao, Ju-Hyun Park, Kam Tuen Law, Helmuth Berger, László Forró, Jie Shan, and Kin Fai Mak. Ising pairing in superconducting NbSe₂ atomic layers. *Nature Physics*, 12(2):139–143, 2016.
- [153] Yu Xiao and Li-Dong Zhao. Seeking new, highly effective thermoelectrics. *Science*, 367(6483):1196–1197, 2020.
- [154] Jie-Min Xu, Shu-Yang Wang, Wen-Jun Wang, Yong-Hui Zhou, Xu-Liang Chen, Zhao-Rong Yang, and Zhe Qu. Possible tricritical behavior and anomalous lattice softening in van der Waals itinerant ferromagnet Fe₃GeTe₂ under high pressure. *Chinese Physics Letters*, 37(7):076202, 2020.
- [155] Yucong Yang, Tao Liu, Lei Bi, and Longjiang Deng. Recent advances in development of magnetic garnet thin films for applications in spintronics and photonics. *Journal of Alloys and Compounds*, 860:158235, 2021.
- [156] Jieyu Yi, Houlong Zhuang, Qiang Zou, Zhiming Wu, Guixin Cao, Siwei Tang, SA Calder, PRC Kent, David Mandrus, and Zheng Gai. Competing antiferromagnetism in a quasi-2D itinerant ferromagnet: Fe₃GeTe₂. *2D Materials*, 4(1):011005, 2016.
- [157] Tingting Yin, Kanchan Ajit Ulman, Sheng Liu, Andrés Granados del Águila, Yuqing Huang, Lifa Zhang, Marco Serra, David Sedmidubsky, Zdenek Sofer, Su Ying Quek, et al. Chiral phonons and giant magneto-optical effect in CrBr₃ 2D magnet. *Advanced Materials*, 33(36):2101618, 2021.
- [158] Yijun Yu, Liguang Ma, Peng Cai, Ruidan Zhong, Cun Ye, Jian Shen, Genda D Gu, Xian Hui Chen, and Yuanbo Zhang. High-temperature superconductivity in monolayer Bi₂Sr₂CaCu₂O_{8+δ}. *Nature*, 575(7781):156–163, 2019.
- [159] Kunpeng Yuan, Xiaoliang Zhang, Lin Li, and Dawei Tang. Effects of tensile strain and finite size on thermal conductivity in monolayer WSe₂. *Physical Chemistry Chemical Physics*, 21(1):468–477, 2019.

- [160] Gao Yun, Wang Ren-Shu, Wu Xiao-Lin, Cheng Jia, Deng Tian-Guo, Yan Xun-Wang, and Huang Zhong-Bing. Searching superconductivity in potassium-doped p-terphenyl. *Wuli*, 65:077402, 2016.
- [161] H Zabel, WA Kamitakahara, and RM Nicklow. Neutron scattering investigation of layer-bending modes in alkali-metal—graphite intercalation compounds. *Physical Review B*, 26(10):5919, 1982.
- [162] Igor A Zaliznyak, Andrei T Savici, V Ovidiu Garlea, Barry Winn, Uwe Filges, John Schneeloch, John M Tranquada, Genda Gu, Aifeng Wang, and Cedomir Petrovic. Polarized neutron scattering on hyspec: the hybrid spectrometer at SNS. In *Journal of Physics: Conference Series*, volume 862, page 012030. IOP Publishing, 2017.
- [163] Hualing Zeng, Junfeng Dai, Wang Yao, Di Xiao, and Xiaodong Cui. Valley polarization in MoS₂ monolayers by optical pumping. *Nature nanotechnology*, 7(8):490–493, 2012.
- [164] Kai Zhang, Ren-Shu Wang, and Xiao-Jia Chen. Vibrational properties of p-terphenyl. *The Journal of Physical Chemistry A*, 122(34):6903–6908, 2018.
- [165] Lifa Zhang and Qian Niu. Angular momentum of phonons and the Einstein–de Haas effect. *Physical Review Letters*, 112(8):085503, 2014.
- [166] Lifa Zhang and Qian Niu. Chiral phonons at high-symmetry points in monolayer hexagonal lattices. *Physical review letters*, 115(11):115502, 2015.
- [167] Yun Zhang, Haiyan Lu, Xiegang Zhu, Shiyong Tan, Wei Feng, Qin Liu, Wen Zhang, Qiuyun Chen, Yi Liu, Xuebing Luo, et al. Emergence of Kondo lattice behavior in a van der Waals itinerant ferromagnet, Fe₃GeTe₂. *Science advances*, 4(1):eaao6791, 2018.
- [168] Hanyu Zhu, Jun Yi, Ming-Yang Li, Jun Xiao, Lifa Zhang, Chih-Wen Yang, Robert A Kaindl, Lain-Jong Li, Yuan Wang, and Xiang Zhang. Observation of chiral phonons. *Science*, 359(6375):579–582, 2018.
- [169] Zhiyong Y Zhu, Yingchun C Cheng, and Udo Schwingenschlögl. Giant spin-orbit-induced spin splitting in two-dimensional transition-metal dichalcogenide semiconductors. *Physical Review B*, 84(15):153402, 2011.
- [170] Houlong L Zhuang, PRC Kent, and Richard G Hennig. Strong anisotropy and magnetostriction in the two-dimensional stoner ferromagnet Fe₃GeTe₂. *Physical Review B*, 93(13):134407, 2016.
- [171] John M Ziman. *Electrons and phonons: the theory of transport phenomena in solids*. Oxford university press, 2001.